# Influence of High Mobility Polymer Semiconductors in Organic Photovoltaics

by

Leanne Murphy

A thesis

presented to the University of Waterloo

in fulfillment of the

thesis requirement for the degree of

Master of Applied Science

in

Chemical Engineering - Nanotechnology

Waterloo, Ontario, Canada, 2013

# AUTHOR'S DECLARATION

I hereby declare that I am the sole author of this thesis. This is a true copy of the thesis, including any required final revisions, as accepted by my examiners. I understand that my thesis may be made electronically available to the public.

# Abstract

Increasing global energy demands and diminishing supplies of conventional fuels are forcing the world to focus more on alternative power sources that are both renewable and ecologically benign. Solar energy is clean, regularly available and can be harvested without sacrificing valuable land space. Due to the associated cost of solar cells, however a very small portion of the world's energy needs are supplied by the sun. Solution-processable organic photovoltaics (OPVs) offer the promise of lower production costs relative to conventional (silicon) solar cell technology. Solution-processing can be performed using reel-to-reel manufacturing, with printing and coating techniques that are significantly cheaper than current processing methods for inorganic semiconductors. Although OPV efficiency values currently remain inferior to those of conventional solar cells, the rate of improvement is much higher in OPVs than in other solar cell technologies. Recently an efficiency exceeding 10% was reported for organic solar cells.

An important difference between organic and conventional solar cells is the charge carrier mobility of the semiconductors, which tends to be relatively low in organic semiconductors. Recent advances in molecular design have led to polymer semiconductor materials that possess hole mobility values similar to that of amorphous silicon. The present study investigates potential improvements in OPV devices that can be achieved through the application of high hole mobility polymer semiconductor donors.

Two diketopyrrolopyrrole-based polymers, PDQT and PDBFBT, were selected for the role of electron donor in OPV devices due to their high mobilities and their optimum optical and electrical properties. Optimization of the process parameters was performed using $PC_{61}BM$ as the acceptor. A relatively high quantity of $PC_{61}BM$ (3 - 4 × the weight of the donor) is required in the donor-acceptor blends of both polymers in order to balance the high hole mobility. For these donor-acceptor blends, a solvent system consisting of chloroform/ortho-dichlorobenzene (4:1 v/v) is necessary for proper solubility, and an additive, 1,8-diiodooctane, is required to achieve an acceptable morphology.

The main benefit expected from the use of high mobility semiconductors is reduced charge recombination. This was studied in relation to the active layer thickness in standard and inverted OPV devices prepared using $PC_{61}BM$ as the acceptor. Normally the thickness of the active layer is required to be low (~100 nm) due to the poor charge transport mobility of the carriers. In this study, rather consistent power conversion efficiencies were achieved throughout a wide range of active layer

thicknesses (~100 nm to ~800 nm). A comparison between standard and inverted device configurations demonstrates that the inverted configuration is more suitable for achieving thicker active layers when a high hole mobility donor is used. This is attributed to the longer hole collection path in the inverted structure, which can benefit from using a high hole mobility material.

Increasing the absorption spectra of the donor-acceptor blend was studied by substituting $PC_{71}BM$ for $PC_{61}BM$. The improved absorption leads to greater charge generation. In PDQT devices, the increase in absorption that is contributed by $PC_{71}BM$ appears to be of greatest benefit when active layers are not very thick. Therefore, when thick active layers (>500 nm) are required, the use of $PC_{61}BM$ is sufficient, in conjunction with a high mobility donor.

Finally, an increase in a polymer's crystallinity can often lead to greater mobility. This can be accomplished through various annealing techniques. The improved crystallinity of PDBFBT that occurs as a result of thermal annealing was studied in OPV applications. Although hole mobility of PDBFBT in the lateral direction improves with thermal annealing, mobility in the vertical direction decreases with increasing temperature. This suggests that the crystallinity of PDBFBT is oriented in the lateral direction as opposed to the vertical direction, thereby directing charge flow horizontal to the surface. With thermal annealing, an optimal amount of $PC_{61}BM$ added to PDBFBT can increase the vertical mobility to fairly high values. Nevertheless, the efficiency of standard and inverted OPV devices decreases with increased annealing temperature. This is attributed to agglomeration of $PC_{61}BM$ that occurs from an increase in annealing temperature. The results of this study demonstrate that thermal annealing is not beneficial for PDBFBT:$PC_{61}BM$ films in OPV applications due to the vertical orientation of devices.

All of the studies presented in this work involve the use of high hole mobility polymer semiconductors as donor materials for OPV applications. This work will provide a deeper understanding of the properties required for the development of new semiconductor materials in OPV applications. Furthermore, this work will be very useful for the design of device structures for more feasible manufacturing of large area OPV devices via high speed roll-to-roll printing processes.

# Acknowledgements

I would like to thank my supervisors, Dr. Yuning Li and Dr. Hany Aziz, who gave me the opportunity to work within their groups and benefit from their knowledge and experience.

Special thanks go to Dr. Wei Hong for his expert synthesis of all of the DPP polymers that were tested in this thesis.

I would also like to thank several of my colleagues including Graeme Williams, Uyxing Vongsaysy, Bin Sun and Jonathan Yuen for their technical guidance and training. I would like to thank the members of both the Li and Aziz research groups for their valuable insights and motivation.

Thanks go to my review committee, Dr. Zhongwei Chen and Dr. Boxin Zhao.

Finally, I would like to thank my husband for his patience and constant support throughout this entire process.

The work reported herein was financially supported by the Natural Sciences and Engineering Research Council of Canada and the University of Waterloo.

# Table of Contents

# List of Figures

# List of Tables

# List of Abbreviations, Symbols and Nomenclature

| | |
|---|---|
| A: | Absorbance |
| AFM: | Atomic force microscopy |
| Ag: | Silver |
| Al: | Aluminum |
| BHJ: | Bulk heterojunction |
| $Bu_4NPF_6$ | Tetrabutylammonium hexafluorophosphate |
| CV: | Cyclic voltammetry |
| D/A: | Donor-Acceptor ratio |
| d-a: | Donor-acceptor |
| DPP: | Diketopyrrolopyrrole |
| $e^-$: | Electron |
| $E_g$: | Band gap |
| $E_{HOMO}$: | HOMO energy level |
| $E_{LUMO}$: | LUMO energy level |
| EQE: | External quantum efficiency |
| FET: | Field-effect transistor |
| *FF*: | Fill factor (%) |
| $h^+$: | Hole |
| HOMO: | Highest occupied molecular orbital |
| HTL: | Hole transport layer |
| IQE: | Internal quantum efficiency |
| ITO: | Indium tin oxide |
| *J*: | Current density ($mAcm^{-2}$) |
| $J_{ill}$: | Illuminated current density ($mAcm^{-2}$) |
| $J_D$: | Dark current density ($mAcm^{-2}$) |
| $J_{SC}$: | Short circuit current density ($mAcm^{-2}$) |

| | |
|---|---|
| L: | Thickness (nm) |
| $L_{ex}$: | Exciton diffusion length |
| LiF: | Lithium fluoride |
| LUMO: | Lowest unoccupied molecular orbital |
| $M_n$ | Molecular weight |
| MEH-PPV: | Poly[2-methoxy, 5-(2'-ethyl-hexyloxy)-*p*-phenylenevinylene)] |
| $MoO_3$: | Molybdenum oxide |
| NiO: | Nickel oxide |
| OPV: | Organic photovoltaic |
| OTFT: | Organic thin film transistor |
| P3HT: | Poly(3-hexylthiophene) |
| PBTTT: | Poly[2,5-bis(3-alkylthiophen-2-yl)thieno[3,2-b]thiophene)] |
| $PC_{61}BM$: | Phenyl-C61-butyric acid methyl ester |
| $PC_{71}BM$: | Phenyl-C71-butyric acid methyl ester |
| PCE: | Power conversion efficiency (%) |
| PCPDTBT: | Poly[2,6-(4,4-bis-(2-ethyhexyl)-4H-cyclopenta[2,1-b;3,4-b']-dithiophene)-*alt*-4,7-(2,1,3-benzothiadiazole)] |
| PDDTT: | Poly[5,7-bis(4-decanyl-2-thienyl)thieno[3,4-b] diathiazole-thiophene-2,5)] |
| PDI | Polydispersity index |
| PDOCPDT: | Poly[2,5-(7,7-dioctyl)-cyclopentadithiophene] |
| PEDOT:PSS: | Poly(3,4-ethylenedioxythiophene) poly(styrenesulfonate) |
| $P_{inc}$: | Incident optical power (~1 $mW/mm^2$) |
| $P_{max}$: | Maximum power output ($mW/mm^2$) |
| PTAA: | Poly(triarylamine) |
| PTV: | Poly(thienylene vinylene) |
| $R_{series}$: | Series resistance ($\Omega \cdot cm^2$) |
| $R_{shunt}$: | Shunt resistance ($\Omega \cdot cm^2$) |
| T: | Transmittance |

| | |
|---|---|
| $TiO_x$: | Titanium oxide |
| $TiO_2$: | Titanium dioxide |
| UV-Vis: | Ultraviolet-Visible spectrometry |
| $V$: | Applied voltage (V) |
| $V_{eff}$ : | Effective voltage (V) |
| $V_{bi}$: | Built-in voltage (V) |
| $V_{OC}$: | Open circuit voltage (V) |
| XRD: | X-ray diffraction |
| ZnO: | Zinc oxide |
| $\beta$: | Field activation factor |
| $\Delta E_{LUMO}$: | LUMO-LUMO offset between donor and acceptor ($e$V) |
| $\varepsilon_0$ | Permittivity of free space ($8.85 \times 10^{-12}$ F/m) |
| $\varepsilon_r$ | Relative permittivity |
| $\lambda_{onset}$: | Onset of absorption (nm) |
| $\mu$: | Mobility ($cm^2V^{-1}s^{-1}$) |
| $\mu_e$: | Electron mobility ($cm^2V^{-1}s^{-1}$) |
| $\mu_h$: | Hole mobility ($cm^2V^{-1}s^{-1}$) |

# Chapter 1.

# Introduction

## 1.1 Overview

Increasing global energy demands and diminishing supplies of conventional fuels (fossil fuels, uranium) have gradually forced the world to focus more on power sources that are both renewable and ecologically benign (i.e. solar, hydrogen, wind, biomass, etc.). Of these alternative resources, solar power offers a wide array of benefits that other approaches do not. Solar energy is clean, regularly available and can be harvested without sacrificing valuable land space. Unlike the equipment of other alternative technologies, solar cells do not possess moving components that require regular maintenance. Despite the abundance of the sun's radiation, a very small portion of the world's energy needs are supplied through solar cells due mainly to the associated cost.

Solar cells convert sunlight into electricity through the use of semiconductor technology in what is known as the photovoltaic effect. In 1954, the first modern photovoltaic cell was developed at Bell Laboratories using silicon as the semiconductor. The efficiency of this silicon-based photocell was 6% [1]. Shortly thereafter, in 1958, the use of organic semiconductors was demonstrated in the first two layer organic photovoltaic (OPV) system [2]. Progress in silicon-based solar cells progressed rather rapidly, whereas marginal progress was made throughout the decades in the field of OPVs [3]. It wasn't until 1995 that the first solution-processed bulk heterojunction (BHJ) solar cell was reported [4]. The device's efficiency of 2.9% was a significant improvement for OPVs, but a sizeable disparity from that of the first silicon solar cell created almost four decades earlier.

Historically the major obstacle to widespread acceptance of conventional solar technology has been the cost. Electricity produced by silicon-based solar cells is more expensive than grid-supplied electricity. The main reason for the high cost of solar electricity is the expensive semiconductor processing technologies that are required [5]. OPVs, on the other hand, offer the promise of relatively lower production costs and a faster return on investment than conventional solar cell technology [5–8]. The potential for lower costs is a result of the ability to solution-process OPV semiconductors. Processing can be performed using reel-to-reel manufacturing, with printing and coating techniques that are significantly cheaper than current methods of solar cell fabrication [5].

Currently the solar cell market is dominated by silicon based technology (>85%) [7] however interest in OPV technology is increasing. Today, reported efficiency values continue to escalate, with a high PCE of 12% most recently announced by Heliatek [9]. The rate of improvements in efficiency of OPVs tends to be much higher than that of other solar cell technologies [7].

OPV technology has great potential but must fulfil the basic requirements in not just cost, but lifetime and efficiency as well [5]. Current OPV efficiency is still inferior to that of silicon solar cells, which is generally around 25%. Combined with their low strength and stability, this makes them inadequate for economically viable products and therefore uncompetitive with conventional solar cells. An important difference between organic and conventional solar cells is the charge carrier mobilities of the semiconductors. Polymer mobilities have typically been several orders of magnitude lower than that of inorganic semiconductors such as silicon and gallium arsenide (see Figure 1) [10–12]. Advances in materials design for organic transistors have recently led to polymers with mobilities exceeding that of amorphous silicon [13–16]. Although high charge carrier mobility is regarded as an important attribute in OPV semiconductors, the study of such materials in this field is rather limited. With such a high potential in cost savings, clearly there is value for further research into the application of high mobility materials in organic photovoltaics.

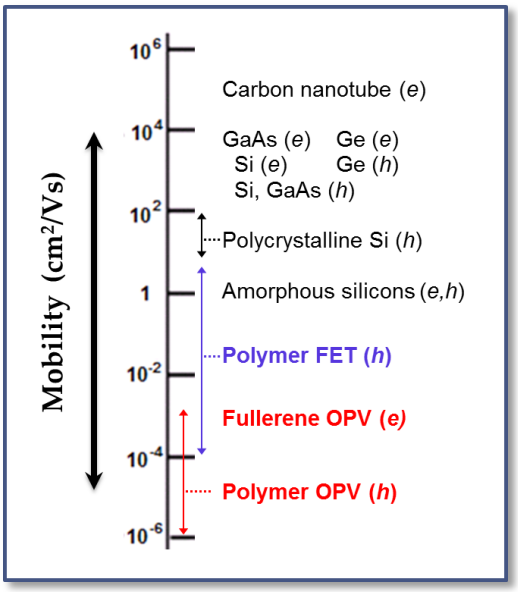


**Figure 1.** Comparison of charge carrier mobility values of common semiconductor materials. Hole and electron mobilities are differentiated by the bracketed notation (*e*) or (*h*), respectively, adapted from [17].

## 1.2 Organic Photovoltaics (OPVs)

### 1.2.1 Structure

The basic structure of the modern OPV device consists of two electrodes - the anode and the cathode, a hole transport layer (HTL), an active layer and an electron transport layer (ETL) (Figure 2).

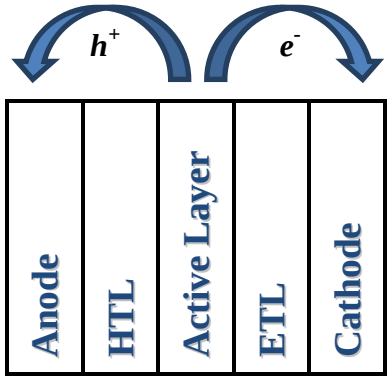


**Figure 2.** The basic layer structure of OPV devices consists of an anode, a hole transport layer (HTL), an active layer, an electron transport layer (ETL) and a cathode.

The ***active layer*** is the heart of the solar cell; the layer in which the energy of a photon is harvested. The active layer is composed of at least two different semiconductor materials, an electron donor and an electron acceptor. These semiconductors perform several functions: they absorb photons from light, convert the photons into charge (holes ($h^+$) and electrons ($e^-$)), and then transport the charges to their respective electrodes.

The ***anode*** is the electrode that collects holes, whereas the ***cathode*** is the electrode that collects electrons. Both electrodes are typically conductive metals. The work function of the cathode must be lower than that of the anode in order to create a built-in potential that drives the electrons and holes toward their respective electrodes [18]. One of the electrodes must be a transparent conductor, such as indium-tin-oxide (ITO), which allows light to penetrate into the active layer. Since ITO must be deposited using extremely high temperatures that damage organics, the ITO layer is generally the first or bottom layer of the device.

The ***hole transport layer*** (HTL) is a high work function material located next to the anode. The role of the HTL is to enhance hole collection at the anode while acting as an electron-blocking layer. One of the most commonly used HTLs is the solution-processed conducting polymer, poly(3,4-

ethylenedioxythiophene):poly(styrene sulfanate) (PEDOT:PSS). Other HTLs of interest include oxides such as molybdenum oxide ($MoO_3$) [19,20] and nickel oxide (NiO) [21,22]. The ***electron transport layer*** (ETL), on the other hand is a low work function material included between the active layer and the cathode to improve electron injection and block holes. Commonly used ETLs are metal oxides, such as zinc oxide (ZnO) and titanium oxide (TiOx) [18,23,24], or lithium fluoride (LiF), which is reported to change the effective work function of aluminum (Al) by shifting the vacuum level at the LiF/Al interface [25].

The most common geometry for OPV devices is referred to in the literature as the "standard", "normal" or "conventional" configuration. Recently, however the inverted OPV architecture has gained popularity due to its higher stability in air [26–28]. The main difference between the two configurations is the electrode positioning with respect to the light source: in the standard configuration, the transparent ITO electrode acts as the hole-collecting anode, whereas in the inverted configuration ITO acts as the electron-collecting cathode (Figure 3). ITO can be transformed into either anode or cathode through the use of a buffer layer with an appropriate work function.

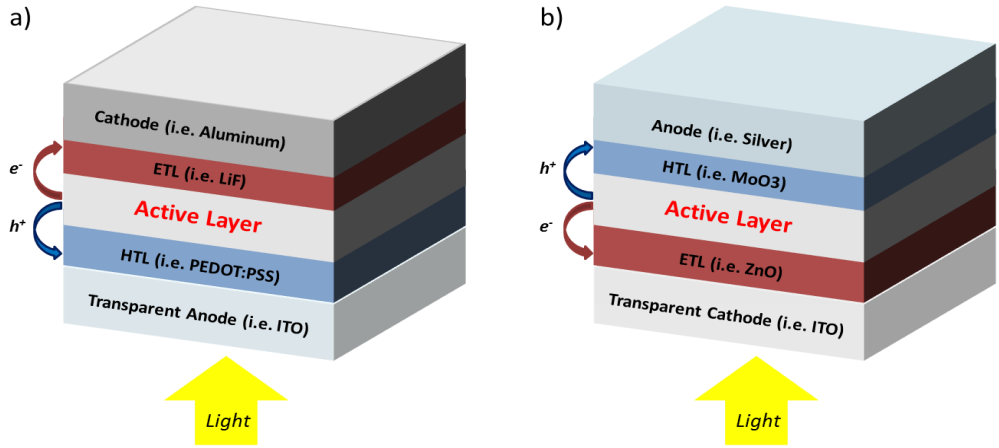


**Figure 3**. (a) Standard geometry, and (b) inverted geometry of a bulk-heterojunction solar cell. The different geometries cause electrons and holes to exit the device in the opposite direction.

The generation of current requires that the energy levels of each layer are aligned with those of the neighbouring layers. The energy levels of organic semiconductors are referred to as the highest occupied molecular orbital (HOMO) and the lowest unoccupied molecular orbital (LUMO). The band gap ($E_g$) is the minimum energy of a photon required to excite an electron from the HOMO to the LUMO (Figure 4). When photons of energy greater than $E_g$ are absorbed by the electron donor,

the excited electron ($e^-$) jumps from the HOMO to the LUMO and an associated hole ($h^+$) is created. The electron-hole pair (exciton), which typically remains bound due to Coulombic attraction, diffuses to the donor-acceptor (d-a) interface where charge separation occurs. The electron jumps from the donor LUMO to the acceptor LUMO, which is lower in energy and therefore more favourable for the electron. The dissociated charges are then transported to their respective electrodes resulting in current [8,29].

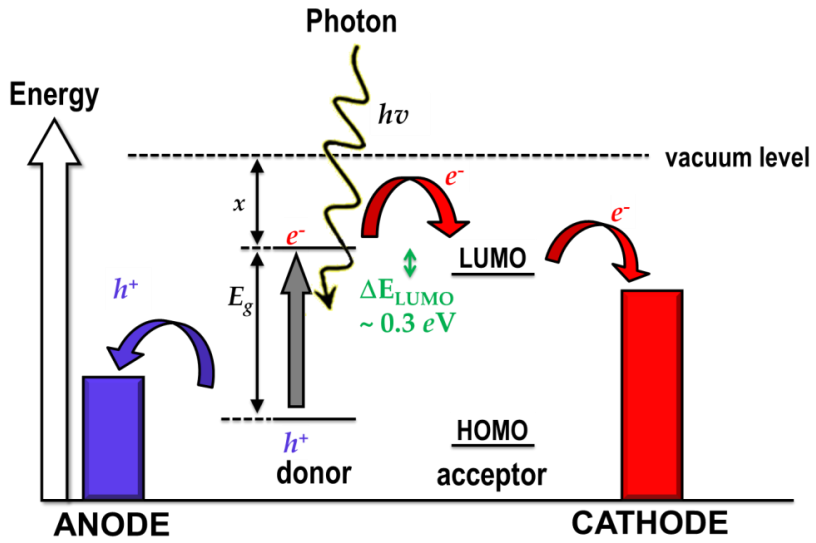


**Figure 4.** Harvesting of energy from a photon at the donor-acceptor interface within the active layer of a photovoltaic cell, adapted from [29].

Charge losses can occur in several ways. First, the distance that an exciton is capable of migrating from the site of generation to the d-a interface is based on the charge mobility (μ) of the semiconductor. This distance is referred to as the exciton diffusion length ($L_{ex}$) [29,30]. If the required diffusion distance is greater than $L_{ex}$, the exciton will not reach the d-a interface and will return to the unexcited state. Should the exciton reach the d-a interface, there are two key loss mechanisms by which charge recombination can occur in OPVs: geminate and bimolecular recombination (Figure 5). Geminate, or mono-molecular recombination refers to the recombination of charge ($h^+$ and $e^-$) generated from the *same* exciton. Bimolecular recombination, on the other hand, refers to the recombination of dissociated charge generated from *different* excitons that may have been a distance apart [31,32].

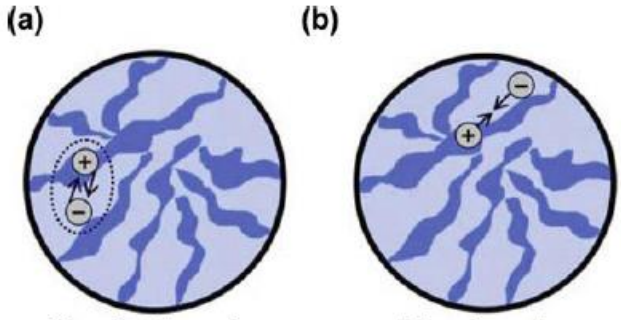


**Figure 5.** The two key mechanisms of hole-electron recombination in OPVs (a) geminate pair recombination and (b) bimolecular recombination, taken from [31].

Recombination of electrons and holes is very undesirable and can be affected by the type of junction between the donor and acceptor. There are three types of junctions used to form donor-acceptor interfaces [33,34] (Figure 6).

A ***bilayer heterojunction*** (or planar heterojunction) is simply a layer of acceptor material adjacent to a layer of donor material (Figure 6a). The efficiency of this type of device is dependent on the thickness of each layer, which must be less than $L_{ex}$. Very thin films are therefore preferable to avoid recombination.

An ***ordered heterojunction*** offers a direct charge transport pathway through vertically aligned columns (Figure 6b). The columns are typically grown from inorganic semiconductors. They are ideal but more complicated and thus more expensive to create.

A **b*ulk heterojunction*** (BHJ) is an interpenetrating network of acceptor and donor (Figure 6c). It is the most common type of heterojunction for polymer-based OPVs since it increases the contact area between the donor and acceptor (compared to bilayer) and can be achieved more cost-effectively through solution-processing (compared to bilayer and ordered) [34]. BHJs are formed by spin-casting the donor and acceptor from a common solvent [33]. Phase separation between the donor and acceptor materials in the solid state has a direct impact on PCE. To achieve high efficiency, the nanodomain size must correspond to $L_{ex}$ in each material. In organic materials, $L_{ex}$ is typically only 5–10 nm [7]. Methods to optimize the organization of the two nanophases include thermal annealing, choice of solvent and solvent additives [35].

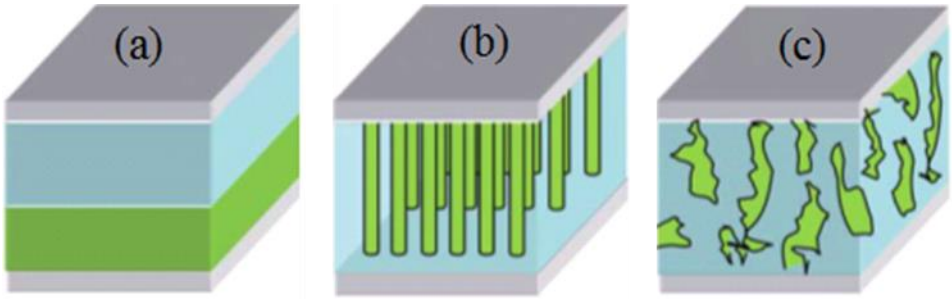


**Figure 6.** Donor-acceptor configurations within the active layer (a) bilayer heterojunctions; (b) ordered heterojunctions and (c) bulk heterojunctions, taken from [34].

### 1.2.2 Efficiency

The efficiency of an OPV device is the gauge by which success is measured. There are three main methods by which efficiency is measured: internal quantum efficiency (IQE), external quantum efficiency (EQE) and power conversion efficiency (PCE) [36]. Most research refers to the power conversion efficiency when communicating the effectiveness of a device [5,8,29].

PCE of a solar cell is the ratio of the maximum power output of the solar cell ($P_{max}$) to the incident power density ($P_{inc}$), which is the solar power available on the Earth's surface (~1 mW/mm$^2$).

$$\mathrm{PCE} = \frac{P_{max}}{P_{inc}} \quad \textbf{(1)}$$

$P_{max}$ is the product of three variables: short circuit current density ($J_{SC}$), open circuit voltage ($V_{OC}$), and fill factor (*FF*) [36].

$$P_{max} = \mathrm{J}_{SC} \times \mathrm{V}_{OC} \times \mathrm{FF} = J_{max} \times V_{max} \quad \textbf{(2)}$$

- ***Short-circuit Current*** ($J_{SC}$) is the current across the solar cell at zero voltage and is a result of generation and collection of charge carriers. It is influenced by several factors, including the number of photons available and the optical properties of the solar cell. Increases in short circuit current density can be obtained by improved harnessing of photons in the red and infrared regions and by increasing the optical density [7].
- ***Open-circuit Voltage*** ($V_{OC}$) is the maximum voltage that a solar cell has available. It is the difference between the highest occupied molecular orbital (HOMO) of the donor and the lowest unoccupied molecular orbital (LUMO) of the acceptor [37]. The theoretical value of

$V_{OC}$ can be calculated using Equation (3) [37]. Improvements in open circuit voltage can be obtained by minimizing the band offset between the donor and the acceptor [7].

$$V_{OC} = \frac{1}{e}(|E^{Donor}HOMO| - |E^{Acceptor}LUMO|) - 0.3\,V \quad \textbf{(3)}$$

- ***Fill Factor*** (*FF*) is the ratio of the maximum power ($P_{max}$) to the product of $J_{SC}$ and $V_{OC}$. It is mainly influenced by charge recombination and ohmic losses, which must be low in order to have high *FF* [7].

$P_{max}$, $J_{SC}$ and $V_{OC}$ are determined directly from a current-voltage (*J-V*) curve (Figure 7). *FF* is then calculated from Equation 2 and PCE is calculated using Equation 1.

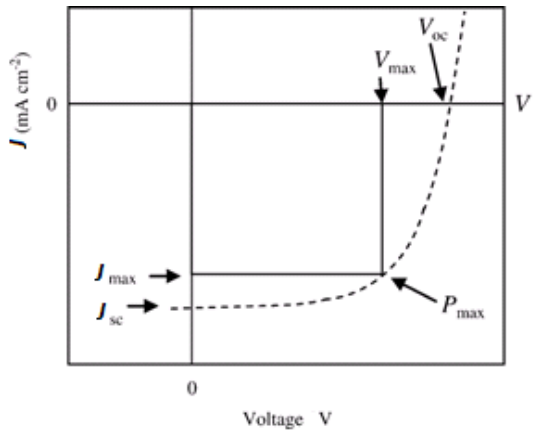


**Figure 7.** Current-voltage (*J-V*) curve for an illuminated photovoltaic device demonstrating how parameters are extracted from the curve, taken from [29].

Each variable is influenced to some degree by ***shunt resistance*** ($R_{shunt}$) and ***series resistance*** ($R_{series}$). $R_{shunt}$ is indicative of the charge losses due to recombination and trapping [38] and must be sufficiently high in order to prevent leakage currents [11]. $R_{series}$, on the other hand, is a result of ohmic losses arising from obstructed charge flow. The presence of charge traps in the bulk, energy barriers at the interfaces, and the formation of space charges due to poor charge collection versus generation rates may lead to a large $R_{series}$ [38]. Low series resistance is therefore required to improve the forward current [11]. Resistance generally has the greatest effect on *FF* but $J_{SC}$ is also influenced by very large series resistance values (10-100 $\Omega \cdot cm^2$) [39].

## 1.3 The Electron Acceptor

The electron acceptor is an n-type semiconductor material with high electron affinity. Fullerene derivatives such as phenyl-C61-butyric acid methyl ester ($PC_{61}BM$) and phenyl-C71-butyric acid methyl ester ($PC_{71}BM$) (Figure 8a and 8b) have been studied in photovoltaic devices since the early 1990s [40]. They are the most commonly used organic acceptors in solution-processed OPVs due to their ability to dissolve in the same solvents in which the electron donor is dissolved, making the active layer completely solution-processable. Electron flow from the acceptor to the cathode is determined by the dispersion of the acceptor in solvent [41]. Therefore, solvents such as chlorobenzene and dichlorobenzene are commonly used due to their excellent ability to dissolve PCBM, in addition to their film forming properties. Because of its popularity, rapid advancements have been made using PCBM as the electron acceptor, leading to marked increases in efficiencies in a short time [42].

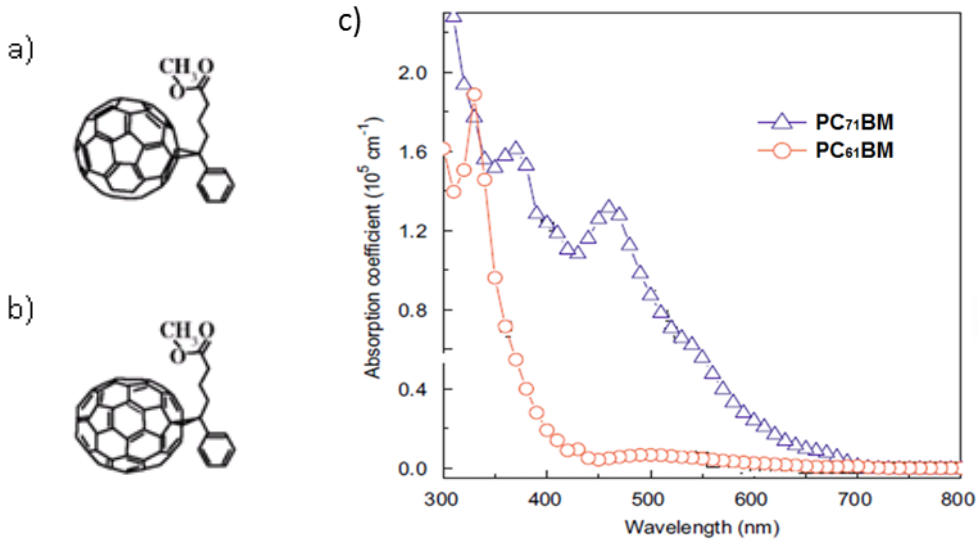


**Figure 8.** Common organic materials used as electron acceptors a) $PC_{61}BM$: phenyl-C61-butyric acid methyl ester and b) $PC_{71}BM$: phenyl-C71-butyric acid methyl ester, c) UV-Vis absorption of $PC_{61}BM$ and $PC_{71}BM$, taken from [43].

$PC_{61}BM$ and $PC_{71}BM$ differ in their absorption spectra in that $PC_{71}BM$ has greater absorption than $PC_{61}BM$ in the 400 to 600 nm range (Figure 8c). $PC_{71}BM$ is therefore often used in conjunction with low band gap donors that predominately absorb at higher wavelengths (>600 nm), thus allowing greater absorption of light throughout the visible spectrum, leading to higher efficiencies.

There are several limitations to the use of fullerene derivatives as the electron acceptor in OPVs, which include high material cost, deep LUMO level [44] and nanophase separation issues [45,46]. The electron mobility ($\mu_e$) of PCBM (~$2.4 \times 10^{-3}$ $cm^2V^{-1}s^{-1}$ [47]) tends to be high amongst other electron acceptor materials for OPVs but is considerably lower than that of inorganics (Figure 1). As a result, the photoactive layer in OPVs is required to be very thin (~50-100 nm) [41,48] and thus is incapable of efficiently absorbing sunlight for photocurrent generation.

## 1.4 The Electron Donor

Organic electron donors are generally divided into two categories: (1) small molecular weight and (2) polymeric semiconductors. Solutions prepared with small molecular weight semiconductors often possess insufficient viscosity for film casting. In addition, small molecules have a tendency to self-assemble, which leads to unfavourable nanoscale morphology in the BHJ structure [49,50]. As a result, many small molecules are not solution-processable and must therefore be deposited using thermal evaporation. For these reasons polymer semiconductors are of greater interest for the current study.

In polymer-based OPVs, the electron donor is a p-type polymer semiconductor. In addition to transporting holes to the anode, the donor polymer also acts as the dominant light harvesting material. Figure 9 displays the structure of some of the common semiconducting donor polymers found in the literature. Poly(3-hexylthiophene) (P3HT) is one of the most studied polymer semiconductors in the literature today and is therefore often used as a standard for comparison. New donor materials are constantly being developed and many have led to considerably better performance. Qualities such as low band gap, optimal energy levels and high hole mobility ($\mu_h$) are considered necessary in the design of new donor materials.

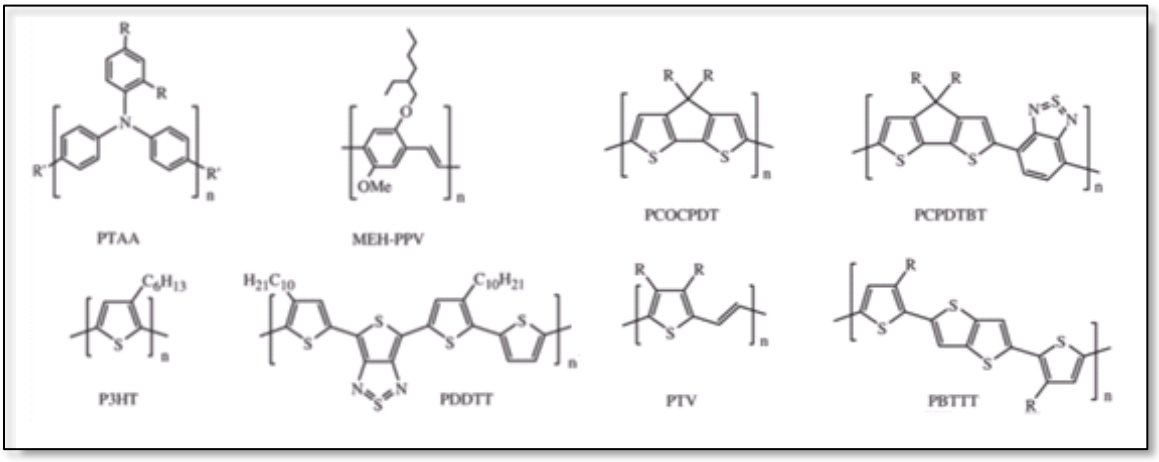


**Figure 9.** Common polymers used as electron donors in OPVs, taken from [29]. (See List of Abbreviations, Symbols and Nomenclature for full names.)

A low band gap is associated with stronger and broader absorption of photons [51]. In general, a band gap is considered to be low if it is below 2 *e*V (the ability to absorb photons with wavelengths longer than 620 nm) [51]. Some strategies used to decrease the band gap include increasing conjugation, increasing the degree of co-planarity or the use of quinoid structures [29,52].

Another common strategy to achieve a low band gap is to incorporate electron deficient and electron rich units in the polymer backbone [13,52–62]. Such alternating copolymers are referred to as donor-acceptor (d-a) molecules and are currently of great interest as donor materials for high efficiency OPVs [52,58–72]. In addition to their optimal band gaps (1.2-1.7 eV), d-a molecules tend to possess favourable HOMO/LUMO levels that match well with the LUMO of common acceptor materials such as fullerene derivatives [72].

In order to achieve optimal energy levels, the position of the donor LUMO level must be sufficiently higher than the position of the acceptor LUMO level (refer to Figure 4) in order to provide enough energy offset for exciton dissociation. The LUMO-LUMO offset ($\Delta E_{LUMO}$) must, however be small enough to minimize energy loss during electron transfer [34] (generally $\Delta E_{LUMO}$ = 0.3 *e*V is considered suitable [73]). The position of the donor HOMO level is also important in relation to the acceptor LUMO level and must be low enough to maximize $V_{OC}$ (see Equation 3). As a general rule, the HOMO energy is raised by electron-donating groups, while the LUMO energy is lowered by electron-withdrawing groups [52]. A decrease in the HOMO energy has also been observed through the addition of electron-withdrawing groups [74].

Another important quality in the design of new donors is high $\mu_h$, which is an important aspect of preventing charge losses due to recombination [37]. $\mu_h$ is influenced by the connectivity of the electron donor. One method to obtain high $\mu_h$ is to incorporate fused rings that experience $\pi$-$\pi$ stacking into the polymer [75–78]. A correlation between OPV efficiency and $\mu_h$ of the donor polymer has previously been suggested [72,79]. The correlation remains unclear however since the number of high mobility polymers that have been investigated in OPV devices is still limited.

Among electron acceptor building blocks for d-a molecules, 1,4-diketopyrrolo[3,4-*c*]pyrrole or diketopyrrolopyrrole (DPP) (Figure 10) has attracted considerable attention in the past few years. DPP was initially synthesized in 1974 for application as a pigment molecule [80] but its exceptional properties have since made it an impressive component in semiconductor materials. The DPP unit is well known for its strong $\pi$-$\pi$ bonding and, when associated with appropriate electron donating materials, strong intermolecular d-a interactions are known to occur. The resulting d-a molecules tend to have low band gaps, favourable energy levels and high hole mobilities, which are promising characteristics for OPV donor materials. DPP has been used for the construction of a large number of high performance organic semiconductors for OPVs [81–83]. Furthermore, several high mobility (i.e. $\mu_h > 0.1$ $cm^2V^{-1}s^{-1}$) DPP-based polymers have shown excellent photovoltaic performance, with PCEs exceeding 5% [15,84–88]. Recently, DPP-based molecules have been reported in organic thin film transistor (OTFT) applications with hole mobilities surpassing that of amorphous silicon [13,14].

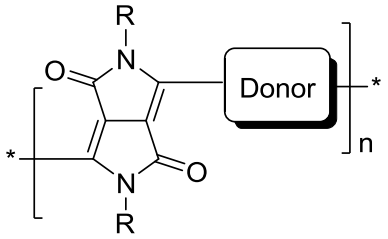


**Figure 10.** The general structure of a DPP-based donor-acceptor (d-a) molecule in which the DPP moiety acts as the acceptor, taken from [83].

## 1.5 Charge Carrier Mobility in OPVs

The charge carrier mobility ($\mu$) of both donor and acceptor materials plays a critical role in the operation of solar cells. $\mu$ influences such factors as charge extraction and transport, free charge recombination kinetics, as well as open circuit voltage [37]. The minimum acceptable $\mu$ in OPVs for both donor and acceptor is considered to be $10^{-4}$ $cm^2V^{-1}s^{-1}$ [33].

$\mu_h$ is influenced by several physical and chemical properties of the polymer. Some important properties necessary to achieve high mobility include easy delocalization of π-electrons, molecular planarity, as well as good electrochemical stability and reversibility [52]. In general, these factors influence the degree of crystallization, as well as the crystal orientation, which governs the direction of electron flow. In addition, the molecular weight of the polymer has also been found to influence the charge carrier mobility [70,79,89].

$\mu_h$ values for polymers are commonly drawn from analyses performed on transistors using the field-effect transistor (FET) method. This data provides potential candidates for OPV donors; however the results acquired from such methods do not necessarily reflect the actual μ within a solar cell device. This is due, in part, to differences in the geometry: the current within a transistor travels parallel to the substrate, whereas in the diode configuration (i.e. an OPV) current travels perpendicular to the substrate [89]. Common methods of measuring μ perpendicular to the substrate are charge extraction by linear increasing voltage (CELIV) [90] and space charge limited current (SCLC) [89,91]. The field-effect mobility values are normally higher than those produced using diode-based methods, such as SCLC, since OFETs operate with substantially higher charge carrier densities than diodes, which largely influences μ values [92,93].

Furthermore, in OPVs the $\mu_h$ of a donor is influenced dramatically by the presence and the nature of the electron acceptor. Blending of donor and acceptor materials has been found to decrease both $\mu_h$ and $\mu_e$ [94]. Unbalanced charge transport of holes versus electrons leads to space charge limited photocurrents [91,95,96], which usually hampers the cell performance by promoting charge recombination [97,98]. Balanced mobilities are even more crucial in the case of low band gap polymers, which have higher carrier densities [99]. In the case of BHJ solar cells utilizing high mobility donors, the charge transport balance is often achieved by increasing the concentration of the acceptor material (i.e. a fullerene derivative), thereby increasing the apparent $\mu_e$ [93].

## 1.6 Project Scope and Objectives

The main focus of this thesis is to explore the behaviour of high mobility semiconductor donors in the application of organic photovoltaics. Two DPP-based d-a copolymer analogues (Figure 11) have been selected as OPV donor candidates. They are of interest to study due to a) their analogous structure, which differs by only two electrons (sulfur versus oxygen), and b) their high field-effect hole mobilities, which is considered to be a critical property for the donor. Mobilities were demonstrated in organic thin film transistors (OTFTs) and are similar to that of amorphous silicon. Both polymers display favourable properties for OPVs that include optimal band gaps and ideal HOMO and LUMO energy levels. Despite their similarities, these polymers have many differences that will hopefully add to our knowledge of high mobility donors.

Process parameters such as casting solvent, active layer thickness, electron donor to acceptor ratio (D/A) and annealing conditions are critical variables in the fabrication of OPV devices. Optimization of these parameters leads to a higher PCE by maximizing the charge generation and transfer, while minimizing charge recombination. These process parameters will be addressed in an attempt to achieve high efficiency while exploring the potential benefits and/or limitations to the use of high mobility semiconductors in the field of OPVs.

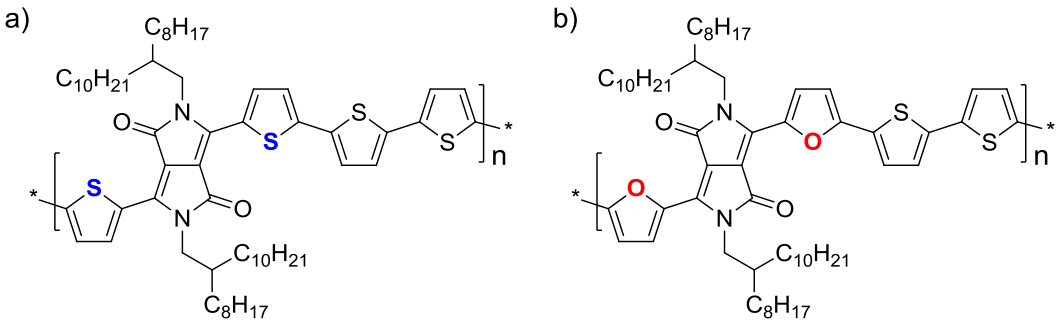


**Figure 11.** The chemical structures of DPP-based donor-acceptor polymers, a) PDQT and b) PDBFBT, to be investigated for compatibility as donor materials in OPVs.

# Chapter 2.

# Experimental Details

## 2.1 Materials

PDQT and PDBFBT were synthesized in-house by Dr. Wei Hong, according to the published procedures [76,100]. The number average molecular weight ($M_n$) and the polydispersity index (PDI) were measured by using a high-temperature gel-permeation chromatography (HT-GPC) at 140°C using 1,2,4-trichlorobenzene as eluent and polystyrene as standards. The $M_n$ and PDI of PDQT are 21,100 and 2.72, respectively and the $M_n$ and PDI of PDBFBT are 35,299 and 2.60, respectively. PEDOT:PSS (P VP AI 4083) was purchased from Clevios. $PC_{61}BM$ and $PC_{71}BM$ were purchased from 1-Material Inc. All other materials were purchased from Sigma-Aldrich and used without further purification.

## 2.2 Device Fabrication

*Substrate cleaning*: Glass substrates coated with indium tin oxide (ITO, ~15 Ω/square), purchased from Luminescence Technology Corporation, were cleaned by sonicating in acetone, soap solution (1% Micro 90 in water) and isopropyl alcohol then dried at 100°C overnight.

*Standard OPV device fabrication*: A 40-45 nm layer of PEDOT:PSS was spin-coated (3000 rpm, 60 s) onto cleaned ITO substrates followed by annealing at ~165°C for 10 min in air. The active layer was deposited in a glove box by spin-coating the active layer solution (20-40 mg/mL) at a certain speed for 60 s. Different thicknesses were obtained by varying the spin-coating speed. Samples were either allowed to dry slowly in a covered Petri dish in the glove box or thermal annealing was performed by heating the sample at a specified temperature for 10 min on a hot plate. A layer of LiF (~1 nm), followed by a layer of aluminum (~100 nm), were deposited by thermal evaporation through a shadow mask under a pressure of ~$10^{-5}$ mbar. The areas of the devices on each substrate were 0.1 $cm^2$, 0.125 $cm^2$ and 0.175 $cm^2$.

*Inverted OPV device fabrication*: A 30 nm layer of ZnO was deposited onto cleaned ITO substrates by spin-coating a zinc acetate solution (33 mg/mL) in ethanol and ethanolamine (0.9% v/v) at 700 rpm for 60 s, followed by annealing at ~180°C for 60 min in air. The active layer was then deposited

similarly to the procedure described for the standard devices. Slow drying or thermal annealing was performed similarly to the procedure described for the standard devices. A layer of MoO3 (~6 nm) and a layer of silver (~100 nm) were sequentially deposited by thermal evaporation through a shadow mask under a pressure of ~$10^{-5}$ mbar.

*Hole-Only device fabrication* (Figure 12a): A 40-45 nm layer of PEDOT:PSS was spin-coated (3000 rpm, 60 s) onto cleaned ITO substrates followed by annealing at ~165°C for 10 min in air. The active layer was then deposited with slow drying or thermal annealing as described above. A layer of MoO3 (~6 nm), followed by a layer of silver (~100 nm), were deposited by thermal evaporation through a shadow mask under a pressure of ~$10^{-5}$ mbar.

*Electron-Only device fabrication* (Figure 12b): A 30 nm layer of ZnO was deposited onto cleaned ITO substrates by spin-coating a zinc acetate solution (33 mg/mL) in ethanol and ethanolamine (0.9% v/v) at 700 rpm for 60 s, followed by annealing at ~180°C for 60 min in air. The active layer was then deposited with slow drying or thermal annealing as described above. A layer of LiF (~1 nm), followed by a layer of aluminum (~100 nm), were deposited by thermal evaporation through a shadow mask under a pressure of ~$10^{-5}$ mbar.

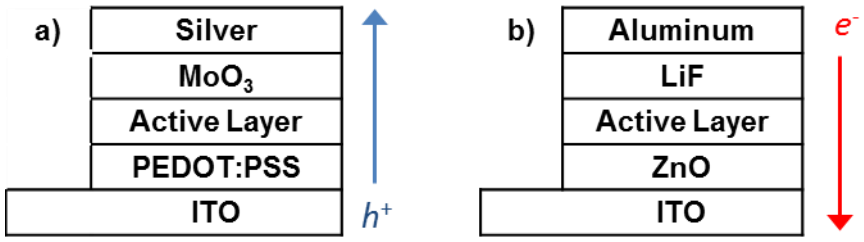


**Figure 12.** Structure of a) hole-only and b) electron-only devices.

## 2.3 Characterization

### 2.3.1 Film Thickness

Film thicknesses were measured using a Veeco Dektak 8 profiler at a tip force of 1- 3 mg.

### 2.3.2 Optical Measurements

Ultraviolet-visible (UV-Vis) absorption measurements were performed using a Thermo Scientific GENESYS$^{TM}$ 20 Spectrophotometer. The equipment measures the intensity of visible light passing through a sample. Conjugated molecules will absorb light at specific wavelengths. This is an indication of their HOMO and LUMO levels because longer wavelengths of light can be absorbed by molecules having a lower band gap. The band gap is calculated according to Equation 4, in which the onset of absorption ($\lambda_{onset}$) is determined from the UV-Vis spectrum. In the present work, experiments are carried out at room temperature on samples prepared as a thin film over glass.

$$E_g = \frac{1240}{\lambda_{onset}} \quad \textbf{(4)}$$

Transmittance (T) is calculated from absorbance (A) using the Beer-Lambert law:

$$\%T = 10^{(2-A)} \quad \textbf{(5)}$$

### 2.3.3 Film Morphology

Atomic force microscopy (AFM) imaging was carried out on a Dimension 3100 Scanning Probe Microscope. The equipment measures surface forces to provide a 3-D profile of a surface. A tip, located on a cantilever, interacts with the surface being measured. The surface forces cause displacement of the tip: the displacement is measured by a photodiode.

### 2.3.4 *J-V* Measurements

Current-voltage (*J-V*) analysis was conducted under simulated AM 1.5G irradiation (100 mW/cm$^2$) using an ABET Technologies Sun 2000 Solar Simulator. The equipment is used to generate current-voltage (*J-V*) curves under illumination and in the dark. Current is measured while varying voltage across the cell in a controlled manner using an applied load [29]. Shunt resistance ($R_{shunt}$) and series resistance ($R_{series}$) were extracted from the illuminated *J-V* characteristics using the two-diode analytical model [101].

### 2.3.5 SCLC Mobility Calculation

Hole and electron mobilities were calculated from the *J*-*V* characteristics of hole-only and electron-only devices measured in the dark, using the space charge limited current (SCLC) method [53,55–58]. Analysis of a log*J*–log*V* plot reveals a quadratic region that corresponds to the accumulation of space charge and is therefore considered trap-free. In this region, charge mobility is measured according to the Mott-Gurney equation [102–105]:

$$J = \frac{9}{8}\mu\varepsilon_0\varepsilon_r exp\left(\frac{0.89\beta}{\sqrt{L}}\sqrt{V_{eff}}\right)\frac{V_{eff}^2}{L^3} \quad \textbf{(6)}$$

where $J$ is the dark current density, $\mu$ is the carrier mobility under zero field, $\varepsilon_0$ is the permittivity of free space ($8.85 \times 10^{-12}$ F/m), $\varepsilon_r$ is the relative permittivity of the material (a value of 3 is assumed) [102,106,107], β is the field activation factor, $L$ is the distance between electrodes (i.e. thickness of the active layer plus buffer layers) and $V_{eff}$ is the effective voltage. $V_{eff}$ is calculated by subtracting a built-in voltage ($V_{bi}$) from the applied voltage ($V$), $V_{eff} = V - V_{bi}$, where a $V_{bi}$ of 0.1 V is assumed [108]. The fitting was performed over $V$ from 0.5 V to 5 V.

### 2.3.6 Cyclic Voltammetry

HOMO and LUMO energy levels of test molecules were estimated by cyclic voltammetry. The equipment consists of a potentiostat (Princeton Applied Research EPP-400) connected to three electrodes:

- The reference electrode (non-aqueous $Ag/Ag^+$) consists of a wire (Ag), glass tubing and a porous Teflon tip sealed to the glass tubing. The tubing was filled with a solution of silver nitrate ($AgNO_3$) dissolved in the buffer solution [109].
- The working electrode (Area = 0.03142 $cm^2$ platinum tip).
- The counter electrode (Area = 0.03142 $cm^2$ platinum tip).

The electrodes were immersed in a buffer solution containing 0.1 M tetrabutylammonium hexafluorophosphate ($Bu_4NPF_6$), ferrocene, which is used as a reference [110,111], and anhydrous acetonitrile. The test molecules were applied as thin films to the working electrode. Potential was applied between the reference and working electrodes while measuring current between the working and counter electrodes. Scans were run at a rate of 100 mV/s.

# Chapter 3.

# Polymer Properties and Characteristics

## 3.1 Introduction and Purpose

Based on the properties and characteristics presented in the literature, two DPP-based polymer analogues were selected to test in OPV applications. The first polymer, PDQT (Figure 11a), possesses a DPP-core flanked on either side by two thiophene units. Li *et al*. reported a high $\mu_h$ value (0.89 $cm^2V^{-1}s^{-1}$) of PDQT in OTFTs without the need for thermal annealing [76]. Thermal annealing of the polymer led to a slightly higher value of 0.97 $cm^2V^{-1}s^{-1}$. Other favourable properties of this polymer include a low band gap (1.2 eV) and compatible energy levels with those of $PC_{61}BM$ ($E_{HOMO}$ = -5.2 eV, $E_{LUMO}$ = -4.0 eV). UV-Vis-NIR absorbance showed the $\lambda_{max}$ at 790 nm. The non-annealed thin films were found to be highly crystalline with preferential edge-on chain orientation, as determined by X-ray diffraction (XRD) analysis. Liu *et al*. independently reported PDQT-based OPV devices with an efficiency of 5.6% using an active layer thickness of ~140 nm [85], thus demonstrating the high potential of this material in OPVs.

The second polymer, PDBFBT, is similar to PDQT but contains furan units in place of two of the thiophene units (Figure 11b) [100]. The furan moiety is known to lead to greater solubility than thiophene [71,112]. Other furan-based polymers have also been synthesized using DPP as a backbone; some of which have demonstrated good OPV performance [71,112–116]. PDBFBT demonstrated relatively high $\mu_h$ in OTFTs without annealing (0.13 $cm^2V^{-1}s^{-1}$), however after annealing the polymer thin films at 100, 150, and 200ºC, $\mu_h$ improved considerably to 0.51, 0.65, and 1.54 $cm^2V^{-1}s^{-1}$, respectively. The band gap of PDBFBT is greater than that of PDQT (1.41 *e*V) due to slight differences in the energy levels, with lower $E_{HOMO}$ and higher $E_{LUMO}$ values (-5.32 *e*V and -3.91 *e*V, respectively) than PDQT. The non-annealed thin film was found to be almost amorphous, as determined by XRD. Crystallinity was found to improve upon thermal annealing (100-220°C), with a random orientation of the polymer chains.

For high performance in OPVs, donor polymers must possess strong and broad absorption of light throughout the visible spectrum to maximize the $J_{SC}$, high $\mu_h$ to maximize the *FF*, and energy levels that are compatible with those of the acceptor in order to maximize the $V_{OC}$. These characteristics

will be analyzed in both polymers as they are investigated for their potential as donor materials with $PC_{61}BM$ as the acceptor. For comparative purposes, some of the properties of P3HT will also be measured.

## 3.2 Results and Discussion

The UV-Vis absorption spectra of PDQT, PDBFBT and P3HT are shown in Figure 13. Values were normalized by dividing by the film thickness. Based on equation 4, the optical band gap of PDQT and PDBFBT were estimated from Figure 13 to be 1.29 and 1.46, respectively. These results are similar, but slightly higher than the published results, suggesting that the polymers used in this study have slightly higher HOMO or slightly lower LUMO levels than the published references. This is to be expected since variations amongst batches often lead to differences in molecular weight and polydispersity, which will affect the energy levels. The optical band gap of P3HT was determined to be 1.94 eV, which is somewhat higher than the DPP-based polymers, indicating the greater energy requirement for exciton generation in P3HT compared to PDBFBT and PDQT.

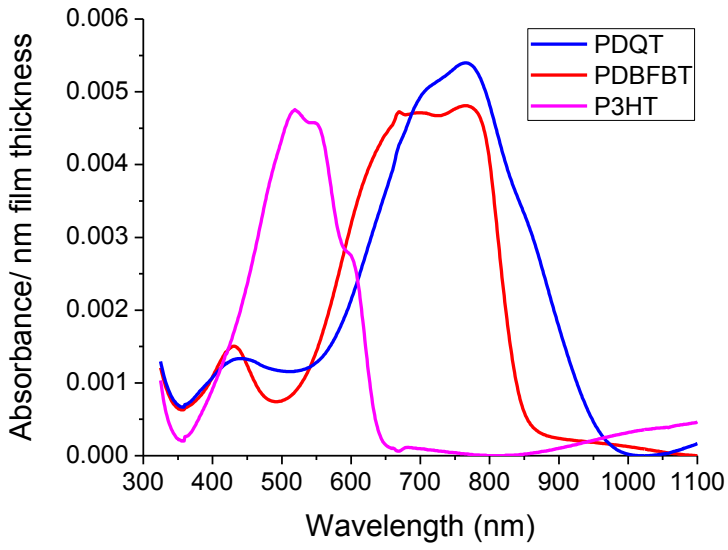


**Figure 13.** Normalized UV-Vis absorption spectra of thin films of PDQT, PDBFBT and P3HT. Absorbance was normalized by dividing by film thickness.

The pure PDQT film absorbs strongly in the region ranging from 600 to 950 nm, with maximum absorption at 770 nm. Similarly, the pure PDBFBT film absorbs strongly in the region ranging from 550 to 850 nm, with maximum absorption at 770 nm. P3HT, on the other hand, absorbs higher

energy photons at shorter wavelengths between 400 and 650 nm, with maximum absorption at 640 nm. P3HT exhibits negligible absorption beyond 650 nm, demonstrating the much broader absorbance of both DPP-based polymers. With the greater absorption range of the two DPP-based polymers, greater exciton generation and therefore greater $J_{SC}$ should be expected compared to P3HT.

Since $PC_{61}BM$ contributes mainly in the short wavelength region below 400 nm (refer to Figure 8), the DPP-polymer:$PC_{61}BM$ blends will result in a very narrow window (~400 nm to 500 nm) in which absorption is expected to be lowest. The greater absorption of $PC_{71}BM$ in the 400 to 600 nm range may therefore be beneficial for both PDBFBT and PDQT by allowing absorption of light throughout the entire visible spectrum.

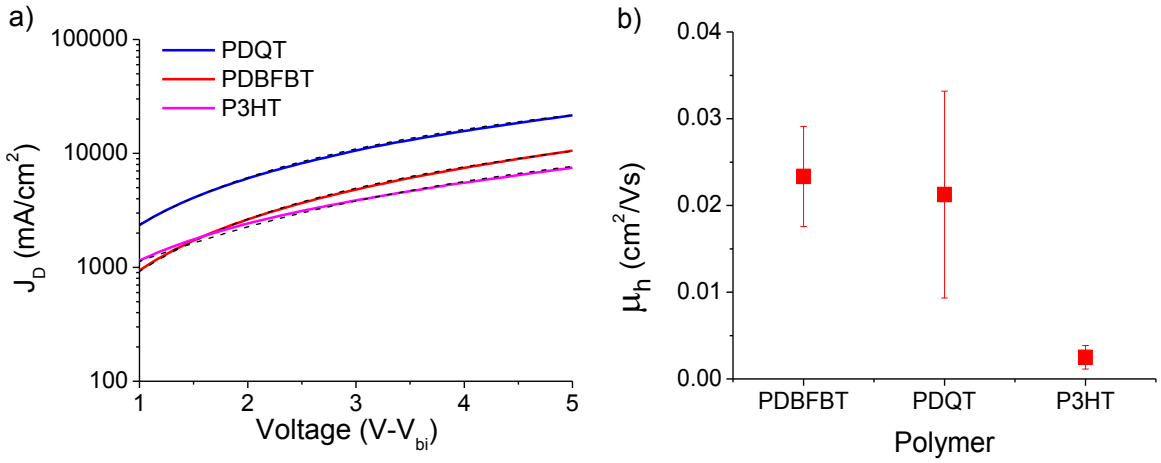


**Figure 14.** (a) *J-V* characteristics in the dark of pure polymers, PDBFBT, PDQT and P3HT. The polymer film thickness of each device was 351, 273 and 169 nm, respectively. The dashed black line represents fitting of the data to the modified Mott-Gurney equation for SCLC measurement of $\mu_h$. (b) Average $\mu_h$ of PDBFBT, PDQT and P3HT determined by the SCLC method.

SCLC $\mu_h$ was determined from hole-only devices that were prepared with as-cast polymer films. The modified Mott-Gurney equation (equation 5) was fit to the dark curve of each of the three polymers (Figure 14a). Figure 14b demonstrates that the SCLC $\mu_h$ of PDQT and PDBFBT are similar to each other ($2.1 \times 10^{-2}$ and $2.3 \times 10^{-2}$ $cm^2V^{-1}s^{-1}$, respectively) but are almost ten times higher than that of P3HT ($2.5 \times 10^{-3}$ $cm^2V^{-1}s^{-1}$). As expected, the SCLC mobilities are lower than the field-effect mobilities [76,100]. Interestingly, in non-annealed films PDQT has higher field-effect $\mu_h$ than PDBFBT but similar SCLC $\mu_h$, suggesting a similar crystal orientation in the vertical direction

between the polymers. Nevertheless, the high $\mu_h$ of these polymers suggests that high *FF* values can be achieved [117]. Moreover, higher $J_{SC}$ values can also be expected due to reduced recombination.

Suitable energy levels of all components within an OPV device are critical in order to favour hole and electron transfer to the appropriate electrodes. The LUMO-LUMO offset ($\Delta E_{LUMO}$) between donor and acceptor molecules is particularly significant in order for separation of the exciton to occur. $\Delta E_{LUMO} \sim 0.3$ *e*V is considered ideal [73] and the LUMO level of the donor must be higher than that of the acceptor in order to promote electron flow. The $E_{LUMO}$ value of $PC_{61}BM$ was found to vary throughout the literature from -3.7 to -4.3 *e*V [18,37,118–120]. The variation within this range could have a substantial impact on the suitability of PDBFBT and PDQT as donors. Given the published LUMO values of PDQT and PDBFBT are -4.0 and -3.91 *e*V, respectively, a LUMO value of -3.7 *e*V for $PC_{61}BM$ would in fact prevent exciton separation. $\Delta E_{LUMO}$ between PDQT and $PC_{61}BM$ was therefore measured by cyclic voltammetry (Figure 15) and was determined to be approximately 0.3 *e*V. The $E_{LUMO}$ of $PC_{61}BM$ was therefore determined to be -4.3 *e*V and $\Delta E_{LUMO}$ for PDBFBT:$PC_{61}BM$ was estimated to be approximately 0.39 eV. The LUMO values of both DPP-based polymers are thus considered to be ideal for exciton separation and electron transfer.

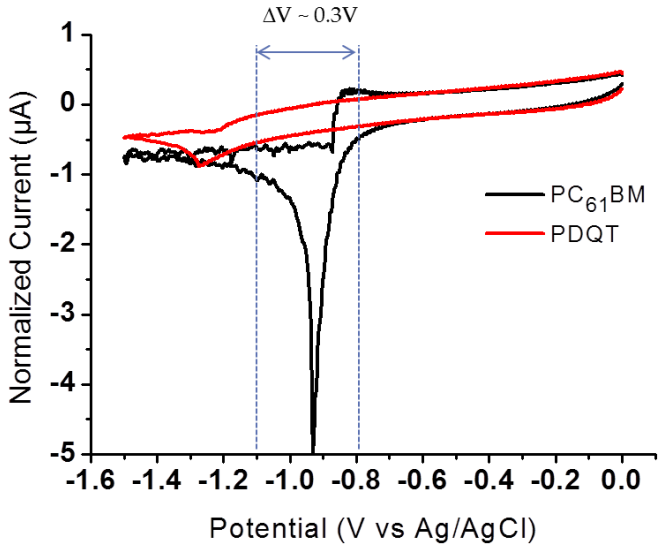


**Figure 15.** Cyclic voltammograms of PDQT and $PC_{61}BM$ films showing the LUMO-LUMO offset.

Using the LUMO levels and band gaps calculated in this study, the HOMO values were reassessed and determined to be -5.29 and -5.37 *e*V for PDQT and PDBFBT, respectively. Figure 16 depicts the

energy level diagrams of these polymers in both inverted and standard OPV device architectures. Based on these energy levels, $V_{OC}$ values were predicted utilizing Equation 3 [37]. The $V_{OC}$ value of PDQT:$PC_{61}BM$ devices was predicted to be 690 mV, while the $V_{OC}$ value of PDBFBT:$PC_{61}BM$ devices was predicted to be 770 mV. These values are relatively high considering the $V_{OC}$ of P3HT is generally below 660 mV [35]. Furthermore, the marked difference in $V_{OC}$ between the two DPP-based polymers could potentially result in a higher PCE in PDBFBT devices.

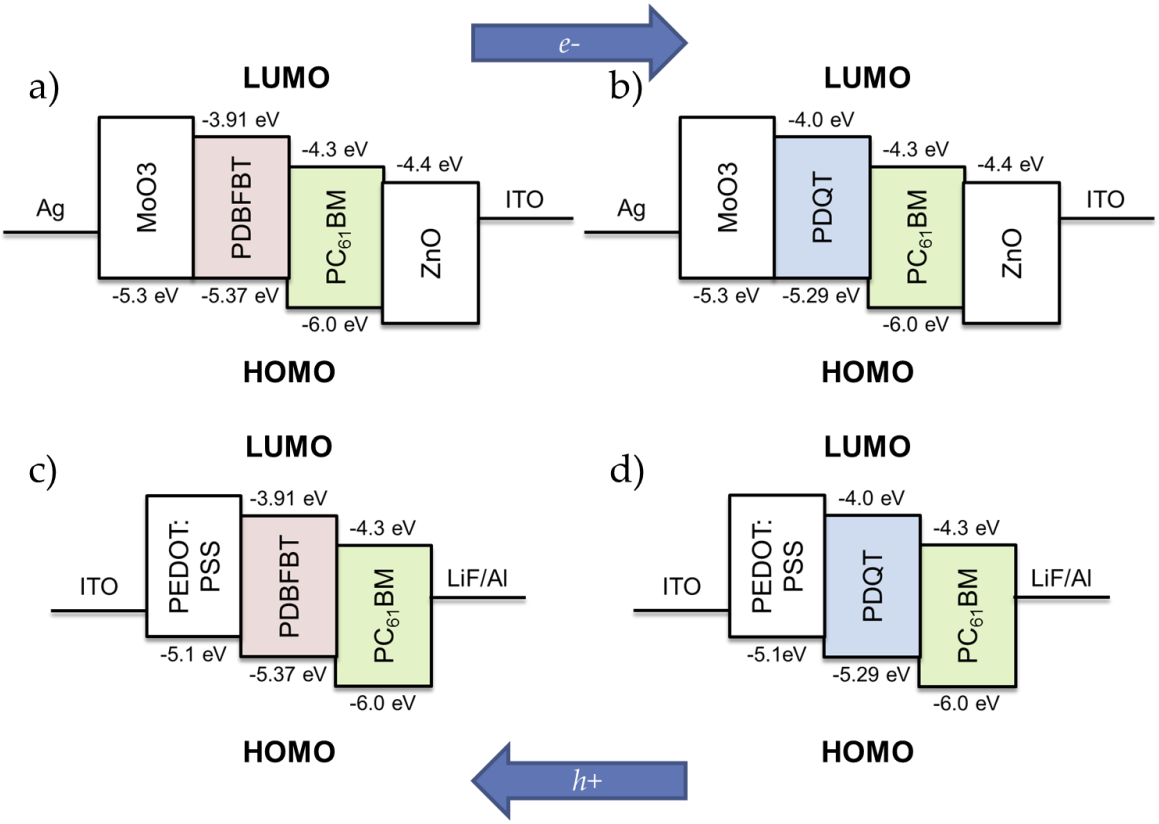


**Figure 16.** Energy level diagrams for inverted OPV devices with a) PDBFBT and b) PDQT as donor, and standard OPV devices with c) PDBFBT and d) PDQT as donor. HOMO and LUMO levels of other materials were adapted from literature values [18,37,76,100,118–120].

A method to predict PCE was developed by Dennler *et al.* [121], based on the donor band gap and $\Delta E_{LUMO}$ of the donor and acceptor (Figure 17). According to this method, P3HT, which has a $\Delta E_{LUMO}$ of ~1 *e*V and a band gap of ~ 1.9 *e*V [122], can be expected to have a PCE of ~ 4-5%. This is somewhat lower than some of the actual values that have been reported (up to 6.5% [123,124])

however in line with the majority of results achieved throughout the literature [35]. For PDQT, the $\Delta E_{LUMO}$ of 0.3 *e*V and a band gap of 1.29 *e*V led to a predicted PCE of 10%. For PDBFBT, due to the greater $\Delta E_{LUMO}$ of 0.39 *e*V and the greater band gap of 1.46 *e*V, a slightly lower PCE of 9% was predicted.

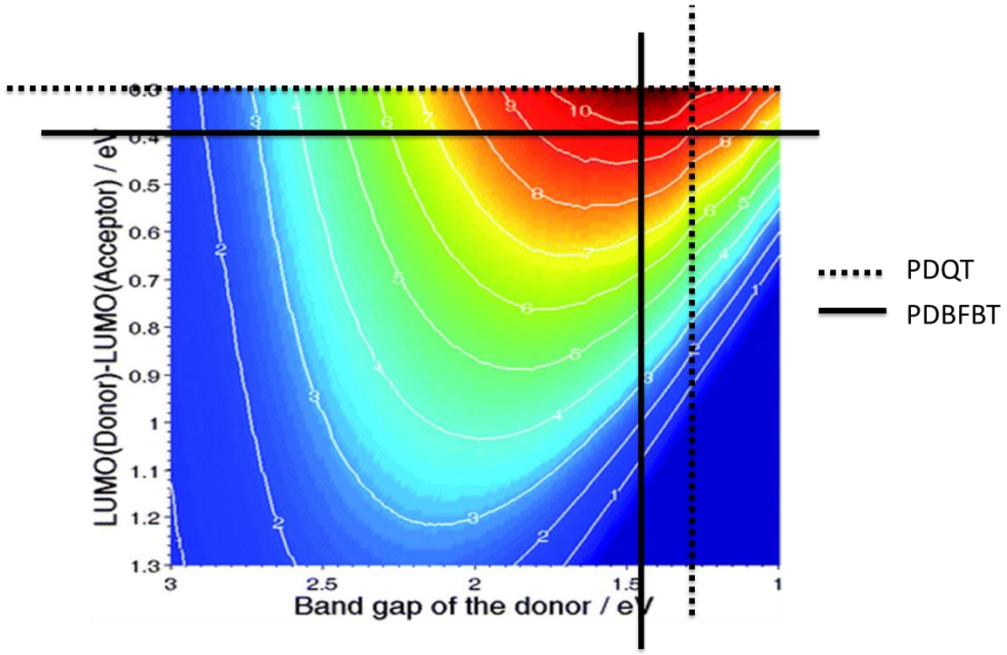


**Figure 17.** Predicted PCE of PDQT (dashed line) and PDBFBT (solid line) under AM1.5G illumination for BHJ devices based on the donor band gap and the LUMO-LUMO offset between the donor and acceptor, adapted from [121].

The above model unfortunately does not account for variables such as the molecular weight ($M_n$) and polydispersity (PDI) of the donor. These factors are known to have a significant influence on OPV performance, which tends to favour higher $M_n$ values [70,79,125–127]. Table 1 shows the $M_n$ and PDI values of both polymers. It can be seen that the polymers have similar PDIs but the $M_n$ value of PDQT is lower than that of PDBFBT. In comparison, a recent report, in which PDQT achieved a PCE of 5.62%, expressed considerably higher $M_n$ and PDI values of 73,000 and 4, respectively [85]. It is not clear how the lower $M_n$ and PDI values will manifest considering the high mobility that the polymer possesses.

**Table 1.** Summary of measured and estimated optical and electrical properties of PDQT, PDBFBT and P3HT.

| | **PDQT** | **PDBFBT** | **P3HT** |
|---|---|---|---|
| Eg (*e*V) | 1.29 | 1.46 | 1.94 |
| $\lambda_{max}$ (nm) | 770 | 770 | 640 |
| SCLC $\mu_h$ ($cm^2V^{-1}s^{-1}$) | $2.1 \times 10^{-2}$ | $2.3 \times 10^{-2}$ | $2.5 \times 10^{-3}$ |
| HOMO (*e*V) | -5.29 | -5.37 | n/a |
| LUMO (*e*V) | -4.0 | -3.91 | n/a |
| $M_n$ | 21,100 | 35,299 | n/a |
| PDI | 2.72 | 2.60 | n/a |

## 3.3 Conclusions

Overall, the two DPP-based semiconductors, PDQT and PDBFBT, appear to be suitable candidates for the role of donor in OPVs. Both polymers demonstrate complimentary energy levels to those of $PC_{61}BM$. The relatively low HOMO values suggest that a high $V_{OC}$ is possible for both polymers; however a higher $V_{OC}$ is expected in PDBFBT devices. High SCLC $\mu_h$ of both polymers has been demonstrated in the vertical direction, suggesting high *FF* and $J_{SC}$ are achievable. Finally, it is expected that $J_{SC}$ can also be high as a result of the strong and broad absorption spectra of both polymers. With proper optimization of the processing parameters, there is potential for these polymers to achieve PCEs of 9% or greater.

# Chapter 4.

# Selection of Casting Solvent

## 4.1 Introduction and Purpose

In solution-processed BHJ solar cell fabrication, the choice of casting solvent is known to dramatically influence factors such as BHJ morphology and light absorption [128–131]. The role of the solvent is to dissolve both donor and acceptor so that ideally sized nanodomains can be formed to maximize charge transport. The boiling point of the casting solvent is an important characteristic that dictates the evaporation rate during spin-coating and drying. With P3HT, the use of solvents with a high boiling point leads to a higher degree of structural organization due to slower drying and thus better crystallization [130,132–134]. Due to their excellent solubilizing capability and their high boiling points, chlorobenzene and dichlorobenzene are two of the most commonly used solvents in solution-processed OPVs.

In OPV studies of DPP-based polymers, the most frequently used solvents are chloroform and ortho-dichlorobenzene (DCB), often used together in a 4:1 (v/v) ratio [15,58,67,71,84,115,135–138]. The presence of chloroform is quite often necessary for DPP-based polymers due to their poor solubility in other solvents. Device efficiency has also been shown to improve with process additives such as 1,8-diiodooctane (DIO) and 1-chloronaphthalene (CN), which significantly improve cell performance by providing a much finer phase separation [71,84,86,131,139–143]. For the additive to perform this function, it must be a poor solvent for the donor and a better solvent for the fullerene acceptor. In addition, the additive must have a higher boiling point than the parent solvent [140]. In the following study, PDQT and PDBFBT have been tested using various solvent systems, with and without the presence of an additive.

## 4.2 Results and Discussion

### 4.2.1 PDBFBT

PDBFBT is much more soluble than PDQT due to the presence of the furan moieties. An active layer consisting of PDBFBT:$PC_{61}BM$ (D/A = 1/3) was prepared using three different solvent systems.

Binary solvent mixtures consisting of chloroform/DCB (4:1 v/v) or 1,1,2,2-tetrachloroethane (TCE)/DCB (4:1 v/v) were tested, along with DCB alone. The boiling point of chloroform, TCE and DCB are 61.2°C, 146.5°C and 180.5°C, respectively. The presence of DCB is important because it is a good solvent for dissolving $PC_{61}BM$. Additionally, it is well known for its ability to allow slow drying and thus provide better crystallization. Chloroform/DCB (4:1 v/v) was chosen due to its prevalence in the literature since DPP-based polymers tend to solubilize well in chloroform. Finally TCE/DCB (1:4 v/v) was chosen because TCE was found to have similar solubilizing capabilities as chloroform yet has a high boiling point that could potentially improve the morphology. The processing additive, DIO, was used in each solvent system with varying percentages (0-2%). Inverted OPV devices were prepared by spin-coating the active layer solution at a specific rate and allowing the solution to dry slowly in the glove box for ≥ 3 hours.

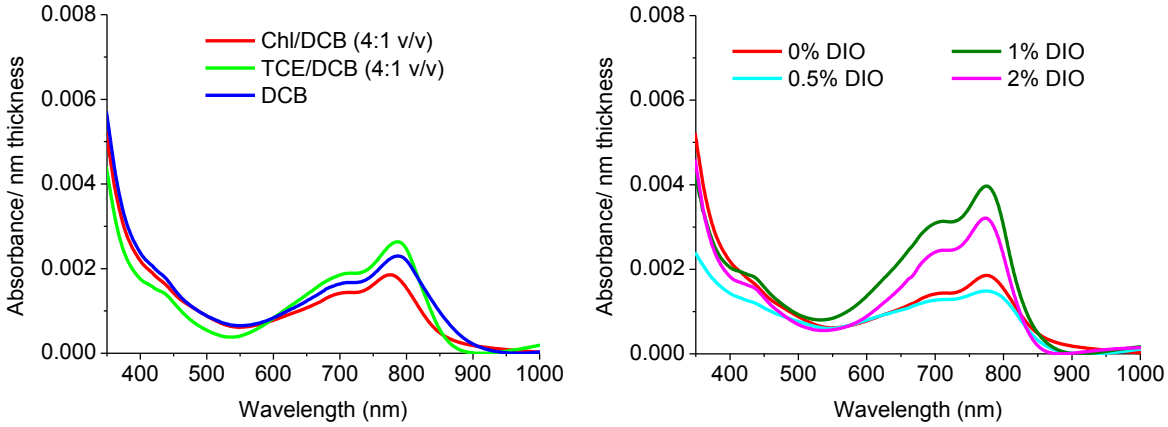


**Figure 18.** Normalized UV-Vis absorption spectra of PDBFBT:$PC_{61}BM$ (D/A = 1/3) thin films prepared using a) different solvent systems (chloroform/dichlorobenzene (4:1 v/v), tetrachloroethane/dichlorobenzene (4:1 v/v) and dichlorobenzene), and b) chloroform/ dichlorobenzene (4:1 v/v) with varying quantities of additive, 1,8-diiodooctane (DIO). Absorbance was normalized by dividing by film thickness.

UV-Vis absorbance was measured on the films prepared using each of the different solvent systems (Figure 18a). The greatest absorbance occurs in the film prepared using TCE/DCB (4:1 v/v) and the lowest absorbance occurs in the film prepared using chloroform/DCB (4:1 v/v). Generally the maximum optical absorption of a polymer is directly related to the degree of its crystallinity [144]. This indicates that the use of solvents with a high boiling point leads to improved crystallization of PDBFBT. Although TCE has a lower boiling point than DCB, the presence of TCE is expected to

improve the solubility of PDBFBT. Moreover, small changes to the quantity of DIO in the chloroform/DCB (4:1 v/v) solvent blend can significantly influence the crystallinity of PDBFBT (Figure 18b). Although 1% (v/v) DIO improves the crystallinity of PDBFBT, 0.5% DIO reduces the degree of crystallinity compared to that of films prepared without DIO.

Analysis of the OPV devices was performed by illuminated and dark *J-V* measurements (Figure 19) from which device parameters were determined (Table 2). Overall, $V_{OC}$ was highest in devices prepared using the chloroform/DCB solvent system. The highest value of 744 mV was achieved without the addition of DIO and is slightly lower than the predicted $V_{OC}$ of 770 mV. *FF*, on the other hand was quite high in devices prepared using the TCE/DCB solvent system, with an extremely high *FF* of 68.54% achieved using 1% DIO. A high *FF* was expected to occur as a result of the high $\mu_h$ of this polymer. The highest $J_{SC}$ value (10.06 $mAcm^{-2}$) was found using DCB as solvent with 2% DIO, however the relatively low *FF* and $V_{OC}$ brought the PCE below 3%. The highest overall PCE (3.48%) was achieved using a solvent system consisting of TCE/DCB + 2% DIO. Similarly the highest PCE within each solvent system was achieved using 2% DIO. The lower than predicted PCE is due mainly to the low $J_{SC}$. To achieve a PCE near the predicted value, a $J_{SC}$ value closer to 20 $mAcm^{-2}$ is required.

Active layer thicknesses amongst devices were inconsistent, ranging from the thinnest active layer of 180 nm to the thickest active layer of 578 nm (Table 2). Certainly the thickness of the active layer is known to influence the device efficiency due to the interplay between increased absorption and increased recombination. Figure 20 demonstrates the relationship between active layer thickness and PCE, comparing the various ratios of DIO, regardless of the solvent system. There is a clear difference between the devices prepared with higher DIO ratios (1 and 2%) compared with the devices prepared with lower DIO ratios (0 and 0.5%). This is particularly noticeable at the lower active layer thicknesses (i.e. < 400 nm).

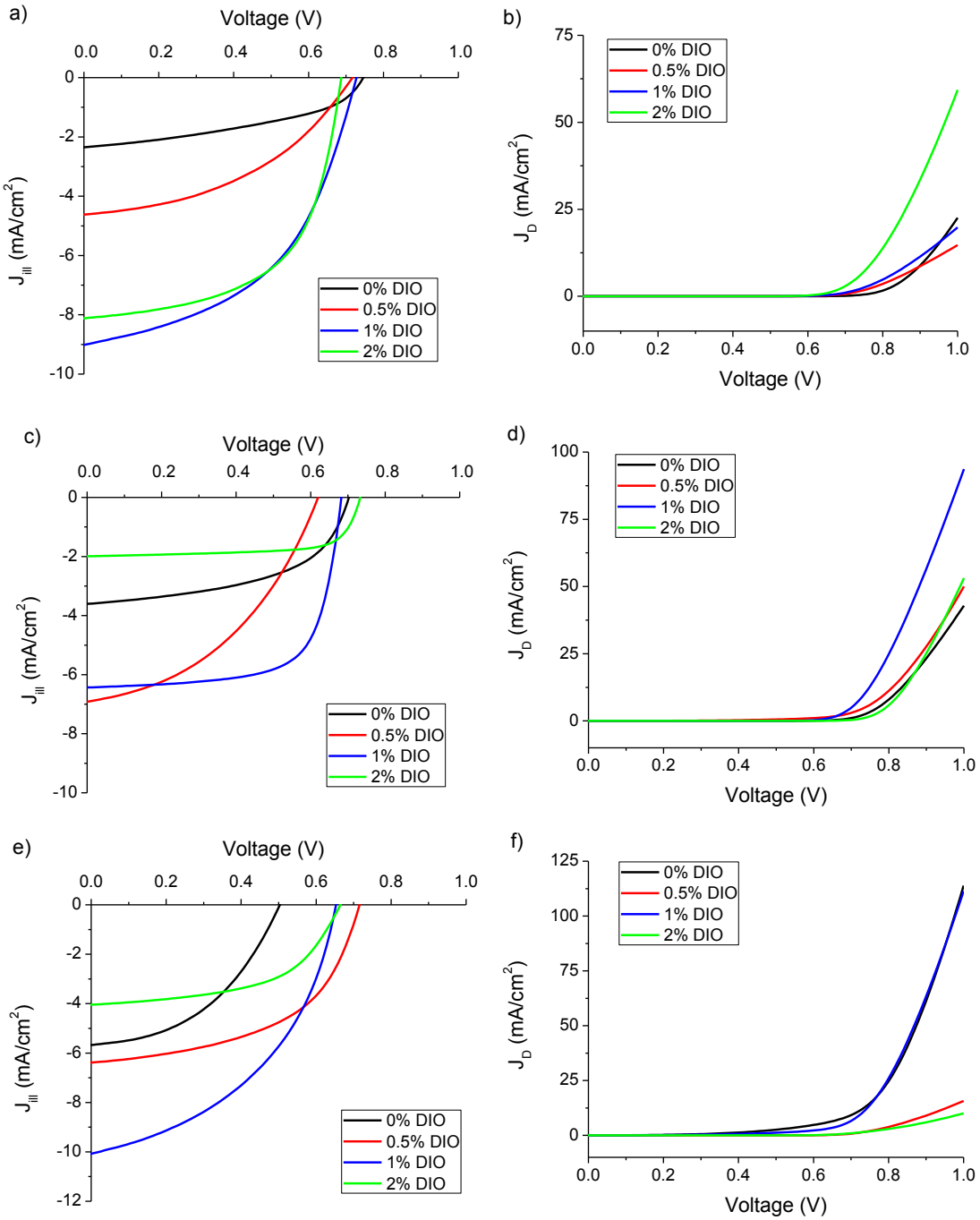


**Figure 19**. *J-V* characteristics of inverted OPV devices prepared with PDBFBT:$PC_{61}BM$ (D/A = 1/3) using different solvent systems with varying amounts of DIO. a) Illuminated and b) dark curves of devices prepared with chloroform/DCB (4:1 v/v); c) illuminated and d) dark curves of devices prepared with TCE/DCB (4:1 v/v); e) illuminated and f) dark curves of devices prepared with DCB.

**Table 2.** Efficiency parameters of OPV devices prepared using PDBFBT:$PC_{61}BM$ (D/A = 1/3) in different solvent systems. 1,8-diiodooctane (DIO) was used as an additive in each solvent system, its concentration varying from 0-2% (v/v).

| Casting Solvent | %DIO (v/v) | Thickness (nm) | $J_{SC}$ ($mAcm^{-2}$) | $V_{OC}$ (mV) | *FF* (%) | PCE (%) |
|---|---|---|---|---|---|---|
| Chloroform/DCB (1:4 v/v) | 0 | 300 | 1.88 | 744 | 44.35 | 0.62 |
| | 0.5 | 450 | 4.42 | 714 | 42.18 | 1.33 |
| | 1 | 578 | 8.94 | 724 | 48.83 | 3.16 |
| | 2 | 372 | 8.03 | 687 | 57.62 | 3.18 |
| TCE/DCB (1:4 v/v) | 0 | 180 | 3.05 | 706 | 58.9 | 1.25 |
| | 0.5 | 180 | 1.92 | 738 | 67.69 | 0.96 |
| | 1 | 207 | 6.34 | 681 | 68.45 | 2.96 |
| | 2 | 554 | 9.02 | 680 | 56.73 | 3.48 |
| DCB | 0 | 272 | 4.1 | 662 | 55.29 | 1.50 |
| | 0.5 | 405 | 6.24 | 722 | 54.02 | 2.43 |
| | 1 | 378 | 5.67 | 503 | 44.82 | 1.28 |
| | 2 | 254 | 10.06 | 652 | 45.28 | 2.97 |

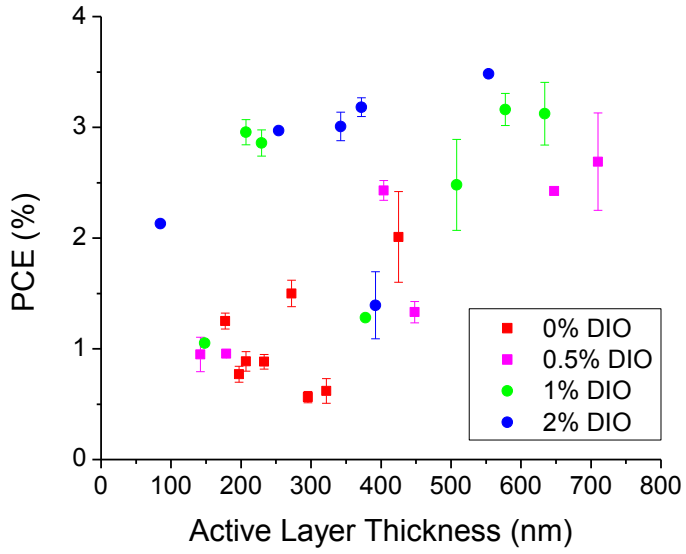


**Figure 20.** Relationship between active layer thickness and PCE of OPV devices prepared using PDBFBT:$PC_{61}BM$ with various percentages of DIO as solvent additive. Various solvent systems (Chloroform/DCB, TCE/DCB and DCB) are represented in each category.

The choice of solvent system was found to greatly influence the active layer thickness. The high boiling solvents (TCE, DCB) did not dry fast enough during spin-coating to achieve thick active layers. Due to the volatility of chloroform, active layer thickness was more easily controlled and a broader range of thicknesses was achievable.

AFM images (Figure 21) demonstrate that the level of DIO in the solvent greatly affects the nanophase separation, as well as the surface roughness (RMS) of the active layer film. Films prepared without DIO show large domain sizes (~1 µm in some cases) with very rough surfaces (> 18 nm). The amount of DIO affects the film morphology obtained with each solvent system differently. Devices prepared with DCB show appropriate morphological features using all tested DIO quantities. Devices prepared with TCE/DCB, on the other hand, show acceptable morphology only with the 1% DIO solvent mixture. Chloroform/DCB films show the best morphology with 1% and 2% DIO. This supports the *J-V* results favouring the higher DIO concentration.

With the benefits of the chloroform/DCB (i.e. better control of active layer thickness) and the similar results of 1% and 2% DIO achieved in this system, a solvent mixture consisting of chloroform/DCB + 1% DIO is recommended as the ideal choice for PDBFBT:$PC_{61}BM$ BHJs.

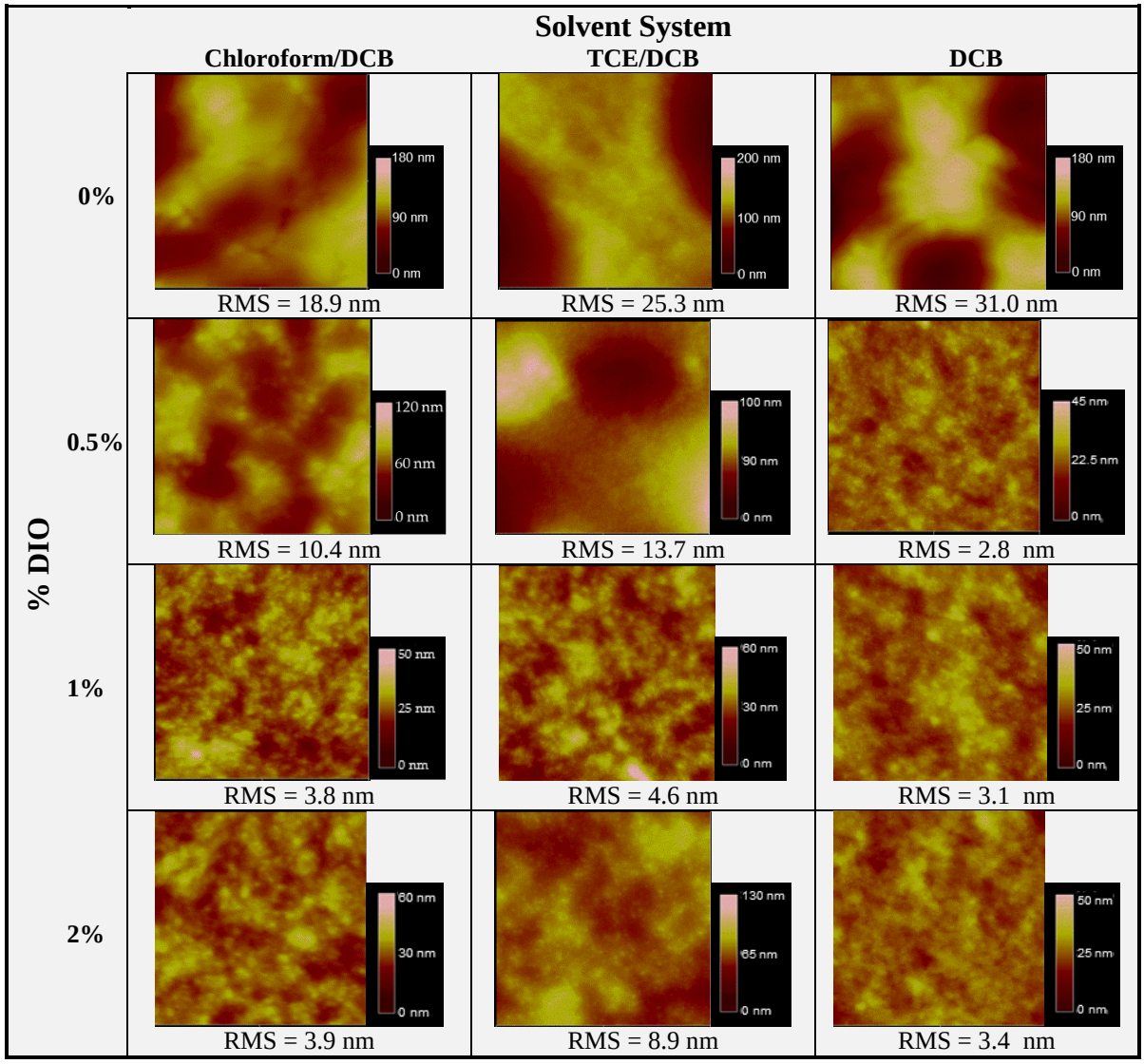


**Figure 21**. AFM images (2 μm × 2 μm) of the active layers of OPV devices prepared with PDBFBT:$PC_{61}BM$ (D/A = 1/3) using different solvent systems and varying amounts of DIO.

### 4.2.2 PDQT

The solubility of PDQT was found to be quite low and required the presence of chloroform for dissolution. Based on the solvent selection for PDBFBT, selection of the casting solvent for PDQT was narrowed down to chloroform/DCB (4:1 v/v) due the ability to control active layer thickness better using the low boiling point solvent. Inverted OPV devices were prepared with varying ratios of DIO and performance was measured to determine the ideal amount of DIO.

*J-V* characteristics of inverted OPV devices were measured under illumination and in the dark (Figure 22). Efficiency parameters were determined from illuminated *J-V* characteristics (Table 3). The highest $V_{OC}$ of 667 mV was achieved without the addition of DIO and is slightly lower than the predicted values of 690 mV. The highest *FF* of 62.5% is fairly high and was also achieved without the addition of DIO. The highest $J_{SC}$ of 6.25 $mAcm^{-2}$ was found using a concentration of 2% DIO. The highest PCE of 2.18% was achieved in devices prepared using 2% DIO, however the variation in PCE amongst the devices prepared with different DIO percentages was low. Despite the highest $V_{OC}$ and *FF*, the performance of devices prepared without the solvent additive was inferior to all devices prepared using DIO. Figure 23a demonstrates the slightly higher PCE achieved with 2% DIO compared with 0.5% DIO. Figure 23b demonstrates the influence of active layer thickness, in which it can be seen that devices prepared with 2% DIO performed better at similar active layer thicknesses than devices prepared with 1% DIO.

**Table 3.** Efficiency parameters of OPV devices prepared using PDQT:$PC_{61}BM$ (D/A = 1/3) in chloroform/DCB with varying amounts of 1,8-diiodooctane (DIO).

| Casting Solvent | %DIO (v/v) | Thickness (nm) | $J_{SC}$ ($mAcm^{-2}$) | $V_{OC}$ (mV) | *FF* (%) | PCE (%) |
|---|---|---|---|---|---|---|
| Chloroform/DCB (1:4 v/v) | 0 | 126 | 2.20 | 663 | 61.9 | 0.90 |
| | 0 | 117 | 2.06 | 667 | 62.5 | 0.86 |
| | 0.5 | 255 | 5.56 | 644 | 56.1 | 2.01 |
| | 0.5 | 311 | 4.86 | 635 | 47.8 | 1.48 |
| | 1 | 313 | 5.96 | 636 | 46.7 | 1.77 |
| | 1 | 504 | 4.86 | 635 | 47.8 | 1.48 |
| | 2 | 379 | 6.25 | 643 | 54.3 | 2.18 |
| | 2 | 515 | 5.85 | 643 | 47.6 | 1.79 |

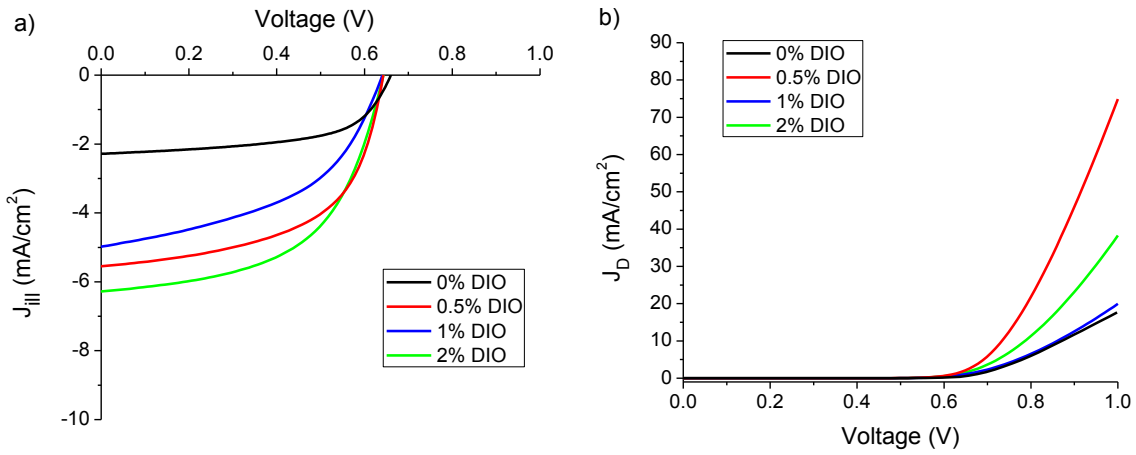


**Figure 22.** *J-V* characteristics measured under a) illumination and b) dark, of inverted OPV devices prepared with PDQT:$PC_{61}BM$ (D/A = 1/3) and chloroform/DCB (4:1 v/v) with varying amounts of DIO.

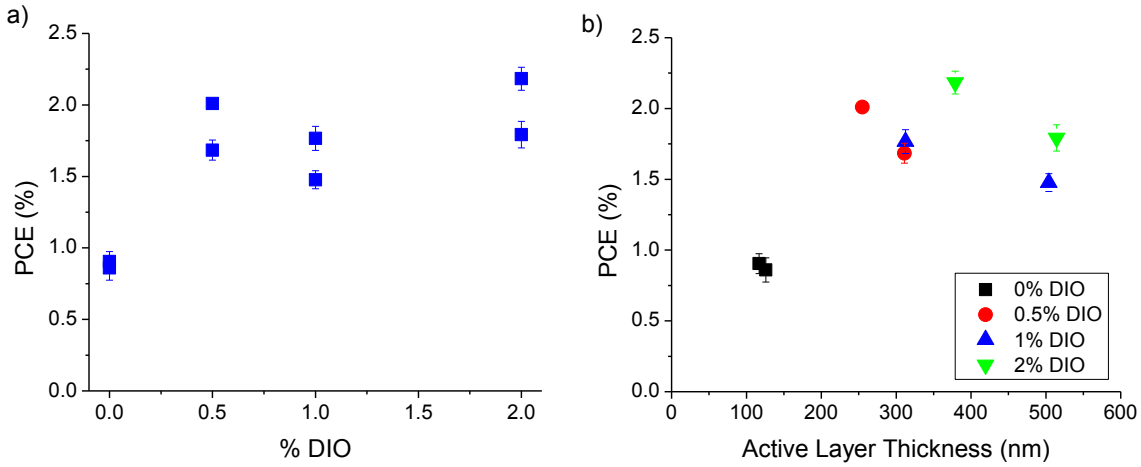


**Figure 23.** a) Relationship of PCE and % DIO of inverted devices prepared using a casting solvent of chloroform/DCB (4:1 v/v) with varying ratios of DIO. Each data point represents a different active layer thickness. b) Relationship of PCE and active layer thickness of inverted devices prepared using a casting solvent of chloroform/DCB (4:1 v/v) with varying ratios of DIO.

Figure 24 shows AFM images of the films prepared with various concentrations of DIO (0-2%). There is little difference in morphology amongst those films containing DIO. The film prepared without DIO however shows greater domain sizes, confirming the necessity of DIO in the solvent mixture for better nanophase separation.

The use of DIO as an additive appears to be required for good performance in PDQT:$PC_{61}BM$ devices. The differences amongst devices prepared with varying DIO concentrations are subtle and therefore the quantity of DIO may not play a significant role in morphological improvements. For this reason, a solvent mixture consisting of chloroform/DCB + 0.5% DIO is recommended as the ideal choice for PDQT:$PC_{61}BM$ BHJs.

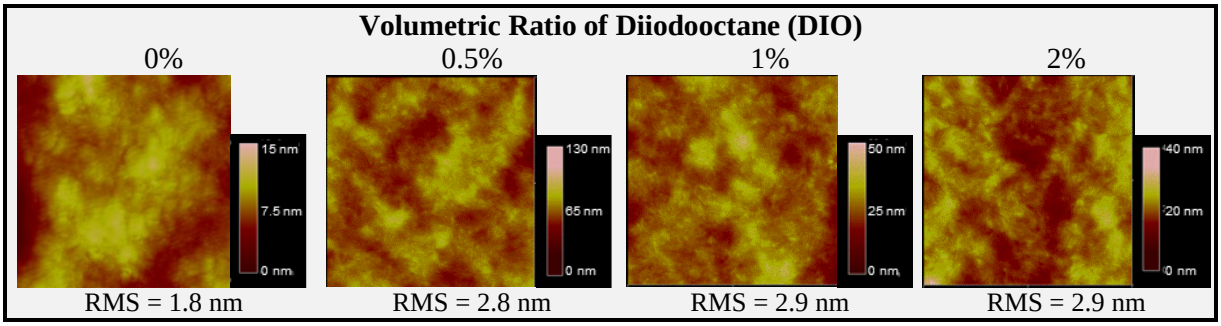


**Figure 24**. AFM images (2 µm × 2 µm) of the active layers of OPV devices prepared with PDQT:$PC_{61}BM$ (D/A = 1/3) using a mixture of chloroform/DCB (4:1 v/v) as the casting solvent with varying amounts of DIO (0%, 0.5%, 1% and 2% by volume).

## 4.3 Conclusions

The ideal solvent systems for PDBFBT:$PC_{61}BM$ and PDQT:$PC_{61}BM$ blends require the presence of chloroform for improved solubility and to allow better control of the active layer thickness. The presence of DCB is also required for dissolution of $PC_{61}BM$. In both blends of polymer:$PC_{61}BM$, the addition of DIO is important for improved morphology. For PDBFBT a greater DIO concentration (1% and 2%) demonstrates better PCE and improved morphology. For PDQT the concentration of DIO does not significantly influence the film morphology and PCE does not vary considerably. Therefore, the solvent system that will subsequently be used for PDBFBT:$PC_{61}BM$ devices is chloroform/dichlorobenzene (4:1 v/v) + 1% DIO, whereas the solvent system to be used for PDQT:$PC_{61}BM$ devices is chloroform/dichlorobenzene (4:1 v/v) + 0.5% DIO.

# Chapter 5.

# Donor-Acceptor Ratio and Thickness of the Active Layer

## 5.1 Introduction and Purpose

Increasing the active layer thickness of OPVs is customarily envisioned as a method to improve device efficiency through greater light absorption and thus, increased exciton generation. In theory, $J_{SC}$ increases with increasing charge generation or photon absorption, and thus thicker active layers would be beneficial. For the majority of high efficiency OPVs, however, the optimal thickness for best performance is around 100 nm [59,145–150]. A slight change to the optimal active layer thickness normally causes a dramatic drop in the photovoltaic performance. From a manufacturing perspective, very thin active layers and a narrow window of tolerable thickness (i.e. a few tens of nm) present formidable challenges in high throughput roll-to-roll processing [19,122].

One of the greatest obstacles to achieving thick active layers is the inability of electrons and holes to traverse the increased distance due to charge recombination that originates from low charge carrier mobilities of the donor and acceptor materials. High charge carrier mobility ($\sim 10^{-3}$ $cm^2V^{-1}s^{-1}$ or greater) is therefore necessary to prevent charge losses if the active layer thickness reaches several hundred nanometers [37].

P3HT is generally considered to be a high mobility polymer, with reported field-effect $\mu_h$ up to 0.1 $cm^2V^{-1}s^{-1}$ in OTFTs [151]. PCEs greater than 6.5% have been reported for OPVs using P3HT as the donor [123,124]. Furthermore, relatively high PCE has previously been achieved in OPV devices with active layers just over 300 nm using a blend of P3HT and $PC_{61}BM$ [23,152]. More recently, it was demonstrated that P3HT:PCBM OPV devices could maintain consistent PCEs at active layer thicknesses up to and beyond 800 nm [153,154]. Since PDQT and PDBFBT have considerably higher SCLC $\mu_h$ than P3HT, it is expected that thick active layers can be achieved using these polymers as the donor.

The influence of the D/A ratio was also investigated in conjunction with active layer thickness. Due to the high $\mu_h$ values of PDQT and PDBFBT, it is expected that a fairly high content of acceptor will be required to balance charge mobility. For high mobility DPP-based molecules (i.e. field-effect $\mu_h$

similar to that of P3HT $\geq$ 0.1 $cm^2V^{-1}s^{-1}$), the most commonly used D/A ratio to achieve optimal charge balance with PCBM as the acceptor is 1/2 [15,67,71,115].

## 5.2 Results and Discussion

To study the absorption characteristics of the active layer, PDQT:$PC_{61}BM$ and PDBFBT:$PC_{61}BM$ films of various D/A ratios and thicknesses were prepared and analyzed by UV-Vis absorption measurements (Figure 25 & Figure 26, respectively). Transmittance values at 770 nm, where the maximum absorption of both polymers is located, are plotted against active layer thickness (Figure 25e & Figure 26e). As expected, transmittance in both polymers decreases exponentially with increasing active layer thickness. Therefore, for an OPV comprising a material blend of PDQT:$PC_{61}BM$, the vast majority of exciton generation (~90%) is expected to occur within the first 250 nm of the active layer for the highest D/A ratio of 1/1, and 450 nm for the lowest D/A ratio of 1/4. Considering that the transmittance values were taken at the maximum absorption, the PDQT:$PC_{61}BM$ active layer thickness is required to be greater than ~250-450 nm, depending on the D/A ratio, in order to harvest the majority of sunlight. Similarly, for the PDBFBT:$PC_{61}BM$ material blend, depending on the D/A ratio, the active layer thickness is required to be greater than ~200-400 nm in order to harvest the majority of sunlight.

The polymer:$PC_{61}BM$ blends with varied thickness were first tested in OPVs having a standard configuration. Figure 27 shows the PCE and related parameters (*FF*, $J_{SC}$, and $V_{OC}$) for devices prepared using PDQT:$PC_{61}BM$. The PCE for the D/A = 1/1 devices reached a maximum value of 1.1% at a thickness of 375 nm, but was considerably lower (only 0.1%) for the devices with the thickest active layer (~800 nm). Devices with D/A ratios of 1/2 and 1/3 showed similar trends to the devices with D/A = 1/1. In general, the PCE for all of the D/A = 1/3 devices was considerably higher than other D/A ratios, with the maximum PCE of 1.9% achieved at a relatively high thickness of 300 nm. In contrast to other ratios, the PCE of the D/A = 1/4 devices was highest at the lowest thickness of ~100 nm, but also dropped as the thickness was increased. Thus it appears that increasing the active layer thickness beyond 300 nm in standard devices leads to a decrease in PCE for all D/A ratios. This trend can be better understood by looking at the effects of the active layer thickness, as well as the shunt and series resistance, on each of the efficiency parameters.

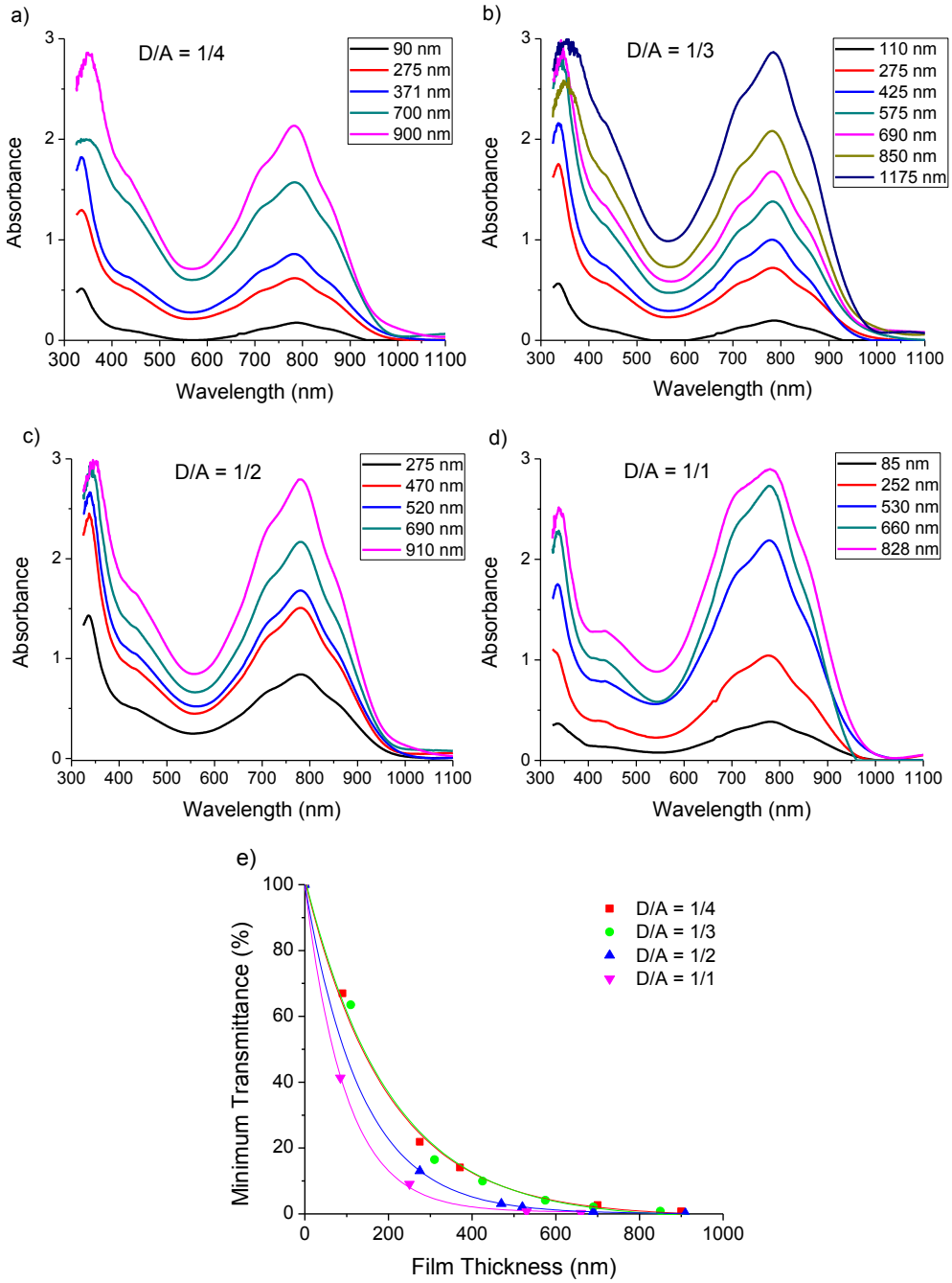


**Figure 25.** UV-Vis absorbance of PDQT:$PC_{61}BM$ films prepared at various active layer thicknesses for D/A ratios of a) 1/4, b) 1/3, c) 1/2 and d) 1/1. e) Minimum transmittance determined from the Beer-Lambert equation for various ratios of PDQT to $PC_{61}BM$ at different film thicknesses. Minimum transmittance was calculated from the maximum absorbance values at 770 nm.

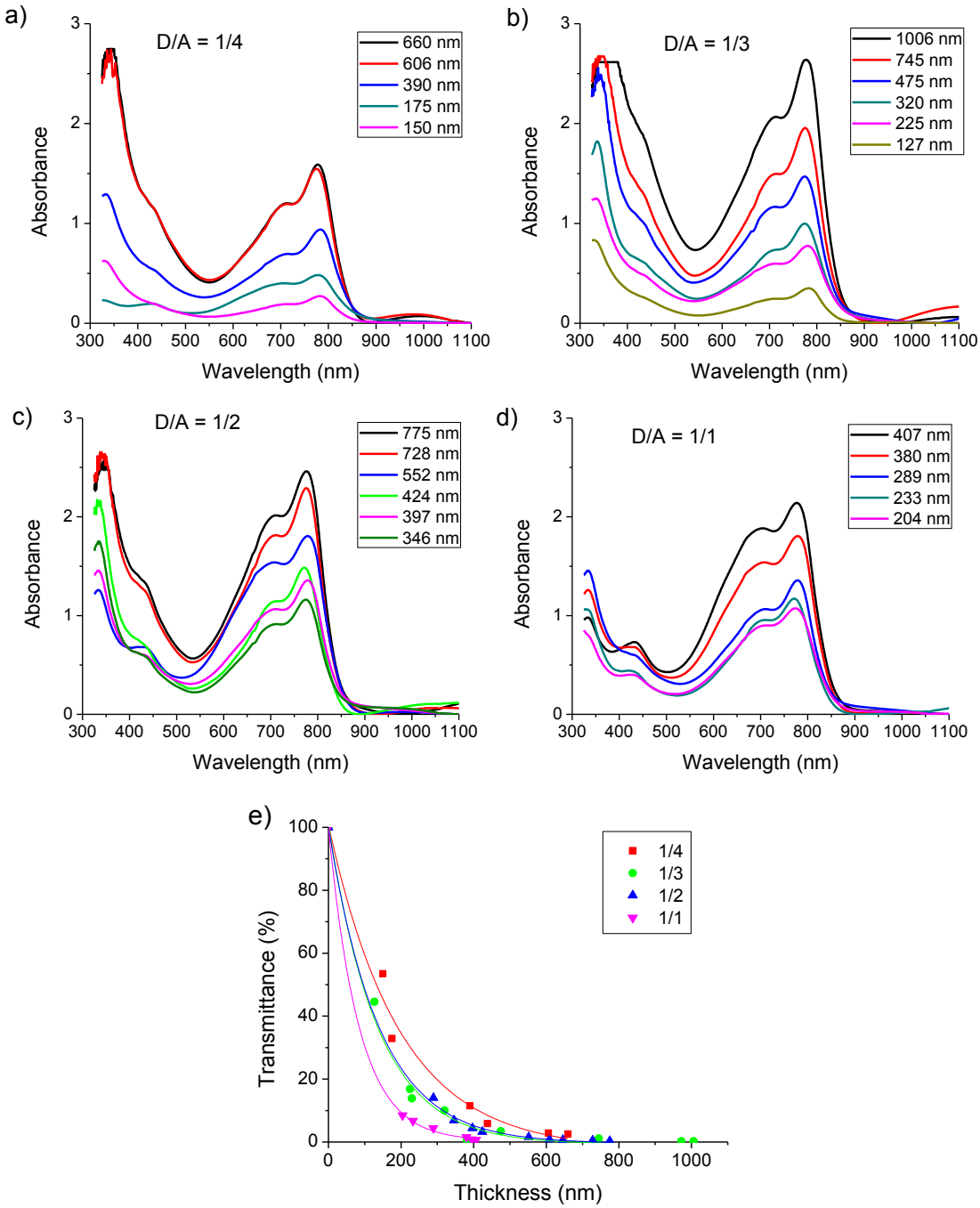


**Figure 26.** UV-Vis absorbance of PDBFBT:$PC_{61}BM$ films prepared at various active layer thicknesses for D/A ratios of a) 1/4, b) 1/3, c) 1/2 and d) 1/1. e) Minimum transmittance determined from the Beer-Lambert equation for various ratios of PDBFBT to $PC_{61}BM$ at different film thicknesses. Minimum transmittance was calculated from the maximum absorbance values at 770 nm.

In all D/A ratios, the maximum *FF* was observed for the device with the thinnest active layer (~100 nm) in the series. *FF*s were found to be quite high when the active layer is thin. Values close to 70% were achieved, which tends to be among the highest values of similar high mobility DPP-based polymer donors [83]. As the active layer thickness increases, *FF* decreases monotonically. The steady decrease in *FF* from the lowest to the highest thickness is reflected in the shunt and series resistances (Figure 28). $R_{shunt}$ in the standard devices was found to decrease with increasing thickness in all ratios up to ~400 nm; it then becomes fairly constant. This suggests that recombination increases with increasing active layer thickness and reaches its maximum at a thickness of ~400 nm. Variations can be observed amongst the different D/A ratios. In comparison with the 1/1 and 1/2 ratios, the 1/3 ratio demonstrates higher $R_{shunt}$ at each thickness, suggesting that this D/A ratio offers a better charge balance. The higher content of $PC_{61}BM$ in the 1/3 ratio blends provides a greater pathway through which the electrons can flow, thereby reducing recombination. However, a further increase in the $PC_{61}BM$ content (D/A = 1/4) causes $R_{shunt}$ to drop to the same level as the devices with D/A = 1/2 or 1/1, probably due to the discontinuity of the donor phase, which hampers hole transport.

$R_{series}$ for each D/A ratio is relatively constant until the thickness reaches ~400 nm. At thicknesses greater than 400 nm, a marked increase in $R_{series}$ is observed. This demonstrates an increase in ohmic losses due to increasing thickness, and suggests that space charge, which leads to bimolecular recombination, is prevalent at greater active layer thicknesses. Variations in $R_{series}$ amongst the different D/A ratios are present, with the 1/3 ratio displaying the lowest $R_{series}$ at each thickness. This is again probably due to a better charge balance attained with the improved pathway (the $PC_{61}BM$ phase) for electron transport.

As predicted from the absorbance data, $J_{SC}$ for all D/A ratios is found to increase with increasing active layer thickness up to ~350-400 nm (Figure 27), due to improved light harvesting. Beyond this thickness, $J_{SC}$ decreases gradually to very low values. For the D/A = 1/1 blends, for example, $J_{SC}$ at 800 nm is only ~1 $mAcm^{-2}$, about 25% of the maximum value of 4 $mAcm^{-2}$ obtained at ~250 nm. This decrease in $J_{SC}$ for devices with thicknesses greater than ~350-400 nm can be attributed to the notable increase in $R_{series}$ (Figure 28), and thus reduced charge collection.

The highest $V_{OC}$ of ~640 -670 mV is very close to the predicted value of 690 mV and was achieved at the lowest thickness of ~100 nm for all D/A ratios. However, $V_{OC}$ decreases very slowly with increasing active layer thickness. The influence of the D/A ratio on $V_{OC}$ seems subtle: the lower ratios (1/4 and 1/3) appear to have only slightly higher $V_{OC}$ values than the higher ratios (1/2 and 1/1).

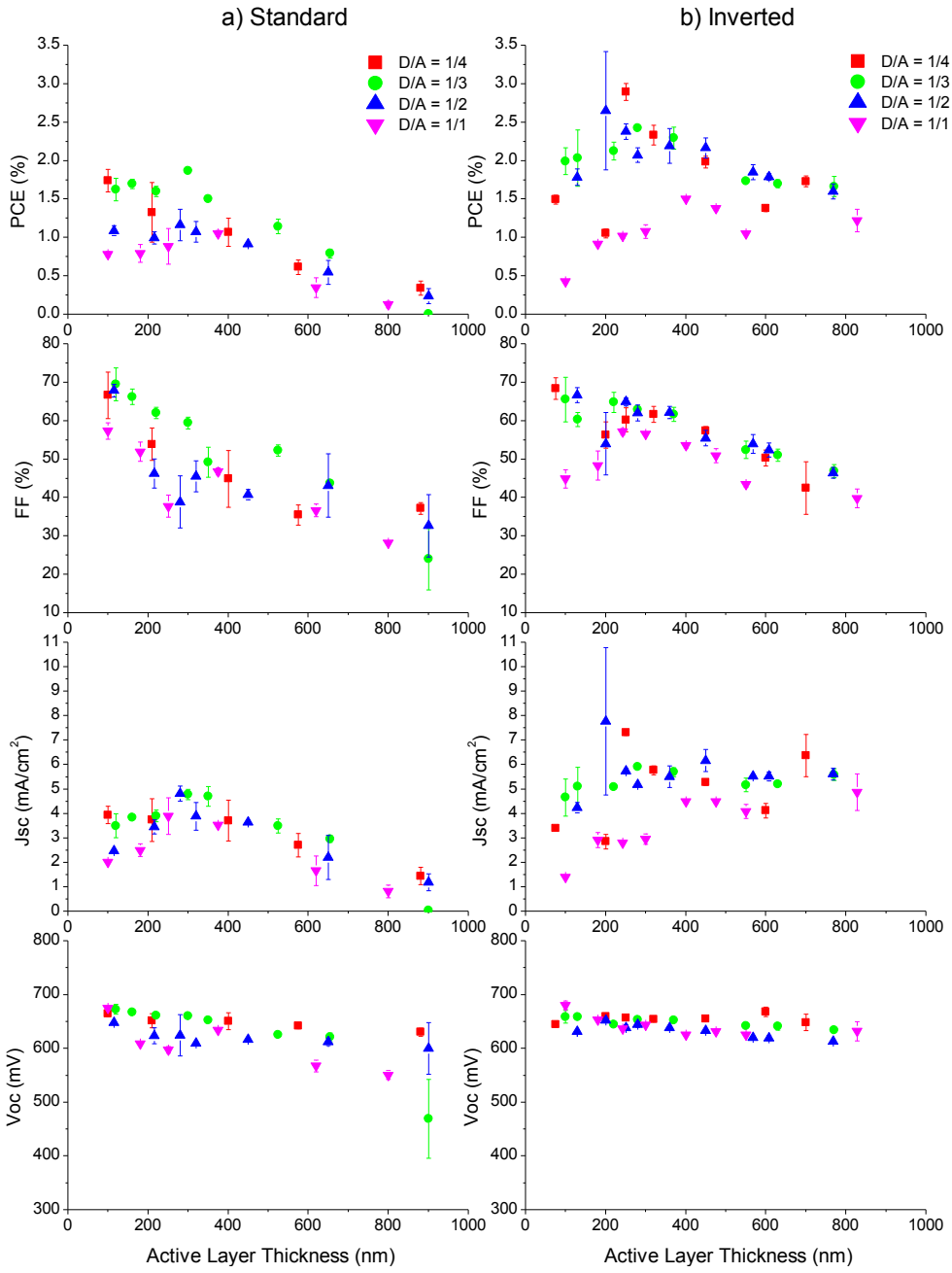


**Figure 27.** Measured power conversion efficiency (PCE), open circuit voltage ($V_{OC}$), fill factor (*FF*) and short-circuit current density ($J_{SC}$) at various active layer thicknesses of **PDQT**:$PC_{61}BM$ OPV devices fabricated in a) standard and b) inverted configurations using various D/A ratios in the active layer.

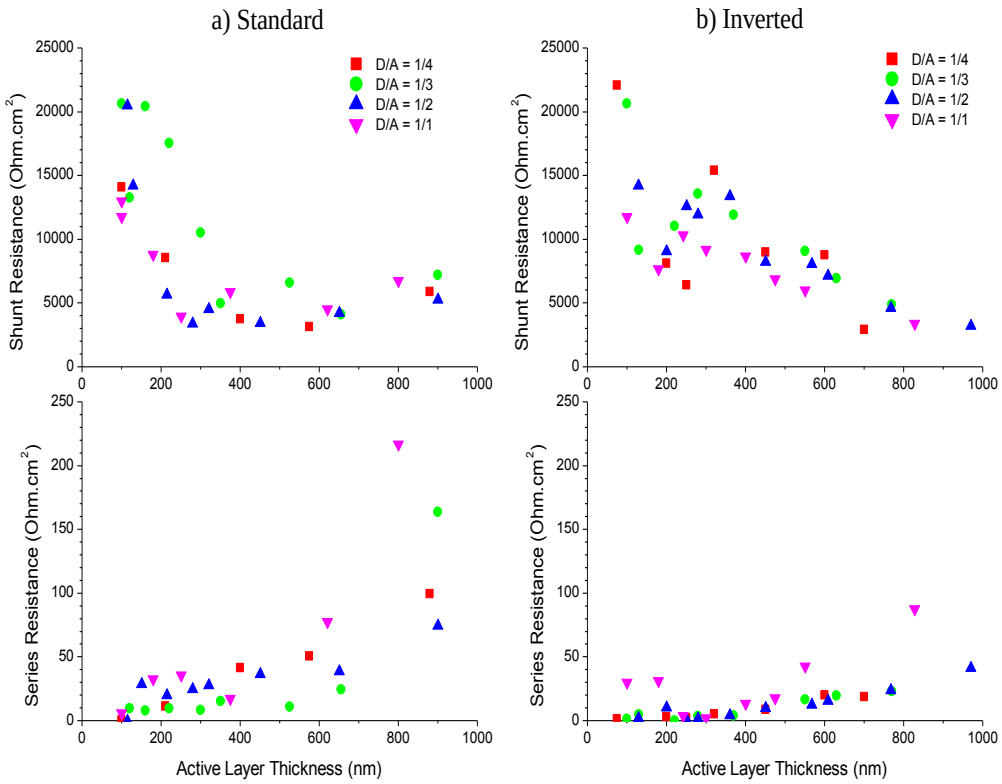


**Figure 28.** Shunt resistance and series resistance at various active layer thicknesses of **PDQT**:$PC_{61}BM$ OPV devices prepared in a) standard and b) inverted configurations using various D/A ratios in the active layer.

The corresponding results obtained using an active layer consisting of PDBFBT:$PC_{61}BM$ are found in Figure 29. The results are very similar to those of PDQT. The PCE of standard devices is found to decrease as the active layer thickness is increased for all ratios tested, and at a thickness of ~ 800 nm, the PCE of all ratios is negligible. The highest PCE (3.14%) was achieved using a D/A ratio of 1/3 and an active layer thickness of 171 nm, which is a markedly higher PCE than found for PDQT with a slightly lower active layer thickness.

Similar to PDQT, *FF* was also found to decrease for all PDBFBT:$PC_{61}BM$ ratios as the active layer thickness was increased. Again, the highest *FF* in each D/A ratio was observed for the device with the thinnest active layer (~100 nm). High *FF* values of ~70% were achieved, which is comparable to the results of PDQT. Although there are fewer data points than that of PDQT, the *FF* trend for PDBFBT also appears to be monotonic and is reflected in the shunt and series resistances (Figure 30). $R_{shunt}$ in the standard devices was found to decrease with increasing thickness in all ratios up to ~600

nm before stabilizing. This thickness is slightly higher than that of PDQT (~400 nm), suggesting maximum recombination occurs at a greater thickness in PDBFBT devices. $R_{series}$ is similar to PDQT in that the values increase until a thickness of ~600 nm and, although the data points are limited, it would appear that there may be a large increase in $R_{series}$ at thicknesses beyond 800 nm.

The $J_{SC}$ results of the PDBFBT standard devices tend to be more oscillatory than the PDQT results. High values are maintained until a thickness of ~600-700 nm, at which point $J_{SC}$ drops in all ratios tested. This decrease in $J_{SC}$ for devices with thicknesses greater than ~600-700 nm is likely attributable to a large increase in $R_{series}$ at the same thickness, however at thicknesses of ~300 nm, $R_{series}$ values are rather high (> 10 $\Omega \cdot cm^2$) and would be expected to impact $J_{SC}$ at this level. Indeed the $J_{SC}$ values do decline at ~300 nm in the 1/2 and 1/4 ratios, demonstrating the opposition between absorbance and recombination.

For each ratio, the highest $V_{OC}$ of ~720 -730 mV is slightly lower than the predicted value of 770 mV (Chapter 3). These values were achieved at the lowest film thickness (~150-200 nm) for all D/A ratios. The $V_{OC}$ is quite consistent amongst the various ratios. A very slight decrease in $V_{OC}$ is observed as the active layer thickness increases to ~800 nm, at which point it declines significantly in the 1/3 and 1/4 ratios.

The optimal thickness of an OPV active layer is determined by the balance achieved between light harvesting and recombination. Based on the above results, it seems that to achieve consistently good photovoltaic performance in standard OPV devices, the thickness of the PDQT:$PC_{61}BM$ active layer needs to be kept between 100 nm and 400 nm. For the PDBFBT:$PC_{61}BM$ standard devices, on the other hand, the optimal range is between 100 nm and 350 nm, which is slightly lower than that of PDQT. In both cases, however the optimal thickness range provides a much greater window of tolerable thickness, and the capability of employing active layers that are thicker than what is commonly allowed (~100 nm).

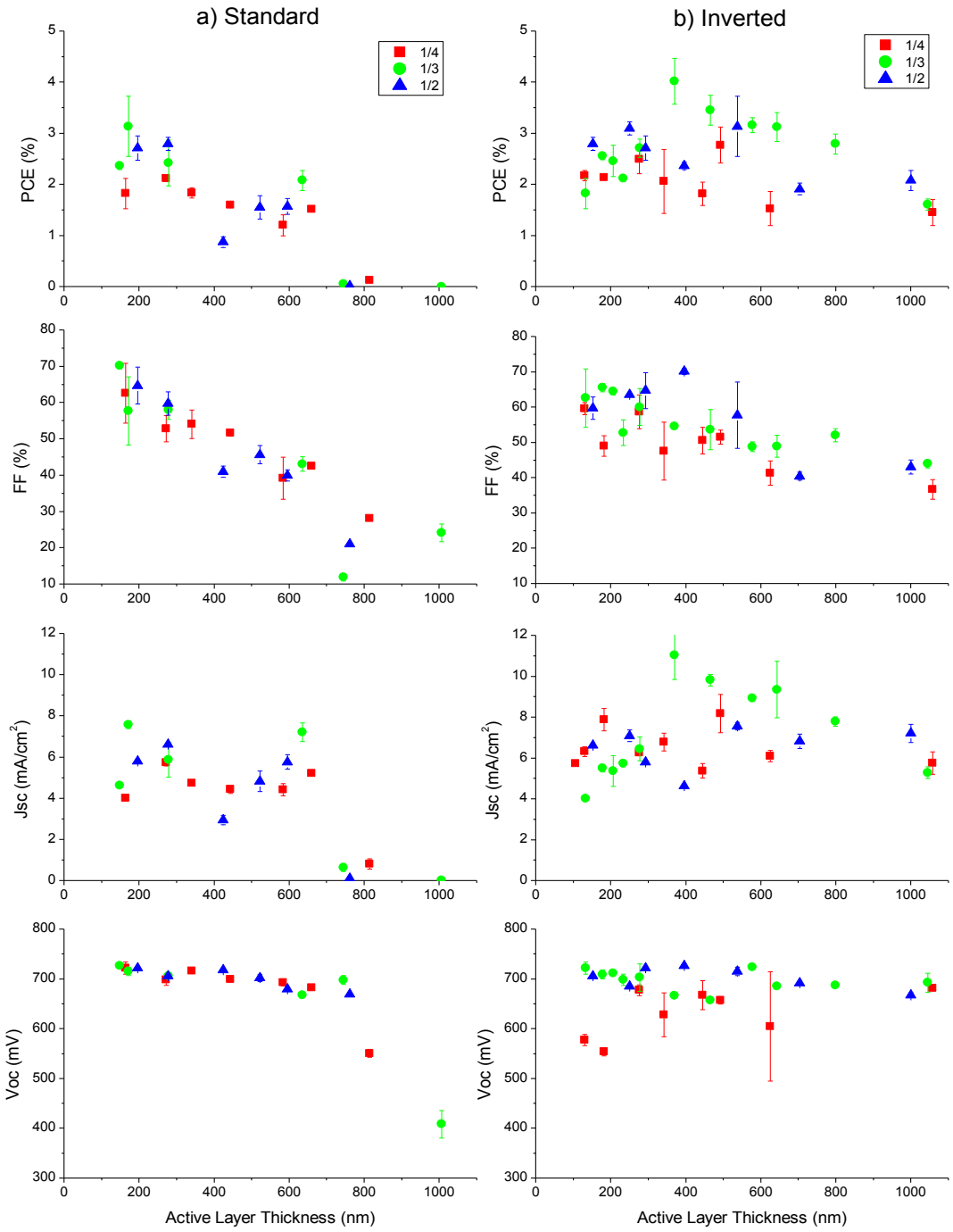


**Figure 29.** Measured power conversion efficiency (PCE), open circuit voltage ($V_{OC}$), fill factor (*FF*) and short-circuit current density ($J_{SC}$) at various active layer thicknesses of **PDBFBT**:$PC_{61}BM$ OPV devices fabricated in a) standard and b) inverted configurations using various D/A ratios in the active layer.

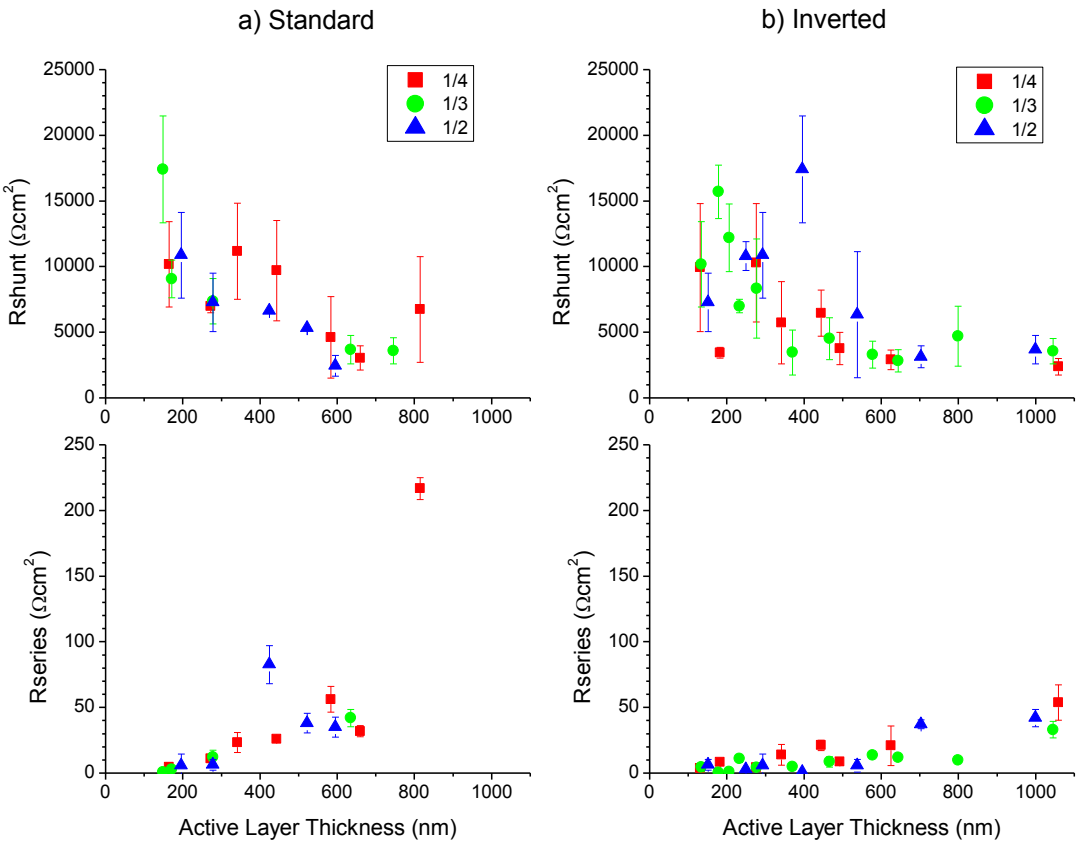


**Figure 30.** Shunt resistance and series resistance at various active layer thicknesses of **PDBFBT**:$PC_{61}BM$ OPV devices prepared in a) standard and b) inverted configurations using various D/A ratios in the active layer.

Inverted OPV devices have previously been found to afford high efficiencies at high active layer thicknesses [23,155]. Both PDQT and PDBFBT were therefore also tested in the inverted OPV device configuration. Figure 27 shows the PCE and related parameters (*FF*, $J_{SC}$, and $V_{OC}$) for the inverted devices prepared using the various PDQT:$PC_{61}BM$ ratio blends. The *FF* of devices with D/A = 1/1 increases with increasing active layer thickness and reaches its maximum value of ~55% at ~250 nm. Increasing the active layer thickness causes a gradual decrease in *FF*. For devices with lower D/A ratios (1/2, 1/3, and 1/4), the *FF* is at its highest value (65-68%) at the lowest thickness and then decreases steadily as the active layer thickness increases from ~100 nm to ~800 nm. When the active layer is thicker than ~200 nm, the *FF* values of the inverted devices are generally much higher than those of the standard devices. In sharp contrast, the decline in $R_{shunt}$ occurs much more gradually in the inverted devices. $R_{shunt}$ values of PDQT:$PC_{61}BM$ inverted devices remain above

~5000 $\Omega \cdot cm^2$ until the thickness reaches ~700 nm (Figure 28). This suggests that recombination is suppressed more effectively in the inverted devices than in the standard devices.

For the inverted devices with D/A ratios of 1/2, 1/3, and 1/4, $R_{series}$ values remain at a low level of < 10 $\Omega \cdot cm^2$ until the thickness reaches ~400 nm. At thicknesses greater than 400 nm, $R_{series}$ values increase, but at a much slower pace compared with the standard devices. Devices with a D/A ratio of 1/1 showed higher $R_{series}$ values than did devices with lower D/A ratios. For inverted devices with various D/A ratios, the trend of $R_{series}$ versus thickness agrees with the trend of *FF*.

The difference between standard and inverted device performance in PDQT:$PC_{61}BM$ films is most remarkable when comparing their $J_{SC}$ values (Figure 27). In the active layer thickness range of ~100-300 nm, the $J_{SC}$ of inverted devices increases when the thickness increases from ~100 nm to ~300 nm, a similar trend to the one observed for the standard devices. However, the $J_{SC}$ values remain almost constant up to a thickness of ~800 nm, which is strikingly different from the standard devices, in which the $J_{SC}$ decreases significantly at thicknesses beyond ~300 nm. These observations again demonstrate the reduction in recombination within the inverted device architecture at higher active layer thicknesses.

At lower thicknesses of ~100 nm, the $V_{OC}$ values of inverted devices are similar to those of standard devices. However, the $V_{OC}$ of inverted devices remains almost at a constant value of ~650 mV throughout the various thicknesses (~100-800 nm) and various D/A ratios, probably due to reduced ohmic losses (lower $R_{series}$ values).

In general, the inverted OPV devices showed much higher efficiencies than the standard devices (Figure 27). For inverted devices with D/A ratios of 1/4, 1/3, and 1/2, the maximum average PCEs of 2.4-2.9% were achieved at active layer thicknesses of ~200-300 nm. While the PCE for the 1/4 ratio devices drops sharply when the active layer thickness deviates from 300 nm, the PCE for devices with D/A = 1/3 or 1/2 remains quite consistent at 1.5-2.5 % throughout the thickness range tested (~100 - 800 nm). Although devices with a D/A ratio of 1/1 displayed lower efficiencies (~1-1.5%), their performance also shows little dependence on thickness, consistent with devices possessing other D/A ratios.

Figure 29 shows the PCE and related parameters (*FF*, $J_{SC}$, and $V_{OC}$) for the inverted devices prepared using the various PDBFBT:$PC_{61}BM$ ratio blends. The *FF* of devices with D/A = 1/2 increases with increasing active layer thickness and reaches its maximum value of ~70% at ~400 nm. Increasing the

active layer thickness further causes a prompt decrease in *FF*. For devices with lower D/A ratios (1/3 and 1/4), the *FF* decreases consistently as the active layer thickness increases from ~150-1000 nm. The *FF* values of the inverted devices are similar to those of the standard devices until a thickness of ~600 nm, at which point the *FF* of standard devices continues to decline but the FF of inverted devices remains at a fairly consistent value of ~40%. Similar to PDQT, the decline in $R_{shunt}$ occurs more gradually in the inverted devices than the standard devices (Figure 30) suggesting improved suppression of recombination in the inverted devices.

For the inverted devices with D/A ratios of 1/2, $R_{series}$ values remain consistently low (< 10 $\Omega \cdot cm^2$) until a thickness of ~550-600 nm (Figure 30). $R_{series}$ values of the D/A = 1/3 devices remain fairly low until a much higher thickness of 800 nm. In the D/A = 1/4 ratio, $R_{series}$ is slightly higher than the 1/2 and 1/3 ratios but also remains consistent until a thickness of ~600 nm. In all D/A ratios of inverted devices the active layers are quite thick (~1000 nm) before $R_{series}$ values are comparable to the 600 nm standard devices. Similar to PDQT inverted devices, the trend of $R_{series}$ versus thickness agrees with the trend of *FF*.

Analysis of the $J_{SC}$ values of PDBFBT:$PC_{61}BM$ OPV devices (Figure 29) shows that with D/A ratios of 1/3 and 1/4, the inverted devices have much higher values than the standard devices. The 1/2 ratio, however demonstrates very similar $J_{SC}$ values in both device configurations. Similar to the standard devices, the $J_{SC}$ is found to oscillate throughout the different active layer thicknesses. In inverted devices, this is most prevalent in the 1/2 and 1/4 ratios since there is less variability amongst the $J_{SC}$ values. In the 1/3 ratio, there is a much greater difference between the highest and lowest $J_{SC}$ values, with the lowest value being ~30% of the highest. This oscillatory behaviour of $J_{SC}$, although not as apparent in PDQT devices, has previously been observed and attributed to optical interference [30,152,156–158]. Such an effect is likely to occur as a result of different refractive indices in the layers of multilayer structures or the presence of reflective back electrodes. Overall, the main difference in $J_{SC}$ between the standard and inverted devices occurs at an active layer thickness of ~700-800 nm. The $J_{SC}$ of standard devices drops suddenly at this thickness, whereas the $J_{SC}$ of inverted devices remains fairly consistent with that of thinner layers. Again the inverted device architecture demonstrates reduced recombination at higher active layer thicknesses.

The $V_{OC}$ values of inverted devices with D/A ratios of 1/2 and 1/3 are similar to those of standard devices, however devices with D/A = 1/4 tend to be less consistent and show lower $V_{OC}$ values

overall. The $V_{OC}$ of inverted devices does not decrease at thicknesses greater than 800 nm as in the standard devices.

As with PDQT, the inverted OPV devices with PDBFBT:$PC_{61}BM$ active layers showed much higher efficiencies than the standard devices (Figure 29). The highest PCE (4.0%) was achieved using a D/A ratio of 1/3 with an active layer thickness of 370 nm, which is much higher than the highest PCE achieved in PDQT:$PC_{61}BM$ devices of 2.9% (D/A = 1/4, 250 nm). For inverted devices with D/A ratios of 1/4 and 1/2, the maximum PCEs (2.8% and 3.1%, respectively) were achieved at active layer thicknesses of ~500-550 nm, although these PCEs were not much higher than those achieved at ~250-275 nm. While the PCE of standard devices drops sharply to negligible values at thicknesses of ~700-800 nm in all ratios, the PCE of inverted devices remains greater than 1.4% in all ratios, even when the active layer thickness is greater than 1 µm.

The markedly different photovoltaic performances of standard versus inverted devices is attributed to the much higher $\mu_h$ of the donor material versus the $\mu_e$ of the acceptor material used in this study, which makes the inverted architecture more favourable from a charge collection standpoint. The proposed mechanism is illustrated in Figure 31, which is in agreement with arguments presented in the literature [159–161].

Since illumination occurs through the bottom ITO electrode in both cell architectures, the majority (~90%) of excitons are generated within the first ~200-450 nm of the active layer adjacent to the ITO, as predicted by the UV-Vis data. The photogenerated holes and electrons will travel towards the anode and cathode, where they are respectively collected. In a standard device, the electrons travel towards the top cathode through the $PC_{61}BM$ domains, whereas the holes move towards the bottom ITO anode through the donor polymer domains. Since charges are created closer to the ITO electrode, the majority of electrons have to travel a longer distance to reach the electron-collecting LiF/Al cathode, whereas the hole collection distance to the PEDOT:PSS/ITO anode is much shorter. Combined with the fact that the $\mu_e$ of $PC_{61}BM$ is much lower than the $\mu_h$ of both PDQT and PDBFBT, the standard device configuration inherently leads to much poorer electron collection capacity in comparison to that of holes. As the active layer thickness increases, the electron collection distance increases, which further aggravates the situation. As such, increasing the active layer thickness leads to charge accumulation and recombination in the active layer, resulting in a decrease in both *FF* and $J_{SC}$. On the other hand, in inverted devices, the conduction paths for electrons and holes are reversed, with holes now traveling a longer distance. As a result, the *FF* and

$J_{SC}$ of inverted devices remain relatively unchanged over a wide thickness range since the $\mu_h$ of both donor materials is much higher.

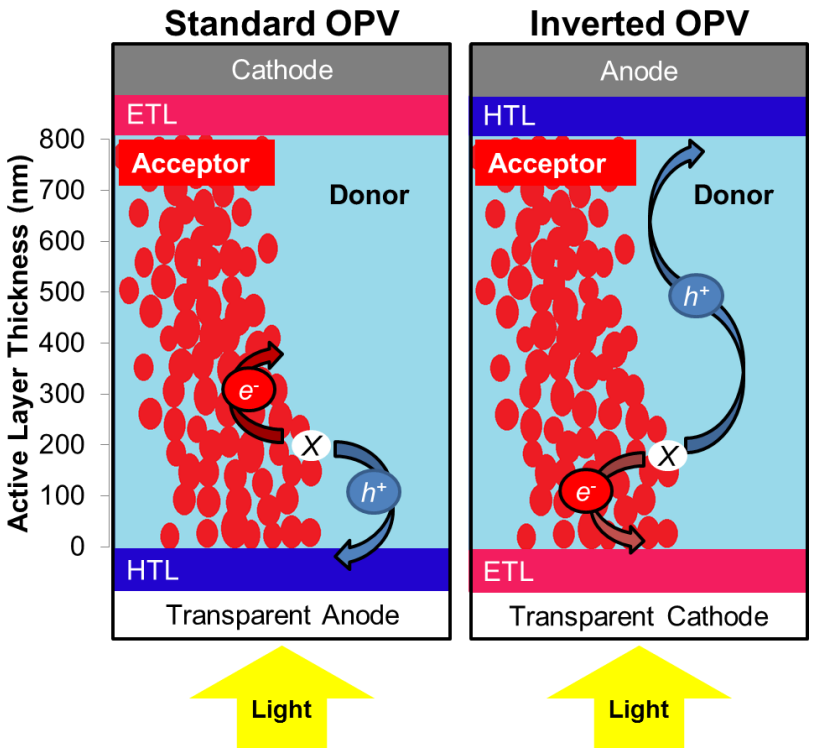


**Figure 31.** A schematic description of hole and electron transport in standard and inverted OPV devices. The majority of excitons (X) are created in the first ~250-400 nm of the active layer closest to the light source. In the standard device configuration, the thickness is limited by the distance that the electrons ($e^-$) are able to move. In the inverted device configuration the thickness is limited by the distance that the holes ($h^+$) are able to move. A donor with high $\mu_h$ is therefore favoured for the inverted structure.

In order to verify that hole conduction in the PDQT:$PC_{61}BM$ mixture is much higher than electron conduction, hole-only and electron-only devices (Figure 32a & b, respectively) were utilized that were designed and fabricated following previously published methodology [105,162–164]. The current density-voltage (*J-V*) characteristics were measured in the dark to study changes in hole and electron conduction in these devices, respectively, as the thickness varies. A D/A ratio of 1/3 was chosen due to the high performance of both standard and inverted devices at this ratio. For these measurements, a positive bias, defined as the ITO being at a more positive potential relative to the

metal electrode, was used. Under such as a bias, holes flow across the PDQT:$PC_{61}BM$ layer and are collected by the $MoO_3$/Ag electrode in the hole-only devices, whereas electrons flow across the PDQT:$PC_{61}BM$ layer and are collected by the ZnO/ITO electrode in the electron-only devices. Therefore the flow direction of holes or electrons from the active layer to the contact in these test devices is the same as in the inverted OPV devices. Figure 32a & b show the *J-V* characteristics obtained from a series of these devices with various PDQT:$PC_{61}BM$ layer thicknesses. As expected, increasing the thickness leads to an increase in overall resistance of all devices, reflected in the lower *J* for any given *V*. However, the changes are much greater in the case of the electron-only devices. For example, in the hole-only devices, increasing the thickness of the active layer by a factor of five (i.e. from 108 nm to 550 nm) generally leads to a decrease in current by approximately one order of magnitude, whereas a similar increase in thickness (i.e. from 120 nm to 630 nm) in the electron-only devices, leads to a decrease in current by more than two orders of magnitude. This clearly shows that hole transport is much easier in the PDQT:$PC_{61}BM$ blend layers, verifying the previous argument that the good performance of the D/A mixture in inverted devices is due to the higher hole transport.

Figure 32c displays the conductance per unit area (=J/V) at 2 volts for the above hole-only and electron-only devices. Although conductance decreases with increasing thickness in both devices, as expected, the electron-only devices demonstrate reduced overall conductance in comparison to hole-only devices. Conductance in both device types begins to decrease at a thickness of ~200-300 nm and appears to be somewhat balanced at ~300 nm. Moreover, at ~400 nm, the conductance of electron-only devices is negligible, whereas hole-only devices continue to demonstrate conductance at a thickness as high as 550 nm. This correlates well with the fact that $J_{sc}$ does not increase beyond a thickness of 300 nm in either standard or inverted devices but $J_{sc}$ in inverted devices can be maintained beyond 300 nm due the conduction of holes at greater thicknesses.

Hole and electron mobilities are often calculated from the *J-V* characteristics of such devices using the space charge limited current (SCLC) method [89,103,106,162]. Analysis of a log*J*–log*V* plot reveals a quadratic region that corresponds to the accumulation of space charge and is therefore considered trap-free. In this region, charge mobility is measured according to the Mott-Gurney equation (Equation 6) [104,108,162]. The hole and electron mobility values for the hole-only and electron-only devices with varied active layer thicknesses at a D/A ratio of 1/3 were calculated and plotted in Figure 32d. The hole and electron mobilities are comparable at a low active layer thickness: $1.2 \times 10^{-3}$ $cm^2V^{-1}s^{-1}$ for the hole-only devices with an active layer thickness of 140 nm and

$1.35 \times 10^{-3}$ $cm^2V^{-1}s^{-1}$ for the electron-only devices with an active layer thickness of 120 nm. $\mu_e$ falls in the range of 0.6 - $5.3 \times 10^{-3}$ $cm^2V^{-1}s^{-1}$ in the thickness range of 120 nm to 630 nm. However, $\mu_h$ is strongly dependent on the active layer thickness. As the thickness increases from 140 nm to 550 nm, $\mu_h$ increases dramatically from $1.2 \times 10^{-3}$ to $2.0 \times 10^{-2}$ $cm^2V^{-1}s^{-1}$. Apparently, hole transport is much more efficient than electron transport in the PDQT:$PC_{61}BM$ blend layers, particularly as the active layer gets thicker.

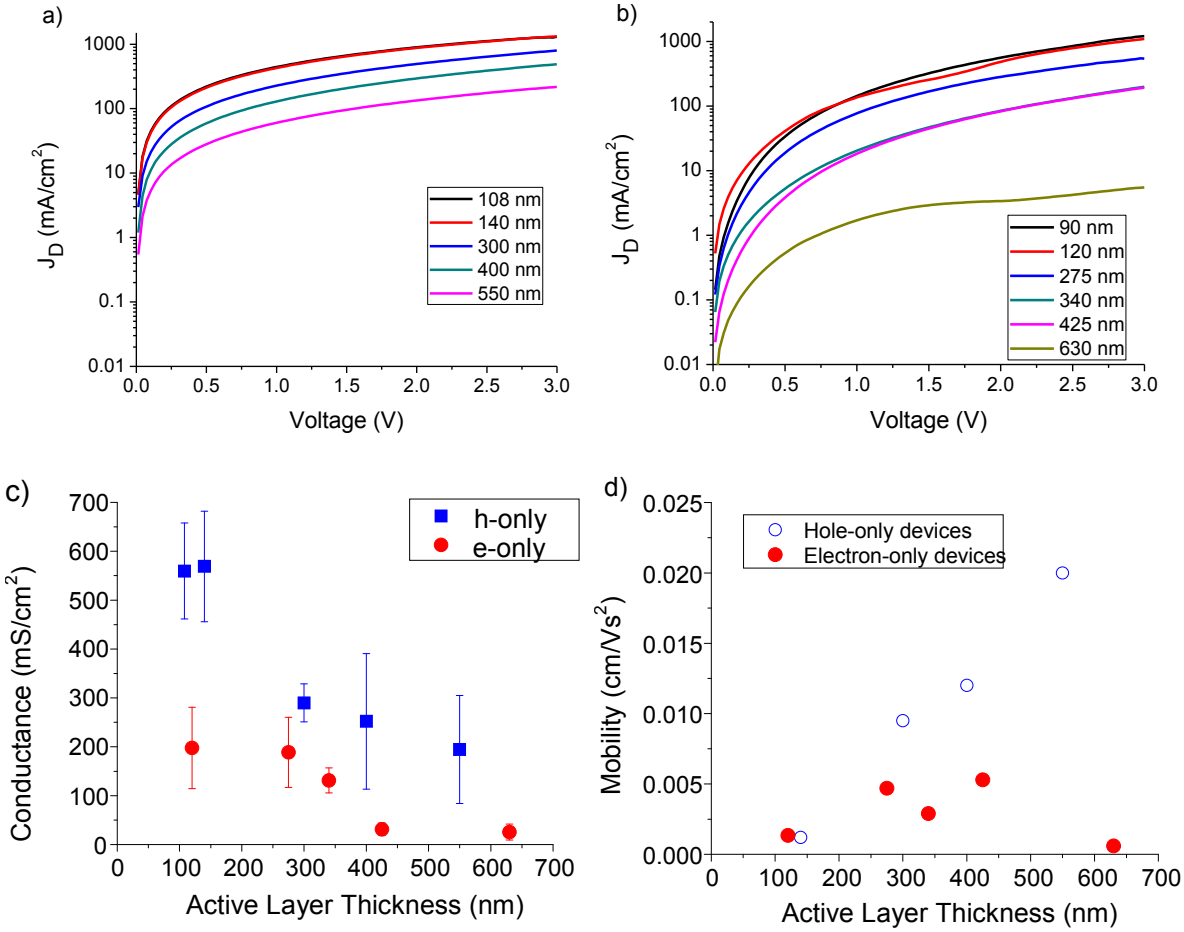


**Figure 32.** Dark current densities of the PDQT:$PC_{61}BM$ blends (D/A =1/3) in (a) hole-only and (b) electron-only devices at various active layer thicknesses (Device area = 0.125 $cm^2$). c) Calculated mobilities of hole-only and electron-only devices at various active layer thicknesses, d) Calculated conductance per device area ($V$ = 2V) of hole-only and electron-only devices at various active layer thicknesses.

Alstrup *et al*. also implemented the inverted OPV configuration to demonstrate that the PCE of P3HT:PCBM devices is maintained with increasing active layer thickness (up to 800 nm) [153]. All

efficiency parameters increased significantly from 0 - 150 nm, the region in which carrier generation and transport occur. In thicknesses beyond 300 nm, where mainly hole transport occurs, current continued to increase due to increasing absorption, whereas $V_{OC}$ remained steady and *FF* decreased at approximately the same rate as the increase in current. Zeng *et al*., on the other hand, reported that the PCE of standard OPV devices having as-cast P3HT:PCBM active layers decreases as the thickness increases beyond 130 nm [154]. Interestingly, after the devices were thermally annealed, the highest PCE was obtained at a high thickness of 830 nm. It was also observed that the PCE was quite consistent (2.3-3.1%) over a wide range of thicknesses, from 370 nm to 1200 nm. This was explained by thermally induced vertical phase separation of the donor and acceptor phases, in which PCBM is concentrated next to the top surface, facilitating electron transport. As well, thermal diffusion of $Li^+$ ions to the active layer is believed to be beneficial in thick layers through the formation of $Li^+PCBM^-$ complexes.

In principle, the different photovoltaic performances between standard and inverted devices may also arise from vertical phase separation effects, which can lead to different charge collection capacities in the two device configurations [165–168]. For example, it has been suggested that in some cases the concentration of $PC_{61}BM$ is higher in the lower part of the active layer. If this is the case, the higher concentration of the acceptor at the bottom of the active layer would facilitate the electron transport towards the bottom cathode (ZnO/ITO), resulting in improved performance of inverted cells. The vertical gradient distribution of PDQT and $PC_{61}BM$ would be influenced by properties of the substrate surface and the active layer thickness. Variations in the gradient distribution would result in changes to the surface morphology of the active layer on different substrate surfaces and at varied active layer thicknesses. In standard devices, the active layer was spin-coated onto the PEDOT:PSS layer on the ITO-coated glass, whereas in the inverted devices, the active layer was spin-coated onto the ZnO-covered ITO-coated glass. AFM images of the active layer films with a D/A ratio of 1/3 on these two types of substrate surfaces are shown in Figure 33. There are almost no differences in morphology among the films with similar thicknesses. The images obtained for the films on the same substrate with three drastically different thicknesses also showed very similar surface morphologies, suggesting that there is no obvious vertical gradient distribution of PDQT and $PC_{61}BM$ in either device configuration. These results therefore suggest that the dramatically different photovoltaic performances observed for standard and inverted devices are unlikely caused by the vertical or lateral phase separation of their active layers.

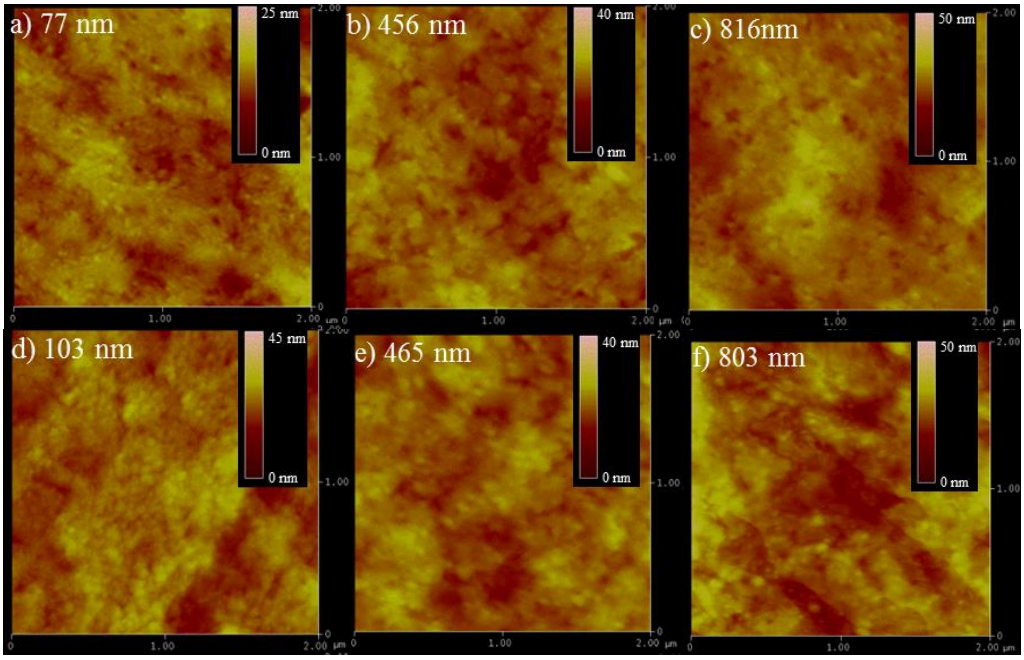


**Figure 33.** AFM images (2 µm × 2 µm) of PDQT:$PC_{61}BM$ (1/3) films spin coated on ITO/PEDOT:PSS (a, b, and c) and ITO/ZnO substrates (d, e, and f) at different active layer thicknesses.

It has previously been suggested that the inverted configuration holds the promise of thicker active layers when produced with donor materials that have high $\mu_h$ values [159–161]. In standard devices, no material reported in the literature other than P3HT has been able to maintain high PCE beyond the 100-200 nm range. With inverted devices, Peet *et al*. found that high PCE could be maintained up to a thickness of 400 nm using a polymer (4,4'-bis(alkyl)dithieno[3,2-b:2',3'-d]silole) and 2,5-bis(thiophen-2-yl)thiazole[5,4-d]thiazole copolymer) with relatively high $\mu_h$ ($10^{-2}$ $cm^2V^{-1}s^{-1}$) [155] in combination with $PC_{61}BM$, which has similar $\mu_e$ ($2.4 \times 10^{-2}$ $cm^2V^{-1}s^{-1}$ [94]). Here it is shown that the use of a higher mobility donor material allows the PCE of inverted devices to be maintained over a much wider active layer thickness range. In this case of PDQT, a PCE that is 70% of its peak value was achieved at a thickness as high as 770 nm. In contrast, the PCE of standard OPVs at this thickness is only ~20% of its peak value. Similar results are present in the thickness analysis of PDBFBT. Active layers with a thickness as high as ~800 nm and a very wide tolerable thickness range (~100-800 nm) are well suited for conventional printing techniques, such as screening printing, that can be used for low cost, high throughput processing [122]. Furthermore, in the case of PDQT, D/A ratios of 1/4, 1/3 and 1/2 gave very similar performance even though the charge carrier mobility

of PDQT is almost 40 times greater than that of $PC_{61}BM$. This suggests that PCE is not very sensitive to the D/A ratio when a high mobility donor material, such as PDQT, is used in an inverted configuration, thus providing even wider latitude for easier and much more feasible large scale production of OPVs.

## 5.3 Conclusions

High *FF*s (~70%) have been achieved through the use of high $\mu_h$ polymers, PDQT and PDBFBT. The high $\mu_h$ of these polymers also allows the fabrication of OPVs with thicker active layers (~100 nm to ~800 nm) without undermining the photovoltaic parameters, especially in inverted configurations. A comparison between standard and inverted devices demonstrates that the inverted configuration is more suitable for achieving thicker active layers when using a high hole mobility donor. This was attributed to the high $\mu_h$ of the donor phase that helps achieve a longer hole collection path in the inverted configuration.

Additionally, the results of this study demonstrate that the thickness dependence of PCE is governed by the charge collection distance of the carrier going towards the electrode farthest from the light source. For inverted devices the mobility of the donor is more critical, whereas balancing the hole and electron mobilities is less important. This suggests that the mobility of the acceptor may be more relevant in standard devices and that acceptors with high electron mobility (~1 $cm^2V^{-1}s^{-1}$) may lead to thicker active layers in the standard device configuration. These results show that high mobility in the donor and/or acceptor materials, as well as a suitable device configuration, are key factors for achieving high performance OPV devices with thick active layers.

# Chapter 6.

# $PC_{71}BM$ for Increased Absorption

## 6.1 Introduction and Purpose

Fullerene derivatives, $PC_{61}BM$ and $PC_{71}BM$, are two of the most commonly reported acceptors used in solution-processable OPVs. Amongst the various organic acceptors, these fullerene derivatives stand out due to their comparatively high electron mobilities. Typically reported $\mu_e$ values of $PC_{71}BM$ tend to be lower than those of $PC_{61}BM$ [169–172]. Differences in the properties of these two molecules are attributed to differences in their structural symmetry [173,174]. $PC_{71}BM$ has become more prominent in the literature since an interest in low band gap donor polymers has arisen. Replacing $PC_{61}BM$ with $PC_{71}BM$ has been reported to improve PCE in OPV devices using various polymer donors [43,131,173,175–177]. $PC_{71}BM$ leads to an increase in $J_{SC}$ by extending the photocurrent spectrum, thus allowing greater absorption. The absorption of $PC_{61}BM$ is limited to wavelengths below 400 nm, whereas $PC_{71}BM$ has a broader and higher absorption spectrum that extends up to ~600 nm [43]. The absorption spectrum of $PC_{71}BM$ is complementary to the absorption minimum of many low band gap polymers, such as PDQT and PDBFBT. $PC_{61}BM$ was therefore replaced with $PC_{71}BM$ in standard and inverted OPV devices prepared with either PDQT or PDBFBT in order to determine if higher efficiencies could be achieved.

## 6.2 Results and Discussion

### 6.2.1 PDQT

The LUMO-LUMO offset between PDQT and $PC_{71}BM$ was measured by cyclic voltammetry (Figure 34) and was determined to be approximately 0.35 *e*V, which is slightly higher than the offset between PDQT and $PC_{61}BM$. The $E_{LUMO}$ of $PC_{71}BM$ was therefore determined to be -4.35 *e*V and $\Delta E_{LUMO}$ for PDBFBT:$PC_{71}BM$ was estimated to be approximately 0.44 *e*V. Using the HOMO levels of PDBFBT and PDQT calculated earlier (-5.37 and -5.29 *e*V, respectively), $V_{OC}$ values were predicted utilizing Equation 3. The $V_{OC}$ value of PDQT:$PC_{71}BM$ devices was predicted to be 640 mV, while the $V_{OC}$ value of PDBFBT:$PC_{71}BM$ devices was predicted to be 720 mV, both of which are somewhat lower than the corresponding devices with $PC_{61}BM$.

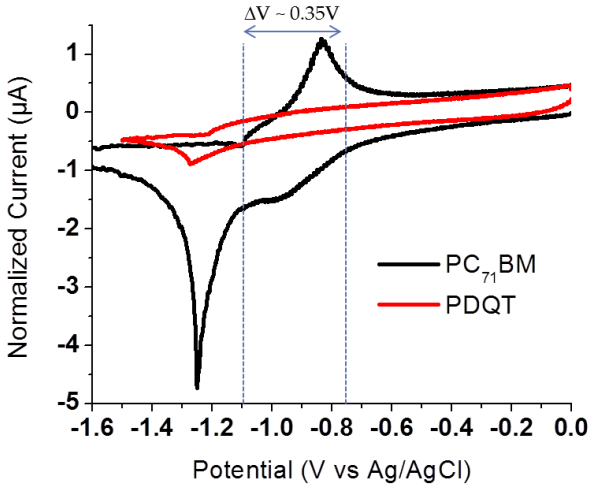


**Figure 34.** Cyclic voltammograms of PDQT and $PC_{71}BM$ films showing the LUMO-LUMO offset.

Figure 35 shows the UV-Vis absorption spectra of PDQT:$PC_{71}BM$ in comparison to the PDQT:$PC_{61}BM$ spectra of two different D/A ratios. The replacement of $PC_{61}BM$ with $PC_{71}BM$ clearly leads to greater absorbance in the 400-650 nm range. This difference in absorbance is particularly prevalent in the films with a higher acceptor content (D/A = 1/3).

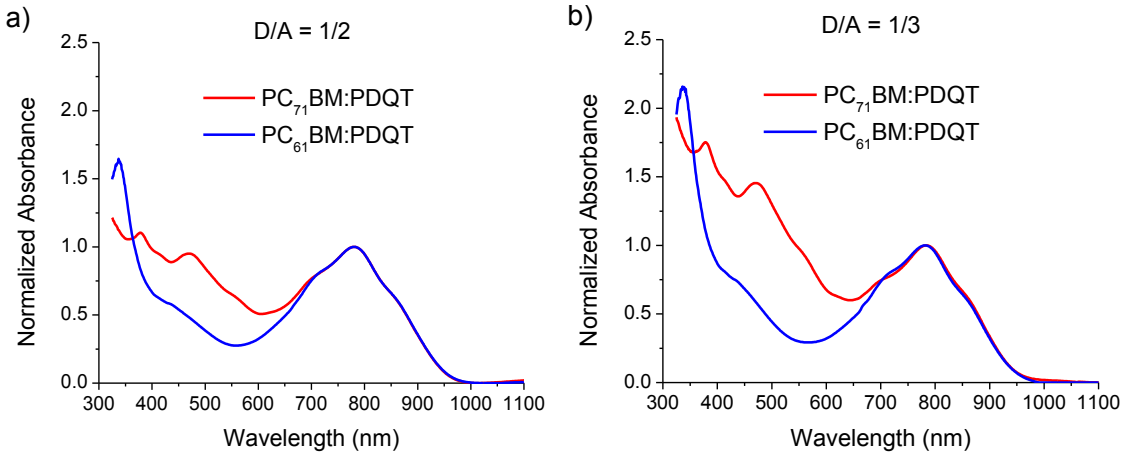


**Figure 35.** UV-Vis absorbance of PDQT:$PC_{71}BM$ compared to PDQT:$PC_{61}BM$ in D/A ratios of a) 1/2 and b) 1/3. Absorbance is normalized for the PDQT peak.

To study the absorption characteristics of the PDQT:$PC_{71}BM$ active layer, films with D/A = 1/2 (Figure 36a) and D/A = 1/3 (Figure 36b) with various thicknesses were prepared and analyzed by UV-Vis absorption measurements. Transmittance values at 770 nm, where the maximum absorption

of PDQT is located, are plotted against active layer thickness (Figure 36c). Similar to the PDQT:$PC_{61}BM$ blends, the vast majority of exciton generation (~90%) is expected to occur within the first 350 nm of the PDQT:$PC_{71}BM$ active layer with D/A = 1/2, and 450 nm for the D/A ratio of 1/3. However, considering the greater absorption of $PC_{71}BM$, a higher $J_{SC}$ in PDQT:$PC_{71}BM$ blends is expected compared to PDQT:$PC_{61}BM$ blends for any given active layer thickness.

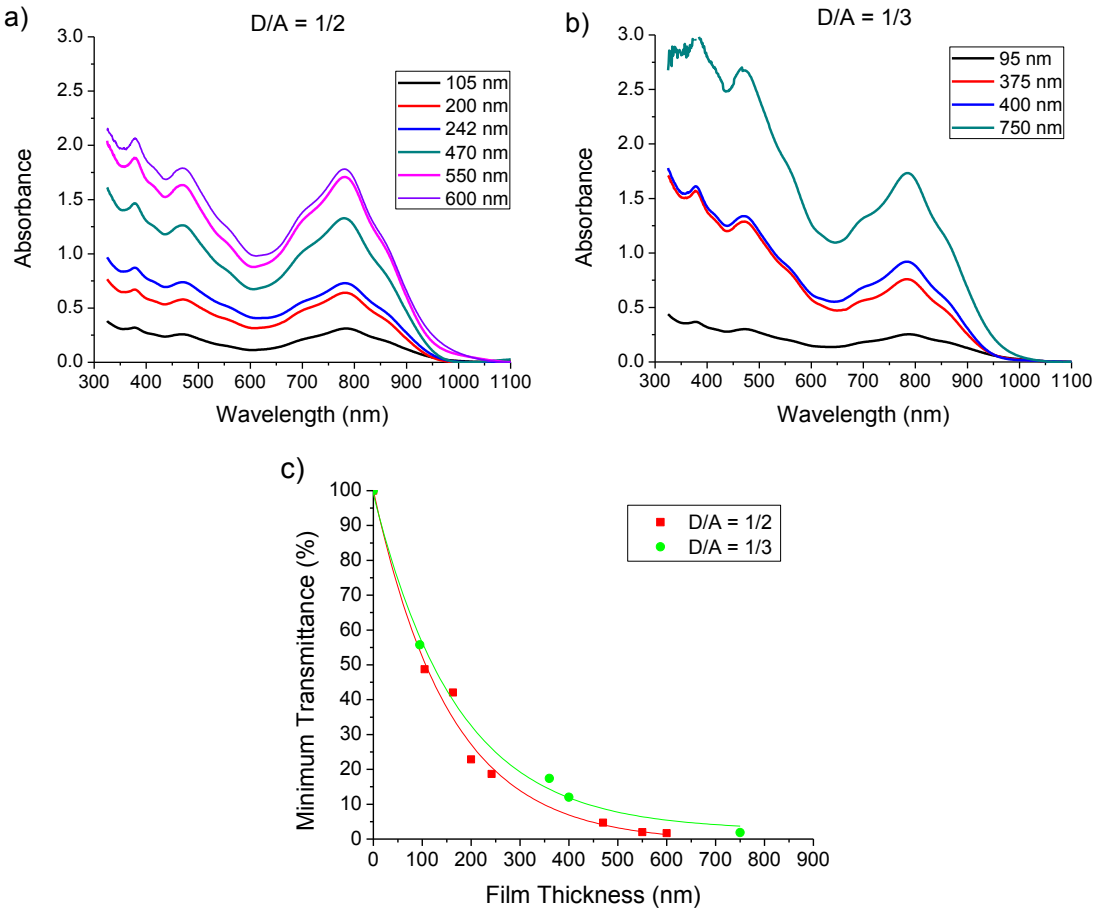


**Figure 36.** UV-Vis absorbance of PDQT:$PC_{71}BM$ films prepared at various active layer thicknesses for D/A ratios of a) 1/2 and b) 1/3. c) Minimum transmittance determined from the Beer-Lambert equation for various ratios of PDQT to $PC_{71}BM$ at different film thicknesses. Minimum transmittance was calculated from the maximum absorbance values at 770 nm.

Standard and inverted OPV devices were prepared using an active layer consisting of PDQT:$PC_{71}BM$ with different D/A ratios. The influence of active layer thickness on PCE and its related parameters (*FF*, $J_{SC}$, and $V_{OC}$) is shown in Figure 37. Similar to the $PC_{61}BM$-based devices, a marked difference

between standard and inverted devices is apparent, particularly when active layers are thick (i.e. > 300 nm).

Overall, the PCE of inverted devices remains fairly consistent when the active layer thickness is high (~550 nm) but standard devices demonstrate a steady decrease in PCE from the thinnest to the thickest active layer. The decrease in PCE of standard devices with D/A ratios of 1/2 and 1/4 occurs more readily at thicknesses greater than 300-350 nm. The decrease in PCE is clearly a result of the decreasing *FF* as thickness increases, as well as the decrease in $J_{SC}$ that occurs at ~300-350 nm. This is similar behaviour to that observed when $PC_{61}BM$ was used as the acceptor.

A comparison of the highest PCE and related parameters achieved using $PC_{71}BM$ versus $PC_{61}BM$ as the acceptor is found in Table 4. The highest efficiency of devices prepared with PDQT:$PC_{71}BM$ is 3.12%, which was achieved using a D/A ratio of 1/3. This PCE is slightly higher than the highest value achieved with PDQT:$PC_{61}BM$ using a D/A ratio of 1/4. It was expected that this increase would be due to a higher $J_{SC}$, however in this case it appears that the improved efficiency of $PC_{71}BM$ devices is due to a higher *FF* value. This is a result of the different D/A ratios and the difference in active layer thickness between the two devices. In the case of $PC_{61}BM$, the greater active layer thickness combined with the higher acceptor content (1/4 versus 1/3) has apparently induced absorption similar to that of $PC_{71}BM$, however the higher *FF* value that occurs in the $PC_{71}BM$ devices is a result of the improved charge balance of the 1/3 ratio and the thinner active layer that leads to a reduction in recombination. A comparison of the highest performing devices with the same D/A ratio (1/3), however demonstrates a higher $J_{SC}$ value when $PC_{71}BM$ is the acceptor, despite the thinner active layer. This supports the argument that $PC_{71}BM$ leads to greater absorption, although it suggests that similar results can be obtained using $PC_{61}BM$ as the acceptor when thicker active layers and the correct D/A ratio are employed.

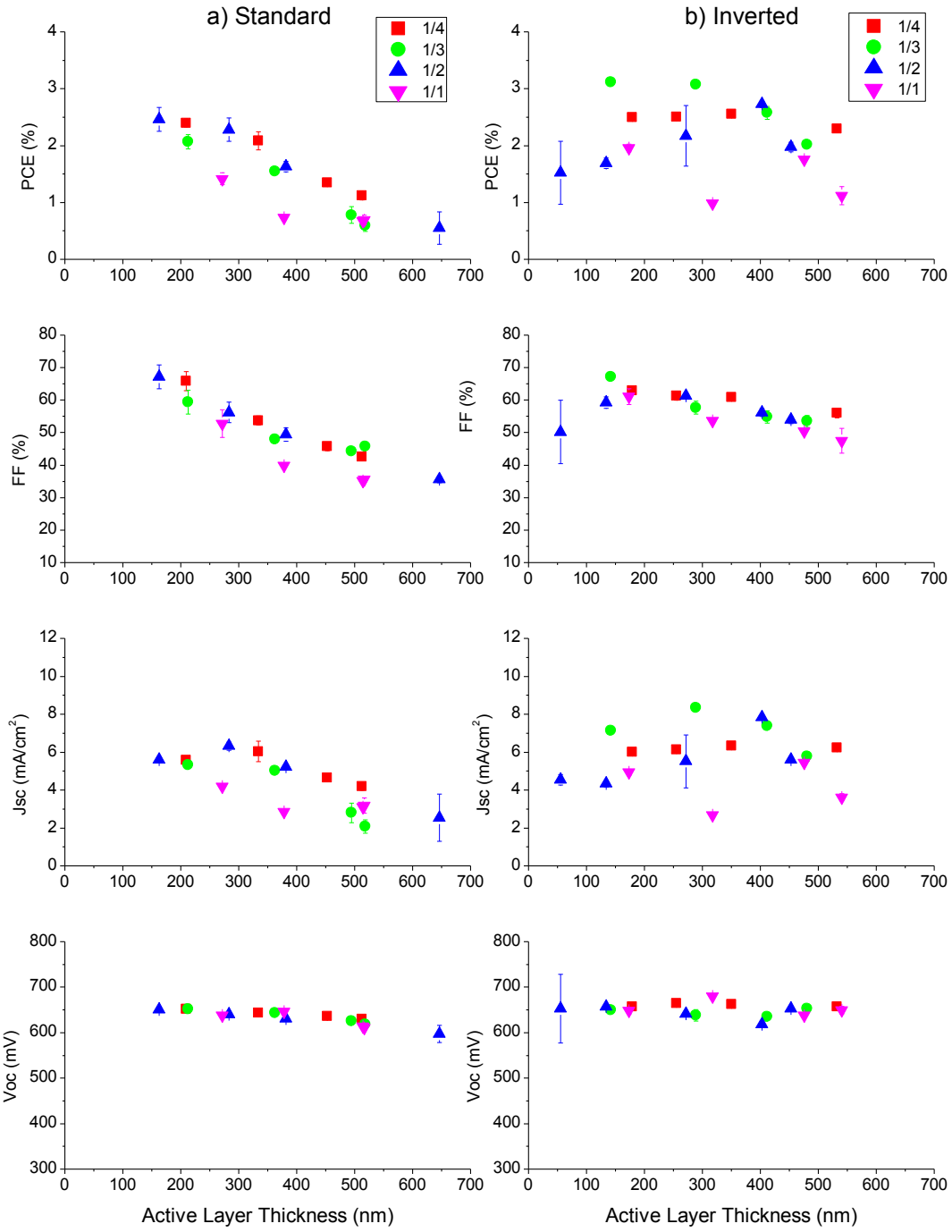


**Figure 37.** Measured power conversion efficiency (PCE), open circuit voltage ($V_{OC}$), fill factor (*FF*) and short-circuit current density ($J_{SC}$) at various active layer thicknesses of PDQT:$PC_{71}BM$ OPV devices fabricated in a) standard and b) inverted configurations using various D/A ratios in the active layer.

**Table 4.** Efficiency parameters of best performing OPV devices prepared using PDQT:$PC_{61}BM$ or PDQT:$PC_{71}BM$ as the active layer.

| Acceptor | D/A Ratio | Thickness (nm) | $J_{SC}$ ($mAcm^{-2}$) | $V_{OC}$ (mV) | *FF* (%) | PCE (%) |
|---|---|---|---|---|---|---|
| $PC_{71}BM$ | 1/3 | 142 | 7.14 | 650 | 67.3 | 3.12 |
| $PC_{61}BM$ | 1/4 | 250 | 7.32 | 657 | 60.3 | 2.90 |
| $PC_{61}BM$ | 1/3 | 280 | 5.91 | 653 | 62.9 | 2.43 |

Similar to the trend observed in PDQT:$PC_{61}BM$ devices, the decline in *FF* of inverted PDQT:$PC_{71}BM$ devices is much slower than that of the standard devices with the same acceptor. The lowest *FF* values of the inverted devices are found within the thickness range of 500-550 nm. These values are greater than 45% and ~10% higher than the values of standard devices with an equivalent D/A ratio. The highest *FF* value achieved using $PC_{71}BM$ (67.3%) is very similar to that achieved using $PC_{61}BM$ (69.5%) as the acceptor, both of which occur when the active layer is relatively thin.

In the previous study involving $PC_{61}BM$, a distinct correlation occurs between *FF* and resistance measurements. Figure 38 shows the $R_{series}$ and $R_{shunt}$ trends of the PDQT:$PC_{71}BM$ devices. $R_{shunt}$ of standard devices decreases as the active layer thickness increases until ~350-400 nm and then levels out at fairly low values. In the inverted devices, the decrease is less apparent due to the insufficient number of data points at thicknesses below 200 nm, however the lowest $R_{shunt}$ values of inverted devices are, in some cases, more than twice as high as those of the standard devices when the active layers are thick (>350 nm). The lower $R_{shunt}$ values of standard devices are suggestive of current losses due to leakage that ultimately leads to lower *FF* values.

The PDQT:$PC_{71}BM$ devices show much lower $R_{series}$ values overall compared to those of the PDQT:$PC_{61}BM$ devices. This is particularly apparent when comparing the standard devices. The majority of PDQT:$PC_{61}BM$ standard devices have $R_{series}$ values greater than 10 $\Omega \cdot cm^2$, whereas when D/A = 1/2, 1/3 or 1/4, the $R_{series}$ values of standard PDQT:$PC_{71}BM$ devices are commonly below 10 $\Omega \cdot cm^2$, particularly when the active layer thickness is less than ~400 nm. The $R_{series}$ values are more similar between inverted devices of the two acceptors. With both acceptors, an increase in $R_{series}$ tends to occur at a thickness of ~400 nm. This increase is less apparent when $PC_{71}BM$ is the acceptor due to the insufficient number of data points at thicknesses greater than 550 nm.

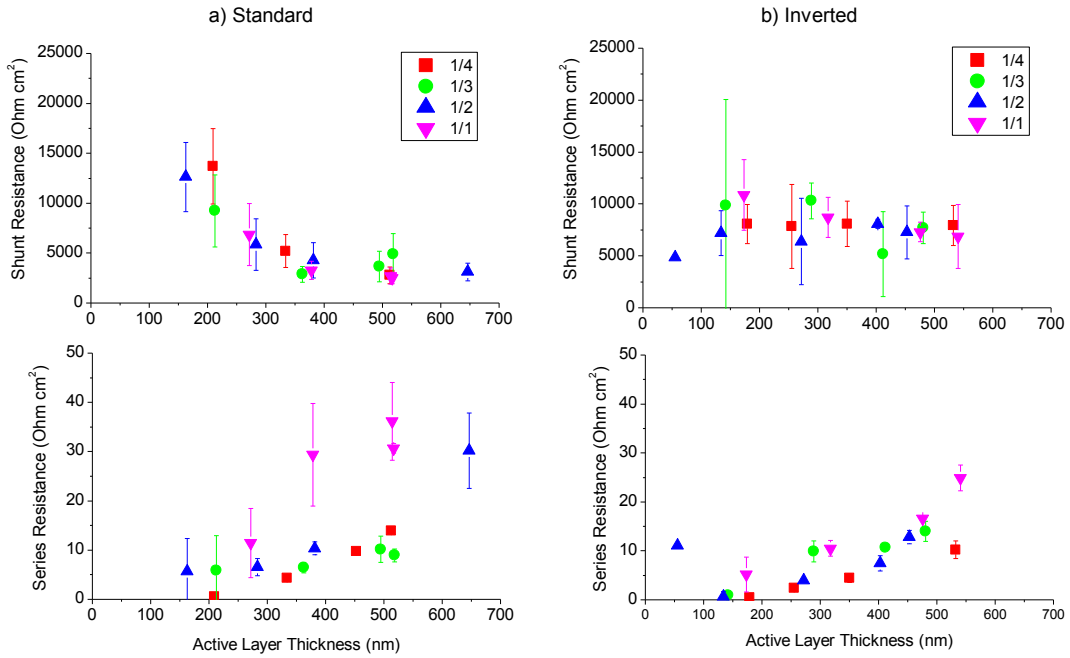


**Figure 38.** Shunt resistance and series resistance at various active layer thicknesses of PDQT:$PC_{71}BM$ OPV devices prepared in a) standard and b) inverted configurations using various D/A ratios in the active layer.

Since $R_{series}$ values of PDQT:$PC_{71}BM$ devices (D/A = 1/2, 1/3 or 1/4) are commonly below 10 $\Omega \cdot cm^2$, it is expected that $R_{series}$ will have less of an impact on the $J_{SC}$ of these devices. In standard devices, the $J_{SC}$ begins to decline at a thickness of ~300-350 nm in devices with lower D/A ratios (1/2, 1/3, 1/4), whereas the devices with D/A = 1/1 start to show a decline in $J_{SC}$ from the lowest measured thickness (~250 nm), perhaps as a result of the high $R_{series}$ that occurs in the 1/1 ratio. In the standard devices, the highest $J_{SC}$ values are similar to the lower values achieved in the inverted configuration. In the inverted devices, however there are some considerably higher $J_{SC}$ values in the 1/2 and 1/3 ratios, and overall $J_{SC}$ values tend to remain high when the active layers are thick. The trend within the inverted devices varies amongst the different ratios. The $J_{SC}$ values of devices with a 1/1 ratio oscillate but the $J_{SC}$ values of D/A = 1/2 devices increase until a thickness of ~400 nm. The $J_{SC}$ values of the 1/3 ratio begin to drop between 300-400 nm and the $J_{SC}$ values of D/A = 1/4 devices remain quite steady across the various thicknesses.

The different trends observed for different D/A ratios in the inverted devices is representative of the optimal active layer thickness required to harvest the majority of sunlight. As the D/A ratio

decreases, absorption in the range of 300-600 nm increases due to the higher quantity of acceptor. With a broader absorption spectrum, the majority of sunlight can then be harvested using a thinner active layer. Therefore, without a significant influence of series resistance, $J_{SC}$ will become level once the maximum absorption is achieved. In PDQT:$PC_{71}BM$ inverted devices with D/A = 1/3, the highest $J_{SC}$ of 8.34 $mAcm^{-2}$ occurs at a thickness of 288 nm. In PDQT:$PC_{61}BM$ inverted devices (D/A = 1/3), the highest $J_{SC}$ of 5.91 $mAcm^{-2}$ occurs at a similar thickness of 280 nm, but is much lower due to the reduced absorption coefficient of $PC_{61}BM$. As the active layer thickness increases, the $J_{SC}$ of the two PDQT:acceptor blends coincide, indicating that maximum absorption has been achieved.

As a final point, $V_{OC}$ is very consistent in both standard and inverted devices at ~650 mV, which is slightly higher than the predicted value. At a thickness of ~450 nm, however, the $V_{OC}$ of standard devices begins to drop slightly. The highest $V_{OC}$ achieved with PDQT:$PC_{71}BM$ is 681 mV, which is almost identical to PDQT:$PC_{61}BM$ devices in which the highest $V_{OC}$ value is 680 mV, thus demonstrating the similarity in the energy levels of $PC_{61}BM$ and $PC_{71}BM$.

The results of this study demonstrate the influence of the acceptor's absorption spectra. These results support the proposed mechanism of charge transport in the standard versus inverted configuration that was presented earlier (Figure 31). The increase in absorption appears to be beneficial only when active layers are thin (i.e. < 400-500 nm). Therefore, when thick active layers are required, the use of $PC_{61}BM$ is sufficient.

### 6.2.2 PDBFBT

PDBFBT was also tested with $PC_{71}BM$ as the acceptor. UV-Vis absorbance measurements (Figure 39) demonstrate the increase in absorption that is achieved by replacing $PC_{61}BM$ with $PC_{71}BM$ in a D/A ratio of 1/3. The increased absorbance is expected to lead to higher charge generation and thus $J_{SC}$ and PCE values.

Inverted devices of varied active layer thickness were prepared with a D/A ratio of 1/3. Efficiency parameters are presented in

Table 5. The highest PCE achieved (2.71%) was with an active layer thickness of 147 nm, which is slightly higher than the PDBFBT:$PC_{61}BM$ device with a similar active layer thickness (2.56%). The parameters of these devices were quite comparable, although *FF* was lower than expected for the device with a thinner active layer. Devices with thicker active layers were expected to perform better,

however no other device exceeded a PCE of 2.71%. Analysis of the parameters of the other PDBFBT:$PC_{71}BM$ devices demonstrates low *FF* and $J_{SC}$ values; both can be attributed to the high $R_{series}$ values.

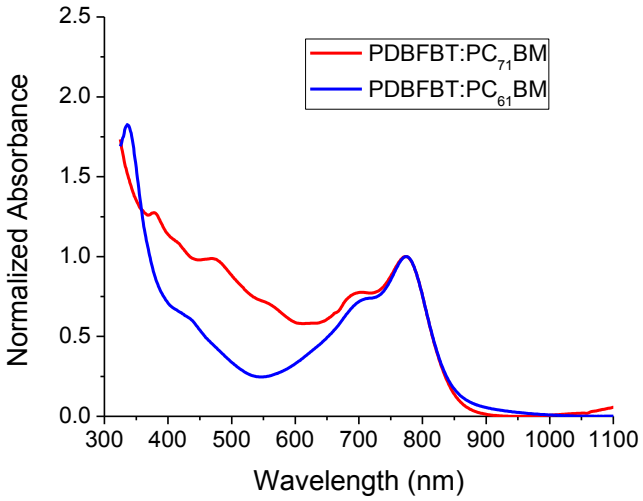


**Figure 39.** UV-Vis absorbance of PDBFT:$PC_{71}BM$ compared to PDBFBT:$PC_{61}BM$ in a D/A ratio of 1/3. Absorbance is normalized for the PDBFBT peak.

**Table 5.** Efficiency parameters of inverted OPV devices prepared using PDBFBT:$PC_{61}BM$ or PDBFBT:$PC_{71}BM$ as the active layer, with various active layer thicknesses.

| Acceptor | D/A Ratio | Thickness (nm) | $J_{SC}$ ($mAcm^{-2}$) | $V_{OC}$ (mV) | *FF* (%) | PCE (%) | $R_{shunt}$ ($\Omega \cdot cm^2$) | $R_{series}$ ($\Omega \cdot cm^2$) |
|---|---|---|---|---|---|---|---|---|
| $PC_{71}BM$ | 1/3 | 377 | 3.02 | 603 | 48.8 | 0.86 | 5555 | 23 |
| $PC_{71}BM$ | 1/3 | 305 | 3.22 | 709 | 43.6 | 1.00 | 4544 | 11 |
| $PC_{71}BM$ | 1/3 | 147 | 6.68 | 700 | 57.9 | 2.71 | 10082 | 2 |
| $PC_{61}BM$ | 1/3 | 370 | 11.05 | 666 | 54.6 | 4.02 | 3479 | 5 |
| $PC_{61}BM$ | 1/3 | 277 | 6.45 | 703 | 60.1 | 2.71 | 8339 | 4 |
| $PC_{61}BM$ | 1/3 | 178 | 5.51 | 709 | 65.6 | 2.56 | 15707 | 0 |

The poor performance due to high $R_{series}$ of inverted OPV devices with PDBFBT:$PC_{71}BM$ blends in comparison with PDBFBT:$PC_{61}BM$ and PDQT:$PC_{71}BM$ blends is suggestive of losses due to poor nanophase separation. Figure 40 displays the morphology of PDBFBT:$PC_{71}BM$ compared to PDQT:$PC_{71}BM$ active layers. The domain size of the PDBFBT:$PC_{71}BM$ blends is quite large,

whereas the domain size of PDQT:$PC_{71}BM$ blends is rather fine and is better suited for charge transport. The device with the thinner active layer was able to perform better than the devices with the thicker active layers due to the shorter distance required for charge transport. The relatively high performance of this device is indicative of the compatibility of PDBFBT and $PC_{71}BM$. Further optimization of the process parameters (casting solvent, DIO concentration, D/A ratio) is required and may lead to very high PCE values.

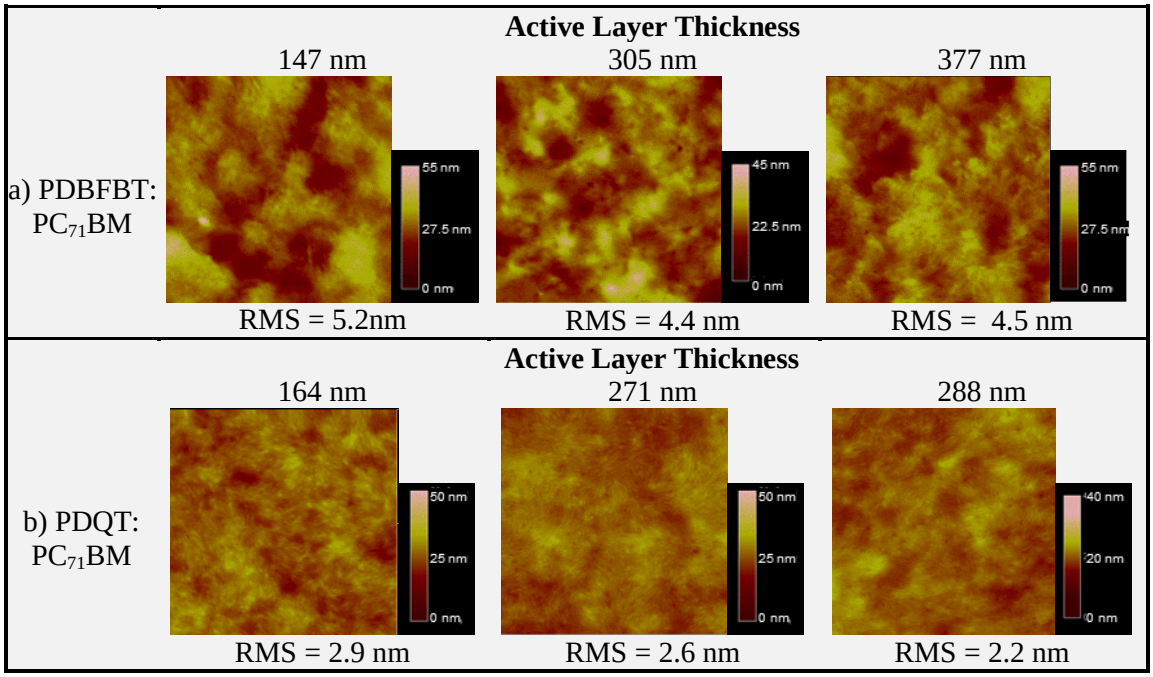


**Figure 40.** AFM images (2 µm × 2 µm) of inverted OPV devices prepared using a) PDBFBT: $PC_{71}BM$ (D/A = 1/3) and b) PDQT: $PC_{71}BM$ (D/A = 1/3).

## 6.3 Conclusions

The use of $PC_{71}BM$ in place of $PC_{61}BM$ allows greater photon absorption in the range of 400-600 nm. This absorption is complimentary to the lower limits of both PDQT and PDBFBT. In PDQT:$PC_{71}BM$ devices, the increase in absorption affects only the $J_{SC}$ values and leads to slightly higher PCE values. This is more apparent in the inverted structure, which can tolerate increases in the active layer thickness when a high $\mu_h$ donor, such as PDQT, is employed due to lower resistance. The results of this study support the proposed mechanism of charge transport in the standard versus inverted configuration, in which the high $\mu_h$ of the donor phase helps achieve a longer hole collection path in

the inverted configuration. The increase in absorption that is contributed by $PC_{71}BM$ appears to be of greatest benefit when active layers are not very thick. Therefore, the use of $PC_{61}BM$ is sufficient when thick active layers (>500 nm) are required.

There is much potential to gain greater efficiencies in PDBFBT:$PC_{71}BM$ devices, however optimization of the process parameters is required to allow better charge transport pathways. This demonstrates the variation imposed with the introduction of new materials, even materials as similar as $PC_{61}BM$ and $PC_{71}BM$.

# Chapter 7.

# Influence of Thermal Annealing

## 7.1 Introduction and Purpose

Thermal annealing is a common technique employed to increase OPV efficiency by inducing a coarser, more crystalline morphology [178–180]. The optimum annealing temperature is specific to the type of polymer but is also influenced by the polydispersity, molecular weight and degree of conjugation of the polymer [125,126].

It was previously demonstrated that the field-effect $\mu_h$ of both PDQT and PDBFBT can be increased upon thermal annealing. Since significant increases in $\mu_h$ of PDBFBT films were associated with thermal annealing, it was of interest to determine if thermal annealing could increase $\mu_h$ in the vertical direction and improve OPV performance in the process.

## 7.2 Results and Discussion

Hole-only devices were first prepared with pure PDBFBT as the active layer. After spin-coating the polymer layer, devices were allowed to sit at room temperature >3 hours (annealing temperature is referred to as 25°C) or were thermally annealed immediately on a hot plate for 10 minutes in the glove box at temperatures ranging from 60°C to 200°C. Film thicknesses were between 330 nm and 440 nm, which was presented earlier as a suitable range for optimal performance (refer to Figure 29). *J-V* characteristics of the devices were measured in the dark (Figure 41a) and $\mu_h$ was determined by fitting the Mott-Gurney equation to the plots (Figure 41b).

As previously demonstrated, PDBFBT films that were allowed to dry at room temperature (25°C) showed rather high SCLC $\mu_h$ ($2.3 \times 10^{-2}$ $cm^2V^{-1}s^{-1}$). Similar, but slightly lower results were obtained with thermal annealing at 60°C but with increased annealing temperature, a linear decrease in $\mu_h$ was observed. Interestingly, all $\mu_h$ values were above the acceptable mobility for OPVs ($10^{-4}$ $cm^2V^{-1}s^{-1}$ [33]) and devices annealed at temperatures of 150°C ($\mu_h = 8.9 \times 10^{-3}$ $cm^2V^{-1}s^{-1}$) or below demonstrated higher mobility than that of P3HT (~$2.5 \times 10^{-3}$ $cm^2V^{-1}s^{-1}$). The decrease in $\mu_h$ with

increased annealing temperature is in direct contrast to the published results [100] in which field-effect $\mu_h$ increased with increased annealing temperature.

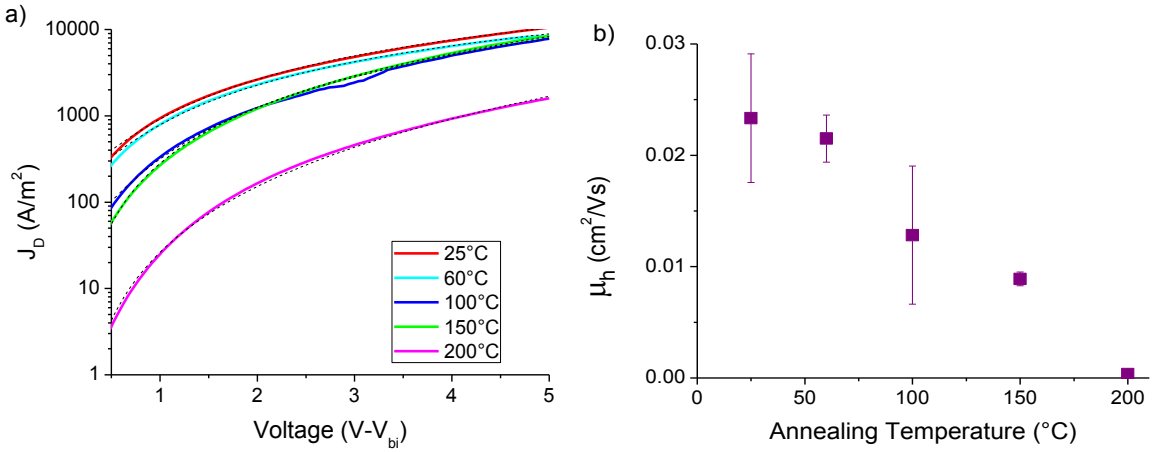


**Figure 41.** a) *J-V* characteristics measured in the dark and fit with the Mott-Gurney equation (black, dotted lines) and b) SCLC $\mu_h$ measurements of hole-only devices annealed at various temperatures, prepared using pure PDBFBT films. Film thicknesses of devices annealed at 25°C, 60°C, 100°C, 150°C and 200°C were 351 nm, 334 nm, 389 nm, 372 nm and 437 nm, respectively.

Analysis of the films by AFM (Figure 42) shows that the grain size of the PDBFBT films decreases as the annealing temperature increases, suggesting an increase in the crystallinity. Furthermore, analysis of the films by UV-Vis absorbance (Figure 43), which were normalized for thickness, demonstrates well-defined absorption peaks at ~695 nm and ~770 nm of those films annealed at 60°C, 100°C and 150°C. The strongest absorbance occurs in the film annealed at 100°C and the weakest absorbance is in the film that was allowed to dry at room temperature (25°C). This suggests a more crystalline form in the 100°C-annealed device since generally the maximum optical absorption of a polymer is directly related to the degree of its crystallinity [144]. This is in agreement with previous work [100], in which it was determined that increasing the annealing temperature led to higher crystallinity in PDBFBT films. The packing of polymer chains in such films was considered to assume a layer-by-layer lamellar configuration, which allows current to flow well in the lateral direction. Coakley *et al*. were able to enhance the SCLC $\mu_h$ of P3HT by a factor of 20 after aligning the polymer chains perpendicular to the substrate using anodic alumina [181]. The results of the current study suggest that the lamellar structure of PDBFBT does not favour hole conduction in the vertical direction, rather the amorphous structure appears to be more favourable for this role.

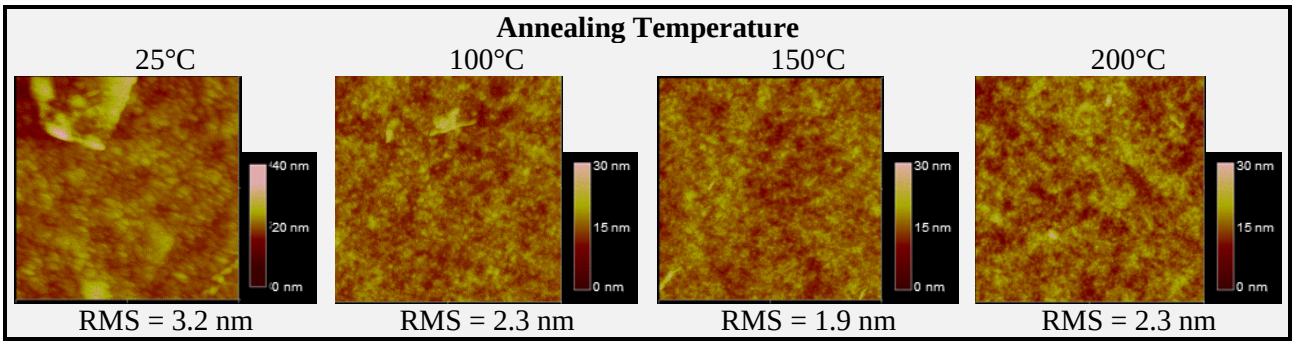


**Figure 42.** AFM images (2 µm × 2 µm) of hole-only devices prepared using PDBFBT with various annealing temperatures.

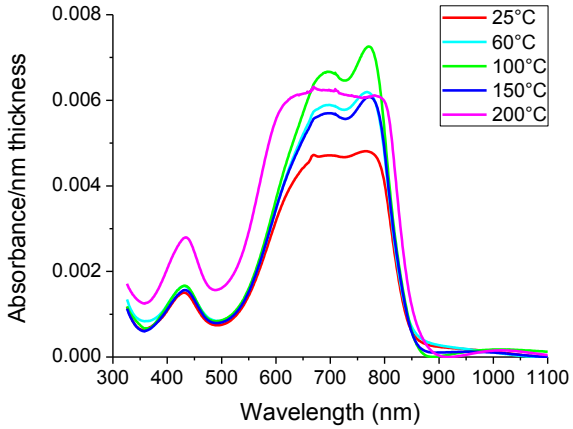


**Figure 43.** Effect of annealing temperature on UV-Vis absorbance of pure PDBFBT films.

The presence of the acceptor is known to impact the mobility of the donor [94], therefore the influence of thermal annealing on charge conduction was studied in blends of PDBFBT:$PC_{61}BM$. For hole-only devices, the same procedure as that of pure PDBFBT was used with D/A blends consisting of various ratios (1/1, 1/2, 1/3 and 1/4). Figure 44a demonstrates that in the non-annealed films (25°C), the presence of $PC_{61}BM$ was found to lower $\mu_h$ compared to that of pure PDBFBT (25°C). Similar $\mu_h$ values were obtained amongst the different D/A ratios. An increase in the annealing temperature had little effect overall on the $\mu_h$ of D/A = 1/4 films. In other D/A ratios, $\mu_h$ remained fairly constant throughout the range of annealing temperatures from 60°C to 150°C. In this temperature range, $\mu_h$ values for D/A = 1/2 and 1/3 were slightly higher than the non-annealed blends

but were quite similar to the non-annealed pure films. $\mu_h$ values for D/A = 1/1 and 1/4 were approximately half the magnitude of the non-annealed pure films but were comparable to the similarly annealed pure films. Interestingly, a sizeable increase in $\mu_h$ was observed in D/A = 1/1, 1/2 and 1/3 devices annealed at 200°C, in some cases surpassing the highest value obtained for pure PDBFBT films by more than double. The presence of $PC_{61}BM$ must therefore influence the crystallization of PDBFBT at high temperatures to allow better hole transport in the vertical direction, particularly when the D/A ratio is 1/3 and 1/2.

$\mu_e$ was measured from electron-only devices annealed at various temperatures (Figure 44b). Since $\mu_e$ tends to be low in comparison with $\mu_h$, PDBFBT:$PC_{61}BM$ ratios with higher acceptor content (D/A = 1/3 and 1/4) were studied. In both ratios, $\mu_e$ was highest in devices annealed at 100°C but was extremely low in devices annealed at 150°C and 200°C. The highest $\mu_e$ was achieved using the highest D/A ratio of 1/4 with an annealing temperature of 100°C. In this case, $\mu_e$ ($1.25 \times 10^{-2}$ $cm^2V^{-1}s^{-1}$) is greater than $\mu_h$ ($3.97 \times 10^{-3}$ $cm^2V^{-1}s^{-1}$) of the same ratio and annealing temperature. It would seem that the best balance in charge mobility is achieved without annealing using a D/A ratio of 1/4; despite earlier results demonstrating that the best performance was achieved using a D/A ratio of 1/3.

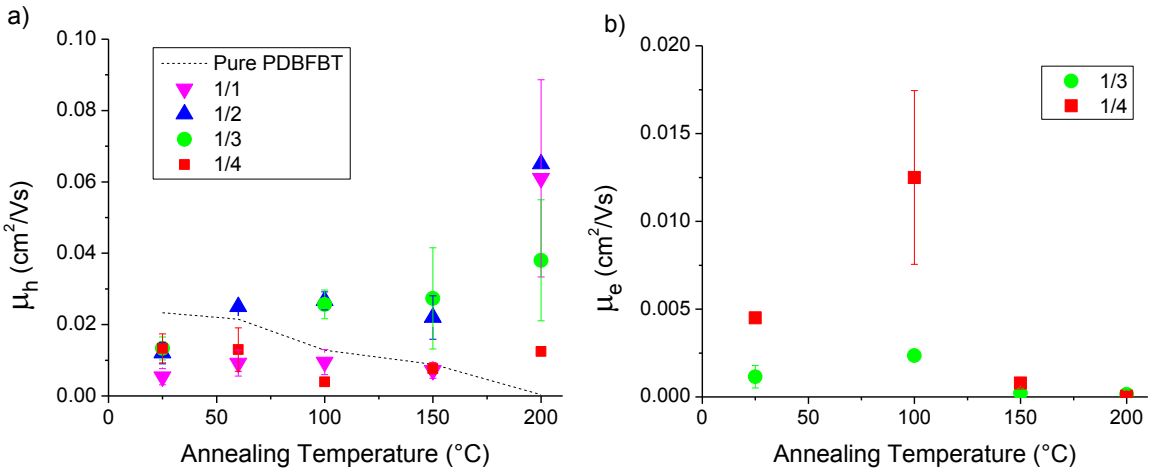


**Figure 44.** SCLC mobility measurements of a) hole-only and b) electron-only devices annealed at various temperatures with various D/A ratios. Refer to Appendix 1, Figure A1-1 for Mott-Gurney fittings of *J-V* data and Table A1-1 for active layer thicknesses.

Since devices with D/A = 1/3 have thus far demonstrated the best performance, annealing studies on OPVs were performed using the same ratio. Both inverted and standard OPV devices were prepared using an active layer consisting of PDBFBT:$PC_{61}BM$ (D/A=1/3). Devices were annealed as

previously described. *J-V* characteristics of the devices were measured under illumination and in the dark (Figure 45). In the inverted structure, active layer thicknesses were quite consistent, from 303 nm to 362 nm, and were within a range expected to provide maximum efficiencies (refer to Figure 29). As the annealing temperature was increased from 25°C to 200°C, all efficiency parameters ($J_{SC}$, $V_{OC}$, *FF* and PCE) were observed to decrease (Table 6). *FF* values decreased somewhat over the range of annealing temperatures tested. The drop in PCE, however appears to be mainly a result of declining $V_{OC}$ and $J_{SC}$ values. Generally low *FF*, $J_{SC}$, and to some extent $V_{OC}$ values can be associated with high $R_{series}$. Here, $R_{series}$ values are rather high ($\geq 10\ \Omega \cdot cm^2$) when annealing temperatures are 100°C and greater, suggesting that thermal annealing of PDBFBT leads to obstructed charge flow. The obstructed charge flow would be expected to lead to greater leakage and thus low $R_{shunt}$ values, however in this case a rise in $R_{shunt}$ is observed when annealing temperature is increased.

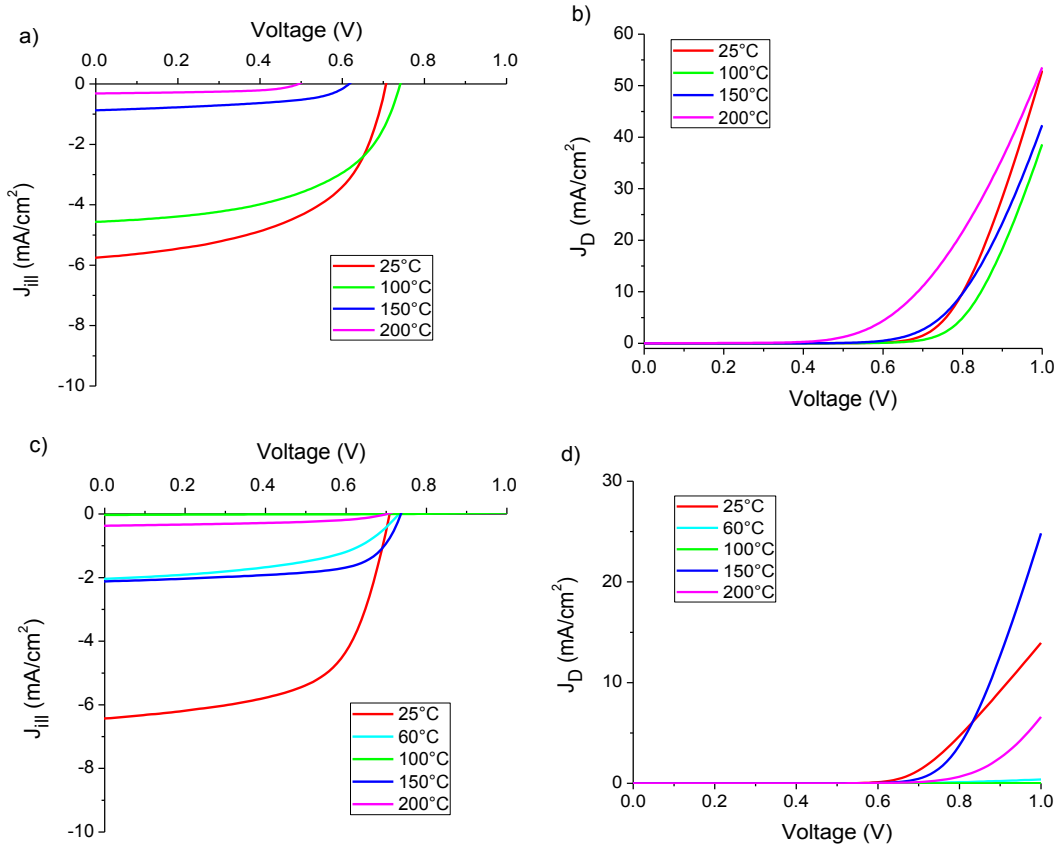


**Figure 45.** *J-V* characteristics of inverted OPV devices a) illuminated and b) dark curves, and standard OPV devices c) illuminated and d) dark curves annealed at various temperatures, prepared with PDBFBT:$PC_{61}BM$ (D/A = 1/3).

In standard OPV devices, the active layer thicknesses showed greater variation, ranging from 160 nm to 378 nm. Similar to the inverted devices, standard devices with active layers in the range of 278 nm to 378 nm displayed an overall decrease in efficiency parameters ($J_{SC}$, $V_{OC}$, *FF* and PCE) as the annealing temperature was increased (Table 6). (Note: due to the unusual $R_{series}$ and $R_{shunt}$ values, the 100°C-annealed device will be neglected in this analysis.) There is a noticeable difference in $J_{SC}$ and *FF* between devices annealed at 25°C versus 200°C. $V_{OC}$, on the other hand remains high in the 200°C-annealed devices and is somewhat consistent with that of the 25°C devices. Within this range of thicknesses, it can be seen that $R_{series}$ values are very high ($\geq 12\ \Omega \cdot cm^2$), even in the 25°C devices and $R_{shunt}$ values also tend to increase with increased annealing temperatures, similar to the results observed using inverted devices.

**Table 6.** Efficiency parameters of inverted and standard OPV devices annealed at various temperatures, prepared using PDBFBT:$PC_{61}BM$ films with D/A = 1/3.

| | **Annealing Temperature (°C)** | **Active Layer Thickness (nm)** | $J_{SC}$ **(mAcm$^{-2}$)** | $V_{OC}$ **(mV)** | ***FF*** **(%)** | **PCE (%)** | $R_{shunt}$ **(Ω·cm$^2$)** | $R_{series}$ **(Ω·cm$^2$)** |
|---|---|---|---|---|---|---|---|---|
| Inverted | 25 | 303 | 5.78 | 706 | 53.6 | 2.19 | 8232 | 4 |
| | 100 | 311 | 4.49 | 740 | 53.0 | 1.76 | 12533 | 10 |
| | 150 | 313 | 0.75 | 633 | 49.2 | 0.23 | 21333 | 28 |
| | 200 | 362 | 0.24 | 405 | 44.9 | 0.05 | 42349 | 91 |
| Standard | 25 | 278 | 5.88 | 706 | 58.0 | 2.42 | 7383 | 12 |
| | 60 | 302 | 1.93 | 732 | 47.7 | 0.68 | 13478 | 58 |
| | 100 | 278 | 0.02 | 502 | 23.1 | 0.00 | $33\times10^{-7}$ | 76720 |
| | 150 | 160 | 1.99 | 735 | 65.5 | 0.96 | 21889 | 1 |
| | 200 | 378 | 0.28 | 698 | 42.3 | 0.08 | 47473 | 326 |

Unlike the other devices, the 150°C-annealed device has a much lower active layer thickness of 160 nm. The *FF* and $V_{OC}$ of this device are higher than those of all other devices in this group. The $J_{SC}$ is higher than that of all other thermally annealed devices but remains lower than the 25°C device. $R_{series}$ is extremely low ($1\ \Omega \cdot cm^2$) and therefore is expected to have a minimal negative impact on the efficiency parameters. $R_{shunt}$ of the 150°C-annealed device is consistent with the trend of increasing $R_{shunt}$ with increased annealing temperature.

UV-Vis spectra of standard (Figure 46a) and inverted (Figure 46b) OPV devices annealed at various temperatures were normalized for active layer thickness. In both cases, the absorption strength of the

200°C-annealed film is the lowest. Moreover, the $PC_{61}BM$ peak at ~400 nm is much weaker in the 200°C-annealed films than those annealed at other temperatures. In both device architectures, the strongest absorption is found in the 25°C and 100°C-annealed devices, suggesting better crystallinity in the non-annealed and 100°C-annealed devices. When compared to the pure PDBFBT UV-Vis spectra, this demonstrates that the presence of $PC_{61}BM$ improves the crystallinity of non-annealed PDBFBT but has little effect on the annealed films.

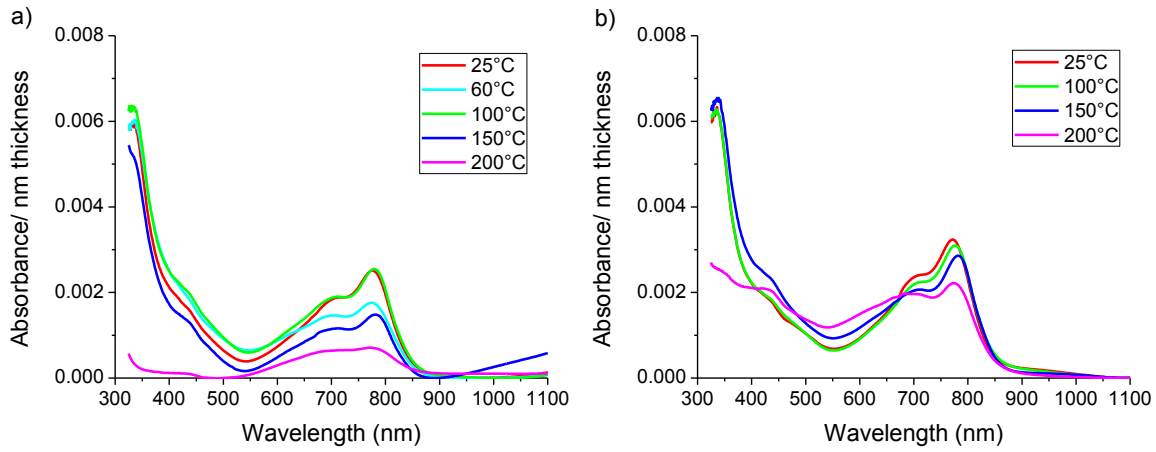


**Figure 46.** Effect of annealing temperature on UV-Vis absorbance of PDBFBT:$PC_{61}BM$ (D/A = 1/3) films in a) standard OPV and b) inverted OPV devices.

The effect of annealing has been well studied in BHJ films, particularly in P3HT:$PC_{61}BM$ blends [178–180,182–188]. It is generally agreed that annealing can lead to improved morphology through better crystallinity and improved domain size of the interpenetrating BHJ components. Variations in annealing temperature and time will certainly influence the quality of the resulting film [189]. Several groups have found that high temperature annealing can have a profound effect on the behaviour and organization of $PC_{61}BM$ within the blend. When the annealing temperature is high, $PC_{61}BM$ diffusion is accelerated within the blend film causing it to readily aggregate and form large clusters through Ostwald ripening [165,182,190–196]. Swinnen *et al.* demonstrated that thermal annealing of P3HT:$PC_{61}BM$ blend films from 125°C to 175°C caused rapid formation of needle-like $PC_{61}BM$ clusters up to a few hundred micrometers in length. Accordingly, $PC_{61}BM$-depleted regions were found to occur throughout the blend films [190].

The major advantage of BHJ active layers has typically been the greater interfacial area offered between interpenetrating donor and acceptor domains. This benefit, of course, is lost if large

aggregates are formed during thermal annealing. The consequence of enlarged domain sizes with reduced interfacial area is a reduction in $J_{SC}$ [195,197]. Both inverted and standard PDBFBT:$PC_{61}BM$ OPV devices displayed a reduction in $J_{SC}$ as annealing temperature was increased, indicating the probability of $PC_{61}BM$ aggregation. Likewise, the observed increase in $R_{series}$ due to obstructed charge flow would also be a result of enlarged $PC_{61}BM$ domains [132].

The various PDBFBT:$PC_{61}BM$ BHJ devices displayed many characteristics that support the possibility of increasing $PC_{61}BM$ domains with increased annealing temperature. At an annealing temperature of 100°C, electron-only devices demonstrated an increase in $\mu_e$. This would be expected with the formation of small $PC_{61}BM$ aggregates that allow better electron transport. At annealing temperatures of 150°C and 200°C, however there was a reduction in $\mu_e$, which would occur as the aggregates increase in size and become engulfed within the PDBFBT phase. Without a continuous network of $PC_{61}BM$ connecting the electrodes, electron transport would be extremely poor. $\mu_h$, on the other hand, was found to increase significantly in the 200°C-annealed devices in D/A ratios with a lower quantity of $PC_{61}BM$ (D/A = 1/1, 1/2 and 1/3). This would be expected to occur when the quantity of $PC_{61}BM$ is low enough that it doesn't disrupt the PDBFBT phase upon agglomeration. Additionally, the presence of large $PC_{61}BM$ clusters may drive the crystallization of PDBFBT into a vertical orientation.

Interestingly, in both OPV device architectures, an increase in $R_{shunt}$ was found to occur as annealing temperature was increased. The presence of shunt current is an indication of losses that can result from non-uniformity, defects, or complexes formed by contact materials [198]. Normally high $R_{shunt}$ values contribute to reduced leakage current and are therefore associated with improved device performance. In this study, the high $R_{shunt}$ values did not lead to improved performance, however they are an indication that the shunt paths have been reduced, which may be a result of reduced surface area caused from the aggregation of $PC_{61}BM$. Additionally, the high $R_{shunt}$ may be a result of fewer pinhole defects in the PDBFBT phase, which would also contribute to the improved $\mu_h$ previously observed.

In order to determine if morphological changes, such as enlarged domains and regions of depletion, were apparent in the annealed films, analysis of the various PDBFBT:$PC_{61}BM$ BHJ devices was performed using AFM. Inverted OPV devices (Figure 47a) showed an increase in both grain size and roughness as the annealing temperature was increased. The 200°C-annealed film showed domains as large as 0.5 µm in diameter. Standard devices (Figure 47b) on the other hand, show fibre-like crystals

that increase in size with increased annealing temperature. There is little difference amongst the roughness of standard devices annealed at 25°C, 100°C and 150°C. The 200°C-annealed device, however is slightly rougher than other standard devices but lower than the inverted devices annealed at 150°C and 200°C.

Analysis of annealing-related morphological changes in other PDBFBT:$PC_{61}$BM BHJ devices shows a slight decrease in the grain size of the hole-only films annealed from 25°C to 150°C (Figure 47c). Roughness also is found to decrease over this range. Annealing at 200°C, however appears to increase the domain size and roughness. In contrast, the change in morphology throughout the electron-only devices (Figure 47d) is much greater, with increasing domain size as the annealing temperature is increased and a six-fold increase in roughness between 100°C-annealed films versus 150°C-annealed films. Parnell *et al*. also documented an increase in surface roughness of P3HT:$PC_{61}$BM films associated with increased annealing temperature. They found that thermal annealing induced $PC_{61}$BM diffusion to the film surface, which caused the increased roughness [199].

In each type of device containing a PDBFBT:$PC_{61}$BM BHJ, it was found that an increase in the annealing temperature leads to strong changes in the film morphology. The temperature-induced transformation of electron-only devices is very similar to that of inverted OPV devices. Inverted and electron-only devices are prepared on films of ZnO that have been produced by annealing the zinc acetate precursor at a very high temperature (180°C). In contrast, standard and hole-only devices are prepared on films of PEDOT:PSS that have been annealed mainly for the purpose of water removal. It was therefore of interest to determine if the ZnO under layer had been influenced by the increased annealing temperatures. The organic component was removed from the electron-only devices and the ZnO layer was examined by AFM (Figure 47e). The ZnO layers appear fairly consistent throughout the various annealing temperatures in both grain size and roughness. This suggests that the differences in morphology of the BHJ films annealed at various temperatures stem directly from changes occurring within the active layer.

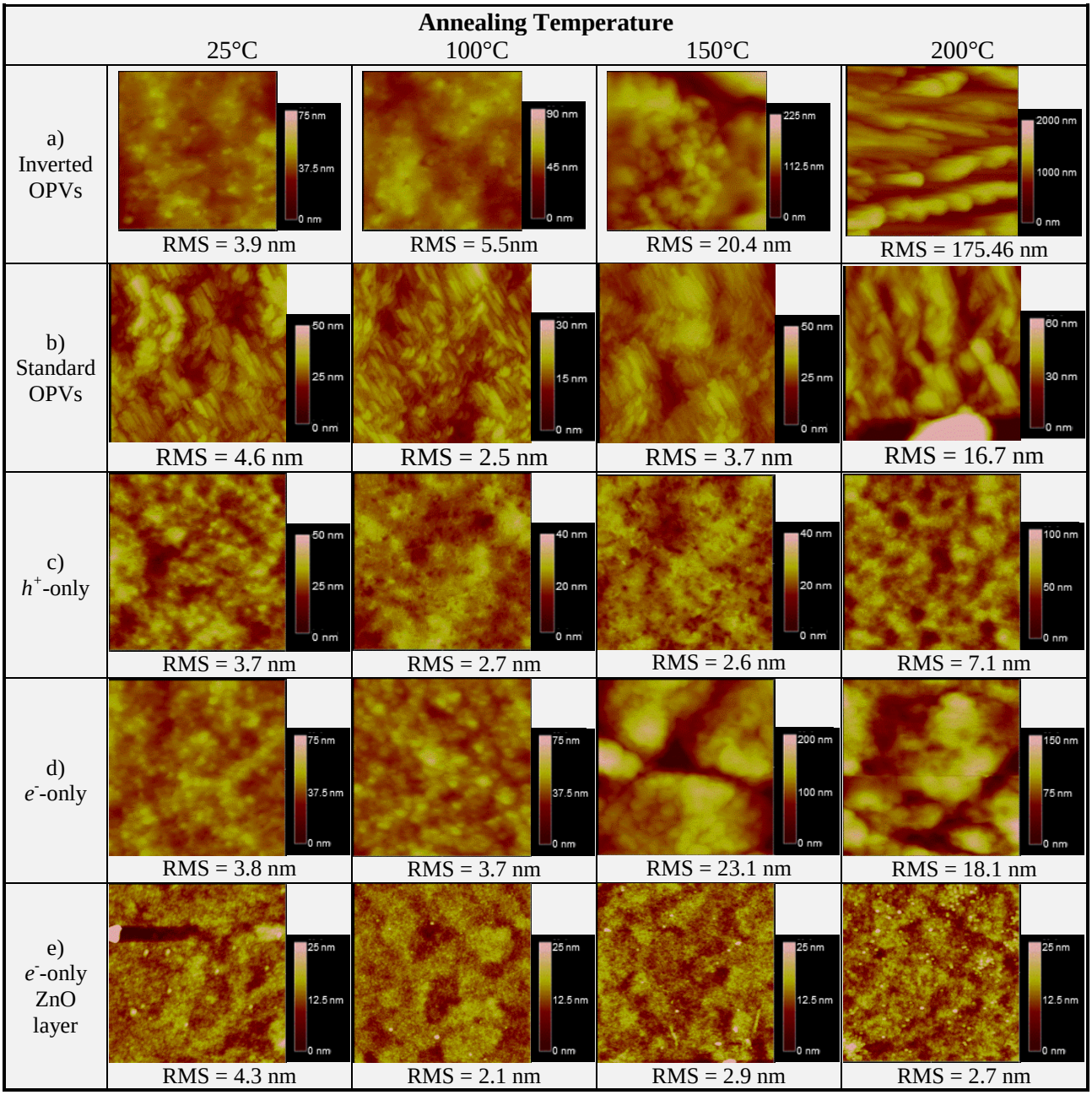


**Figure 47.** AFM images (2 μm × 2 μm) of a) inverted OPV devices, b) standard OPV devices, c) hole-only and d) electron-only devices prepared using PDBFBT:$PC_{61}BM$ (D/A = 1/3) with various annealing temperatures. e) ZnO layer of the same electron-only devices after removal of the active layer.

## 7.3 Conclusions

Earlier studies of PDBFBT found that field-effect $\mu_h$ increases as the annealing temperature is increased. Thermal annealing improves the crystallinity of PDBFBT; however SCLC $\mu_h$ of pure PDBFBT films decreases with increased annealing temperature. This suggests that the improved crystallinity of PDBFBT is oriented in the lateral direction as opposed to the vertical direction, thereby directing charge flow horizontal to the surface. With the addition of $PC_{61}BM$ in D/A ratios of 1/2 and 1/3, SCLC $\mu_h$ increases with thermal annealing and surpasses the highest value achieved using pure films. This suggests that an optimal amount of $PC_{61}BM$ can contribute to directing the crystallization of PDBFBT in the vertical direction.

Standard and inverted OPV devices prepared with PDBFBT:$PC_{61}BM$ (D/A = 1/3) show decreasing efficiency with increased annealing temperature. This is attributed to agglomeration of $PC_{61}BM$ that is known to result from an increase in annealing temperature. The results of this study demonstrate that thermal annealing is not beneficial for PDBFBT:$PC_{61}BM$ films in OPV applications.

# Chapter 8.

# Summary and Future Direction

Two DPP-based d-a copolymer analogues, PDQT and PDBFBT, were selected to study as OPV donor materials. The polymers were of interest due to their analogous structure and their high field effect $\mu_h$. Although lower than the published field-effect $\mu_h$ values, the SCLC $\mu_h$ values of PDQT and PDBFBT are similar to each other and almost ten times greater than that of P3HT, demonstrating that these polymers show high hole mobility in the vertical direction as well as the lateral direction.

Optimization of the casting solvent, active layer thickness and donor to acceptor ratio (D/A) are important steps that were performed on both polymers. Consistent with the majority of literature surrounding DPP-based polymers, a blend of chloroform/o-dichlorobenzene (4:1 v/v) is the best choice of solvent for both PDQT and PDBFBT. The chloroform improves solubility of the DPP-based polymers, while allowing better control over the thickness of the active layer. A small quantity (0.5-1% v/v) of the solvent additive, 1,8-diiodooctane, is necessary to provide a finer nanophase separation in the BHJ films of both polymers.

For charge balance, the high donor $\mu_h$ necessitates a much higher proportion of acceptor in the blend. For PDQT, the D/A ratio that gives the highest PCE (2.9%) is 1/4, although the 1/3 and 1/2 ratios also demonstrate comparable performance. The optimal D/A ratio for PDBFBT is 1/3, which achieves demonstrably higher PCE (4.0%) than the other ratios. However, if the proportion of acceptor is too high, this can lead to poor performance due to discontinuity of the donor phase and lower overall absorption at a given film thickness. The design and synthesis of compatible acceptor materials with high $\mu_e$ (~1 $cm^2V^{-1}s^{-1}$) will therefore be key in further research directed at the application of high mobility donors in OPV systems.

The balance of hole and electron mobility is also influenced by the active layer thickness. The highest PCEs were achieved at thicknesses between 200-400 nm, which is much thicker than most high efficiency OPVs (~100 nm). The high $\mu_h$ of the donors reduces charge recombination at higher thicknesses, resulting in higher *FF*. The increase in absorption within this thickness range is therefore visible through higher PCE values. These results show that the use of high hole mobility polymers,

PDQT and PDBFBT, allows the fabrication of OPVs with thick active layers without undermining the photovoltaic parameters.

A comparison between standard and inverted devices demonstrates that the inverted configuration is more suitable for achieving thicker active layers (up to 1 μm) when using a high hole mobility donor. This was attributed to the high hole mobility of the donor phase that helps achieve a longer hole collection path in the inverted configuration. The thickness dependence of PCE is governed by the charge collection distance of the carrier going towards the electrode farthest from the light source. For inverted devices the mobility of the donor is more critical, whereas balancing the hole and electron mobilities is less important. This suggests that the mobility of the acceptor may be more relevant in standard devices and that acceptors with high electron mobility (~1 $cm^2V^{-1}s^{-1}$) may lead to thicker active layers in the standard device configuration. These results show that high mobility in the donor and/or acceptor materials, as well as a suitable device configuration, are key factors for achieving high performance OPV devices with thick active layers.

Replacing $PC_{61}BM$ with $PC_{71}BM$ allows greater photon absorption in the range of 400-600 nm, which is complimentary to the lower limits of both PDQT and PDBFBT. The increase in absorption leads to higher $J_{SC}$ and thus PCE values when the process parameters are properly optimized. This is more apparent in the inverted structure, which can tolerate increases in the active layer thickness when a high $\mu_h$ donor is employed. Despite the change in acceptor, the high $\mu_h$ of the donor phase continues to achieve a longer hole collection path in the inverted configuration and allows thicker active layers. The increase in absorption that is contributed by $PC_{71}BM$, however appears to be of greatest benefit when active layers are not very thick. Therefore, the use of $PC_{61}BM$ is sufficient when thick active layers (>500 nm) are required.

Finally, it was demonstrated that thermal annealing improves the crystallinity of PDBFBT, however SCLC $\mu_h$ of pure PDBFBT films decreases with increased annealing temperature. This, combined with thermal annealing-related high field-effect $\mu_h$ that was previously published, suggests that the improved crystallinity of PDBFBT is oriented in the lateral direction as opposed to the vertical direction, thereby directing charge flow horizontal to the surface. With the addition of $PC_{61}BM$ in D/A ratios of 1/2 and 1/3, SCLC $\mu_h$ increases with thermal annealing and surpasses the highest value achieved using pure films. This suggests that an optimal amount of $PC_{61}BM$ can contribute to directing the crystallization of PDBFBT in the vertical direction. However, the efficiency of standard and inverted OPV devices prepared with PDBFBT:$PC_{61}BM$ (D/A = 1/3) decreases with increased

annealing temperature. This is attributed to agglomeration of $PC_{61}BM$ that is known to result from an increase in annealing temperature. The results of this study demonstrate that thermal annealing is not beneficial for PDBFBT:$PC_{61}BM$ films in OPV applications. Further studies of thermal annealing of PDBFBT would be of interest using an acceptor that does not tend to agglomerate.

Future work in the field of high hole mobility donor polymers will benefit from the development of new high electron mobility acceptors. Solution-processable DPP-based acceptors that are capable of dissolving in the same solvent as DPP-based donors are currently being explored, however electron mobility tends to be rather low [148,200,201]. Alternatively, charge mobility balance may be accomplished through the use of n-type inorganic semiconductors (i.e. ZnO, $TiO_2$), which are known for their high electron mobility as well as high electron affinity and good stability [202]. The PCE of such hybrid solar cells currently remains much lower than that of their fullerene-based counterparts, however novel methods for efficiency improvements are constantly being developed [29,34,203,204].

All of the studies presented in this work involve the use of high hole mobility polymer semiconductors as donor materials for OPV applications. This work will provide a deeper understanding of the properties required for the development of new semiconductor materials in OPV applications. Furthermore, this work will be very useful for the design of device structures for more feasible manufacturing of large area OPV devices via high speed roll-to-roll printing processes.

# References


[1] J. Perlin, The silicon solar cell turns 50, NREL Report No. BR-520-33947. (2004) 1–4.

[2] D. Kearns, M. Calvin, Photovoltaic effect and photoconductivity in laminated organic systems, The Journal of Chemical Physics. 29 (1958) 950–951.

[3] G.A. Chamberlain, Organic solar cells: A review, Solar Cells. 8 (1983) 47–83.

[4] G. Yu, J. Gao, C. Hummelen, F. Wudl, A.J. Heeger, Polymer photovoltaic cells: enhanced efficiencies via a network of internal donor-acceptor heterojunctions, Science. 270 (1995) 1789–1791.

[5] C.J. Brabec, Organic photovoltaics: Technology and market, Solar Energy Materials and Solar Cells. 83 (2004) 273–292.

[6] J. Kalowekamo, E. Baker, Estimating the manufacturing cost of purely organic solar cells, Solar Energy. 83 (2009) 1224–1231.

[7] C.A. Wolden, J. Kurtin, J.B. Baxter, I. Repins, S.E. Shaheen, J.T. Torvik, A.A. Rockett, V.M. Fthenakis, E.S. Aydil, Photovoltaic manufacturing: Present status, future prospects, and research needs, Journal of Vacuum Science & Technology A: Vacuum, Surfaces, and Films. 29 (2011) 030801.

[8] S. Günes, H. Neugebauer, N.S. Sariciftci, Conjugated polymer-based organic solar cells, Chemical Reviews. 107 (2007) 1324–1338.

[9] Heliatek, Heliatek consolidates its technology leadership by establishing a new world record for organic solar technology with a cell efficiency of 12% [Press release], 2013.

[10] C.D. Dimitrakopoulos, D.J. Mascaro, Organic thin-film transistors: A review of recent advances, IBM Journal of Research and Development. 45 (2001) 11–27.

[11] H. Hoppe, N.S. Sariciftci, Organic solar cells: An overview, Journal of Materials Research. 19 (2004) 1924–1945.

[12] B.A. Gregg, M.C. Hanna, Comparing organic to inorganic photovoltaic cells: Theory, experiment, and simulation, Journal of Applied Physics. 93 (2003) 3605–3613.

[13] H. Chen, Y. Guo, G. Yu, Y. Zhao, J. Zhang, D. Gao, H. Liu, Y. Liu, Highly π-extended copolymers with diketopyrrolopyrrole moieties for high-performance field-effect transistors, Advanced Materials. 24 (2012) 4618–4622.

[14] J.S. Lee, S.K. Son, S. Song, H. Kim, D.R. Lee, K. Kim, M.J. Ko, D.H. Choi, B. Kim, J.H. Cho, Importance of solubilizing group and backbone planarity in low band gap polymers for

high performance ambipolar field-effect transistors, Chemistry of Materials. 24 (2012) 1316–1323.

[15] H. Bronstein, Z. Chen, R.S. Ashraf, W. Zhang, J. Du, J.R. Durrant, P.S. Tuladhar, K. Song S.E. Watkins, Y. Geerts, M.M. Wienk, R.A.J. Janssen, T. Anthopolous, H. Sirringhaus, M. Heeney, I. McCulloch, Thieno[3,2-b]thiophene-diketopyrrolopyrrole-containing polymers for high-performance organic field-effect transistors and organic photovoltaic devices, Journal of the American Chemical Society. 133 (2011) 3272–3275.

[16] J. Li, Y. Zhao, H.S. Tan, Y. Guo, C.-A. Di, G. Yu, Y. Liu, M. Lin, S.H. Lim, Y. Zhou, H. Su, B.S. Ong, A stable solution-processed polymer semiconductor with record high-mobility for printed transistors, Scientific Reports. 2 (2012) 1–9.

[17] S. Tiwari, N.C. Greenham, Charge mobility measurement techniques in organic semiconductors, Optical and Quantum Electronics. 41 (2009) 69–89.

[18] K. Lee, J.Y. Kim, W. Ma, A.J. Heeger, New architecture for thermally stable high efficiency polymer solar cells, Proceedings of SPIE. 5938 (2005) 59380B–1–59380B–12.

[19] Y. Sun, C.J. Takacs, S.R. Cowan, J.H. Seo, X. Gong, A. Roy, A.J. Heeger, Efficient, air-stable bulk heterojunction polymer solar cells using MoO(x) as the anode interfacial layer, Advanced Materials. 23 (2011) 2226–2230.

[20] D.W. Zhao, S.T. Tan, L. Ke, P. Liu, A.K.K. Kyaw, X.W. Sun, G. Q. Lo, D. L. Kwong, Optimization of an inverted organic solar cell, Solar Energy Materials and Solar Cells. 94 (2010) 985–991.

[21] M.D. Irwin, D.B. Buchholz, A.W. Hains, R.P.H. Chang, T.J. Marks, p-Type semiconducting nickel oxide as an efficiency-enhancing anode interfacial layer in polymer bulk-heterojunction solar cells, PNAS. 105 (2008) 2783–2787.

[22] J. Jung, D.L. Kim, S.H. Oh, H.J. Kim, Stability enhancement of organic solar cells with solution-processed nickel oxide thin films as hole transport layers, Solar Energy Materials and Solar Cells. 102 (2012) 103–108.

[23] M.S. White, D.C. Olson, S.E. Shaheen, N. Kopidakis, D.S. Ginley, Inverted bulk-heterojunction organic photovoltaic device using a solution-derived ZnO underlayer, Applied Physics Letters. 89 (2006) 143517–1–143517–3.

[24] H. Oh, J. Krantz, I. Litzov, T. Stubhan, L. Pinna, C.J. Brabec, Comparison of various sol–gel derived metal oxide layers for inverted organic solar cells, Solar Energy Materials and Solar Cells. 95 (2011) 2194–2199.

[25] C.J. Brabec, S.E. Shaheen, C. Winder, N.S. Sariciftci, P. Denk, Effect of LiF/metal electrodes on the performance of plastic solar cells, Applied Physics Letters. 80 (2002) 1288–1290.

[26] Y. Şahin, S. Alem, R. de Bettignies, J.-M. Nunzi, Development of air stable polymer solar cells using an inverted gold on top anode structure, Thin Solid Films. 476 (2005) 340–343.

[27] S.K. Hau, H.-L. Yip, N.S. Baek, J. Zou, K. O'Malley, A.K.-Y. Jen, Air-stable inverted flexible polymer solar cells using zinc oxide nanoparticles as an electron selective layer, Applied Physics Letters. 92 (2008) 253301–1–253301–3.

[28] F. Zhang, X. Xu, W. Tang, J. Zhang, Z. Zhuo, J. Wang,J. Wang, Z. Xu, Y. Wang, Recent development of the inverted configuration organic solar cells, Solar Energy Materials and Solar Cells. 95 (2011) 1785–1799.

[29] B.R. Saunders, M.L. Turner, Nanoparticle-polymer photovoltaic cells, Advances in Colloid and Interface Science. 138 (2008) 1–23.

[30] T. Stübinger, W. Brütting, Exciton diffusion and optical interference in organic donor–acceptor photovoltaic cells, Journal of Applied Physics. 90 (2001) 3632–3641.

[31] J.D. Servaites, M.A. Ratner, T.J. Marks, Organic solar cells: A new look at traditional models, Energy & Environmental Science. 4 (2011) 4410–4422.

[32] T.M. Clarke, J.R. Durrant, Charge photogeneration in organic solar cells, Chemical Reviews. 110 (2010) 6736–6767.

[33] A.C. Mayer, S.R. Scully, B.E. Hardin, M.W. Rowell, M.D. McGehee, Polymer-based solar cells, Materials Today. 10 (2007) 28–33.

[34] T. Xu, Q. Qiao, Conjugated polymer–inorganic semiconductor hybrid solar cells, Energy & Environmental Science. 4 (2011) 2700–2720.

[35] M.T. Dang, L. Hirsch, G. Wantz, P3HT:PCBM, best seller in polymer photovoltaic research, Advanced Materials. 23 (2011) 3597–3602.

[36] S.R. Forrest, The limits to organic photovoltaic cell efficiency, MRS Bulletin. 30 (2005) 28–32.

[37] M.C. Scharber, D. Mühlbacher, M. Koppe, P. Denk, C. Waldauf, A.J. Heeger, C.J. Brabec, Design rules for donors in bulk-heterojunction solar cells - towards 10% energy-conversion efficiency, Advanced Materials. 18 (2006) 789–794.

[38] A. Moliton, J.-M. Nunzi, How to model the behaviour of organic photovoltaic cells, Polymer International. 55 (2006) 583–600.

[39] J.D. Servaites, S. Yeganeh, T.J. Marks, M.A. Ratner, Efficiency enhancement in organic photovoltaic cells: consequences of optimizing series resistance, Advanced Functional Materials. 20 (2010) 97–104.

[40] N.S. Sariciftci, L. Smilowitz, A.J. Heeger, F. Wudl, Photoinduced electron transfer polymer to buckminsterfullerene, Science. 258 (1992) 1474–1476.

[41] C. Yang, Y. Li, J. Hou, C. He, Z. Tan, B. Fan, Y. Zhou, Q. Sun, Y. Li, Y. Li, S. Zhu, Thinner-film plastic photovoltaic cells based on different C60 derivatives, Polymers for Advanced Technologies. 17 (2006) 500–505.

[42] C.J. Brabec, S. Gowrisanker, J.J.M. Halls, D. Laird, S. Jia, S.P. Williams, Polymer-fullerene bulk-heterojunction solar cells, Advanced Materials. 22 (2010) 3839–3856.

[43] J.-H. Huang, C.-P. Lee, Z.-Y. Ho, D. Kekuda, C.-W. Chu, K.-C. Ho, Enhanced spectral response in polymer bulk heterojunction solar cells by using active materials with complementary spectra, Solar Energy Materials and Solar Cells. 94 (2010) 22–28.

[44] F.B. Kooistra, J. Knol, F. Kastenberg, L.M. Popescu, W.J.H. Verhees, J.M. Kroon, J.C. Hummelen, Increasing the open circuit voltage of bulk-heterojunction solar cells by raising the LUMO level of the acceptor, Organic Letters. 9 (2007) 551–554.

[45] A.J. Moulé, K. Meerholz, Morphology control in solution-processed bulk-heterojunction solar cell mixtures, Advanced Functional Materials. 19 (2009) 3028–3036.

[46] J. Peet, M.L. Senatore, A.J. Heeger, G.C. Bazan, The role of processing in the fabrication and optimization of plastic solar cells, Advanced Materials. 21 (2009) 1521–1527.

[47] V.D. Mihailetchi, J.K.J. van Duren, P.W.M. Blom, J.C. Hummelen, R.A.J. Janssen, J.M. Kroon, M.T. Rispens, W.J.J. Verhees, M.M. Wienk, Electron transport in a methanofullerene, Advanced Functional Materials. 13 (2003) 43–46.

[48] D.W. Sievers, V. Shrotriya, Y. Yang, Modeling optical effects and thickness dependent current in polymer bulk-heterojunction solar cells, Journal of Applied Physics. 100 (2006) 114509–1–114509–7.

[49] J.K. Park, C. Kim, B. Walker, T.Q. Nguyen, J.H. Seo, Morphology control of solution processable small molecule bulk heterojunction solar cells via solvent additives, RSC Advances. 2 (2012) 2232–2234.

[50] J. Peet, A.B. Tamayo, X.-D. Dang, J.H. Seo, T.-Q. Nguyen, Small molecule sensitizers for near-infrared absorption in polymer bulk heterojunction solar cells, Applied Physics Letters. 93 (2008) 163306.

[51] E. Bundgaard, F. Krebs, Low band gap polymers for organic photovoltaics, Solar Energy Materials and Solar Cells. 91 (2007) 954–985.

[52] Y.J. Cheng, S.H. Yang, C.S. Hsu, Synthesis of conjugated polymers for organic solar cell applications, Chemical Reviews. 109 (2009) 5868–923.

[53] L. Biniek, B.C. Schroeder, C.B. Nielsen, I. McCulloch, Recent advances in high mobility donor–acceptor semiconducting polymers, Journal of Materials Chemistry. 22 (2012) 14803–14813.

[54] E.E. Havinga, W. ten Hoeve, H. Wynberg, Alternate donor-acceptor small-band-gap semiconducting polymers; polysquaraines and polycroconaines, Synthetic Metals. 55-57 (1993) 299–306.

[55] S.P. Mishra, A.K. Palai, M. Patri, Synthesis and characterization of soluble narrow band gap conducting polymers based on diketopyrrolopyrrole and propylenedioxythiophenes, Synthetic Metals. 160 (2010) 2422–2429.

[56] A.B. Tamayo, B. Walker, T.Q. Nguyen, A low band gap, solution processable oligothiophene with a diketopyrrolopyrrole core for use in organic solar cells, The Journal of Physical Chemistry C. 112 (2008) 11545–11551.

[57] X. Wang, H. Luo, Y. Sun, M. Zhang, X. Li, G. Yu, Y. Liu, Y. Li, H. Wang, Narrow band gap D-A copolymer of indacenodithiophene and diketopyrrolopyrrole with deep HOMO level: Synthesis and application in field-effect transistors and polymer solar cells, Journal of Polymer Science Part A: Polymer Chemistry. 50 (2011) 371–377.

[58] L. Zhang, K. Tajima, K. Hashimoto, Low bandgap polymers based on regioregular oligothiophenes linked with electron accepting units, Macromolecules. 44 (2011) 4222–4229.

[59] S.H. Park, A. Roy, S. Beaupré, S. Cho, N. Coates, J.S. Moon, D. Moses, M. Leclerc, K. Lee, A.J. Heeger, Bulk heterojunction solar cells with internal quantum efficiency approaching 100%, Nature Photonics. 3 (2009) 297–303.

[60] H. Zhou, L. Yang, A.C. Stuart, S.C. Price, S. Liu, W. You, Development of fluorinated benzothiadiazole as a structural unit for a polymer solar cell of 7% efficiency, Angewandte Chemie. 123 (2011) 3051–3054.

[61] E. Wang, L. Hou, Z. Wang, S. Hellström, F. Zhang, O. Inganäs, M.R. Andersson, An easily synthesized blue polymer for high-performance polymer solar cells, Advanced Materials. 22 (2010) 5240–5244.

[62] Y.-C. Chen, C.-Y. Yu, Y.-L. Fan, L.-I. Hung, C.-P. Chen, C. Ting, Low-bandgap conjugated polymer for high efficient photovoltaic applications, Chemical Communications. 46 (2010) 6503–6505.

[63] W.-H. Lee, S.K. Son, K. Kim, S.K. Lee, W.S. Shin, S.-J. Moon, I.-N. Kang, Synthesis and characterization of new selenophene-based donor-acceptor low-bandgap polymers for organic photovoltaic cells, Macromolecules. 45 (2012) 1303–1312.

[64] J. Li, K.-H. Ong, S.-L. Lim, G.-M. Ng, H.-S. Tan, Z.-K. Chen, A random copolymer based on dithienothiophene and diketopyrrolopyrrole units for high performance organic solar cells., Chemical Communications. 47 (2011) 9480–9482.

[65] W. Li, T. Lee, S.J. Oh, C.R. Kagan, Diketopyrrolopyrrole-based π-bridged donor-acceptor polymer for photovoltaic applications, ACS Applied Materials & Interfaces. 3 (2011) 3874–3883.

[66] B. Lim, J.-S. Yeo, D. Khim, D.-Y. Kim, Synthesis and photovoltaic properties of a thienylenevinylene and diketopyrrolopyrrole copolymer with high mobility, Macromolecular Rapid Communications. 32 (2011) 1551–1556.

[67] P. Sonar, S.P. Singh, Y. Li, Z.-E. Ooi, T. Ha, I. Wong, M.S. Soh, A. Dodabalapur, High mobility organic thin film transistor and efficient photovoltaic devices using versatile donor–acceptor polymer semiconductor by molecular design, Energy & Environmental Science. 4 (2011) 2288–2296.

[68] E. Zhou, S. Yamakawa, K. Tajima, C. Yang, K. Hashimoto, Synthesis and photovoltaic properties of diketopyrrolopyrrole-based donor-acceptor copolymers, Chemistry of Materials. 21 (2009) 4055–4061.

[69] Y. Zhu, R.D. Champion, S.A. Jenekhe, Conjugated donor-acceptor copolymer semiconductors with large intramolecular charge transfer: Synthesis, optical properties, electrochemistry, and field effect carrier mobility of thienopyrazine-based copolymers, Macromolecules. 39 (2006) 8712–8719.

[70] M. Sommer, S. Hüttner, U. Steiner, M. Thelakkat, Influence of molecular weight on the solar cell performance of double-crystalline donor-acceptor block copolymers, Applied Physics Letters. 95 (2009) 183308–1–183308–3.

[71] Y. Li, P. Sonar, S.P. Singh, Z.E. Ooi, E.S.H. Lek, M.Q.Y. Loh, Poly(2,5-bis(2-octyldodecyl)-3,6-di(furan-2-yl)-2,5-dihydro-pyrrolo[3,4-c]pyrrole-1,4-dione-co-thieno[3,2-b]thiophene): A high performance polymer semiconductor for both organic thin film transistors and organic photovoltaics, Physical Chemistry Chemical Physics. 14 (2012) 7162–7169.

[72] J. Chen, Y. Cao, Development of novel conjugated donor polymers for high-efficiency bulk-heterojunction photovoltaic devices, Accounts of Chemical Research. 42 (2009) 1709–1718.

[73] J.L. Brédas, J.E. Norton, J. Cornil, V. Coropceanu, Molecular understanding of organic solar cells: The challenges, Accounts of Chemical Research. 42 (2009) 1691–1699.

[74] H. Chen, J. Hou, S. Zhang, Y. Liang, G. Yang, Y. Yang, Polymer solar cells with enhanced open-circuit voltage and efficiency, Nature Photonics. 3 (2009) 649–653.

[75] Y. Li, S.P. Singh, P. Sonar, A high mobility p-type DPP-thieno[3,2-b]thiophene copolymer for organic thin-film transistors, Advanced Materials. 22 (2010) 4862–4866.

[76] Y. Li, P. Sonar, S.P. Singh, M.S. Soh, M. van Meurs, J. Tan, Annealing-free high-mobility diketopyrrolopyrrole-quaterthiophene copolymer for solution-processed organic thin film transistors, Journal of the American Chemical Society. 133 (2011) 2198–2204.

[77] Y. Wu, Y. Li, S. Gardner, B.S. Ong, Indolo[3,2-b]carbazole-based thin-film transistors with high mobility and stability, Journal of the American Chemical Society. 127 (2005) 614–618.

[78] H. Pan, Y. Li, Y. Wu, P. Liu, B.S. Ong, S. Zhu, G. Xu, Low-temperature, solution-processed, high-mobility polymer semiconductors for thin-film transistors, Journal of the American Chemical Society. 129 (2007) 4112–4113.

[79] P. Schilinsky, U. Asawapirom, U. Scherf, M. Biele, C.J. Brabec, Influence of the molecular weight of poly(3-hexylthiophene) on the performance of bulk heterojunction solar cells, Chemistry of Materials. 17 (2005) 2175–2180.

[80] O. Wallquist, 20 years of DPP Pigments - Future perspectives, Macromolecular Symposia. 187 (2002) 617–629.

[81] S. Qu, H. Tian, Diketopyrrolopyrrole (DPP)-based materials for organic photovoltaics, Chemical Communications. 48 (2012) 3039–3051.

[82] B. Tieke, A.R. Rabindranath, K. Zhang, Y. Zhu, Conjugated polymers containing diketopyrrolopyrrole units in the main chain, Beilstein Journal of Organic Chemistry. 6 (2010) 830–845.

[83] Y. Li, P. Sonar, L. Murphy, W. Hong, High mobility diketopyrrolopyrrole (DPP)-based organic semiconductor materials for organic thin film transistors and photovoltaics, Energy & Environmental Science. (2013) DOI: 10.1039/C3EE00015J.

[84] J.W. Jung, F. Liu, T.P. Russell, W.H. Jo, A high mobility conjugated polymer based on dithienothiophene and diketopyrrolopyrrole for organic photovoltaics, Energy & Environmental Science. 5 (2012) 6857–6861.

[85] F. Liu, Y. Gu, C. Wang, W. Zhao, D. Chen, A.L. Briseno,T.P. Russell, Efficient polymer solar cells based on a low bandgap semi-crystalline DPP polymer-PCBM blends, Advanced Materials. 24 (2012) 3947–3951.

[86] J.C. Bijleveld, V.S. Gevaerts, D. Di Nuzzo, M. Turbiez, S.G.J. Mathijssen, D.M. de Leeuw, M.M. Wienk, R.A.J. Janssen, Efficient solar cells based on an easily accessible diketopyrrolopyrrole polymer, Advanced Materials. 22 (2010) E242–E246.

[87] W. Li, W.S.C. Roelofs, M.M. Wienk, R.A.J. Janssen, Enhancing the photocurrent in diketopyrrolopyrrole-based polymer solar cells via energy level control, Journal of the American Chemical Society. 134 (2012) 13787–13795.

[88] M. Shahid, R.S. Ashraf, Z. Huang, A.J. Kronemeijer, T. McCarthy-Ward, I. McCulloch, J.R. Durrant, H. Sirringhaus, M. Heeney, Photovoltaic and field effect transistor performance of selenophene and thiophene diketopyrrolopyrrole co-polymers with dithienothiophene, Journal of Materials Chemistry. 22 (2012) 12817–12823.

[89] C. Goh, R.J. Kline, M.D. McGehee, E.N. Kadnikova, J.M.J. Fréchet, Molecular-weight-dependent mobilities in regioregular poly(3-hexyl-thiophene) diodes, Applied Physics Letters. 86 (2005) 122110–1–122110–3.

[90] A. Kumar, H.-H. Liao, Y. Yang, Hole mobility in optimized organic photovoltaic blend films obtained using extraction current transients, Organic Electronics. 10 (2009) 1615–1620.

[91] V.D. Mihailetchi, J. Wildeman, P.W.M. Blom, Space-charge limited photocurrent, Physical Review Letters. 94 (2005) 1–4.

[92] C. Tanase, E.J. Meijer, P.W.M. Blom, D.M. de Leeuw, Unification of the Hole Transport in Polymeric Field-Effect Transistors and Light-Emitting Diodes, Physical Review Letters. 91 (2003) 1–4.

[93] E. von Hauff, J. Parisi, V. Dyakonov, Field effect measurements on charge carrier mobilities in various polymer-fullerene blend compositions, Thin Solid Films. 511-512 (2006) 506–511.

[94] J. Nakamura, K. Murata, K. Takahashi, Relation between carrier mobility and cell performance in bulk heterojunction solar cells consisting of soluble polythiophene and fullerene derivatives, Applied Physics Letters. 87 (2005) 132105–1–132105–3.

[95] V.D. Mihailetchi, H. Xie, B. de Boer, L.M. Popescu, J.C. Hummelen, P.W.M. Blom, L.J.A. Koster, Origin of the enhanced performance in poly(3-hexylthiophene): [6,6]-phenyl C61-butyric acid methyl ester solar cells upon slow drying of the active layer, Applied Physics Letters. 89 (2006) 012107–1–012107–3.

[96] L.J.A. Koster, V.D. Mihailetchi, H. Xie, P.W.M. Blom, Origin of the light intensity dependence of the short-circuit current of polymer/fullerene solar cells, Applied Physics Letters. 87 (2005) 203502–1–203502–3.

[97] L.J.A. Koster, V.D. Mihailetchi, P.W.M. Blom, Ultimate efficiency of polymer/fullerene bulk heterojunction solar cells, Applied Physics Letters. 88 (2006) 093511–1–093511–3.

[98] P. Peumans, S.R. Forrest, Separation of geminate charge-pairs at donor–acceptor interfaces in disordered solids, Chemical Physics Letters. 398 (2004) 27–31.

[99] J.D. Kotlarski, D.J.D. Moet, P.W.M. Blom, Role of balanced charge carrier transport in low band gap polymer:fullerene bulk heterojunction solar cells, Journal of Polymer Science Part B: Polymer Physics. 49 (2011) 708–711.

[100] Y. Li, P. Sonar, S.P. Singh, W. Zeng, M.S. Soh, 3,6-Di(furan-2-yl)pyrrolo[3,4-c]pyrrole-1,4(2H,5H)-dione and bithiophene copolymer with rather disordered chain orientation showing high mobility in organic thin film transistors, Journal of Materials Chemistry. 21 (2011) 10829–10835.

[101] B. Amrouche, A. Guessoum, M. Belhamel, A simple behavioural model for solar module electric characteristics based on the first order system step response for MPPT study and comparison, Applied Energy. 91 (2012) 395–404.

[102] C. Kanimozhi, P. Balraju, G.D. Sharma, S. Patil, Synthesis of diketopyrrolopyrrole containing copolymers: a study of their optical and photovoltaic properties, The Journal of Physical Chemistry B. 114 (2010) 3095–3103.

[103] G. Ren, P.-T. Wu, S.A. Jenekhe, Enhanced performance of bulk heterojunction solar cells using block copoly(3-alkylthiophene)s, Chemistry of Materials. 22 (2010) 2020–2026.

[104] P.N. Murgatroyd, Theory of space-charge-limited current enhanced by Frenkel effect, Journal of Physics D: Applied Physics. 3 (1970) 151–156.

[105] V.D. Mihailetchi, H. Xie, B. de Boer, L.J.A. Koster, P.W.M. Blom, Charge transport and photocurrent generation in poly(3-hexylthiophene):methanofullerene bulk-heterojunction solar cells, Advanced Functional Materials. 16 (2006) 699–708.

[106] Z.B. Wang, M.G. Helander, M.T. Greiner, J. Qiu, Z.H. Lu, Carrier mobility of organic semiconductors based on current-voltage characteristics, Journal of Applied Physics. 107 (2010) 034506–1–034506–4.

[107] B.S. Jeong, H. Choi, N. Cho, H. Min Ko, W. Lim, K. Song, J.K. Lee, J. Ko, Molecular engineering of diketopyrrolopyrrole-based photosensitizer for solution processed small molecule bulk heterojunction solar cells, Solar Energy Materials and Solar Cells. 95 (2011) 1731–1740.

[108] V. Shrotriya, Y. Yao, G. Li, Y. Yang, Effect of self-organization in polymer/fullerene bulk heterojunctions on solar cell performance, Applied Physics Letters. 89 (2006) 063505–1–063505–3.

[109] A.W. Bott, Practical problems in voltammetry 3: Reference electrodes for voltammetry, Current Separations. 14 (1995) 64–68.

[110] R.R. Gagne, C.A. Koval, G.C. Lisensky, Ferrocene as an internal standard for electrochemical measurements, Inorganic Chemistry. 19 (1980) 2854–2855.

[111] A.M. Bond, K.B. Oldham, G.A. Snook, Use of the ferrocene oxidation process to provide both reference electrode potential calibration and a simple measurement (via semiintegration) of the uncompensated resistance in cyclic voltammetric studies in high-resistance organic solvents, Analytical Chemistry. 72 (2000) 3492–3496.

[112] C.H. Woo, P.M. Beaujuge, T.W. Holcombe, O.P. Lee, J.M.J. Fréchet, Incorporation of furan into low band-gap polymers for efficient solar cells., Journal of the American Chemical Society. 132 (2010) 15547–15549.

[113] J.C. Bijleveld, B.P. Karsten, S.G.J. Mathijssen, M.M. Wienk, D.M. de Leeuw, R.A.J. Janssen, Small band gap copolymers based on furan and diketopyrrolopyrrole for field-effect transistors and photovoltaic cells, Journal of Materials Chemistry. 21 (2011) 1600–1606.

[114] E. Ripaud, D. Demeter, T. Rousseau, E. Boucard-Cétol, M. Allain, R. Po, P. Leriche, J. Roncali, Structure–properties relationships in conjugated molecules based on diketopyrrolopyrrole for organic photovoltaics, Dyes and Pigments. 95 (2012) 126–133.

[115] P. Sonar, S.P. Singh, E.L. Williams, Y. Li, M.S. Soh, A. Dodabalapur, Furan containing diketopyrrolopyrrole copolymers: synthesis, characterization, organic field effect transistor performance and photovoltaic properties, Journal of Materials Chemistry. 22 (2012) 4425–4435.

[116] A.T. Yiu, P.M. Beaujuge, O.P. Lee, C.H. Woo, M.F. Toney, J.M.J. Fréchet, Side-chain tunability of furan-containing low band-gap polymers provides control of structural order in efficient solar cells, Journal of the American Chemical Society. 134 (2012) 2180–2185.

[117] L.M. Andersson, C. Müller, B.H. Badada, F. Zhang, U. Würfel, O. Inganäs, Mobility and fill factor correlation in geminate recombination limited solar cells, Journal of Applied Physics. 110 (2011) 024509–1–024509–7.

[118] V. Shrotriya, G. Li, Y. Yao, C.-W. Chu, Y. Yang, Transition metal oxides as the buffer layer for polymer photovoltaic cells, Applied Physics Letters. 88 (2006) 073508–1–073508–3.

[119] T. Kuwabara, Y. Kawahara, T. Yamaguchi, K. Takahashi, Characterization of inverted-type organic solar cells with a ZnO layer as the electron collection electrode by ac impedance spectroscopy, ACS Applied Materials & Interfaces. 1 (2009) 2107–2110.

[120] G. Zhang, Y. Fu, Z. Xie, Q. Zhang, Synthesis of low bandgap polymer based on 3,6-dithien-2-yl-2,5-dialkylpyrrolo[3,4-c]pyrrole-1,4-dione for photovoltaic applications, Solar Energy Materials and Solar Cells. 95 (2011) 1168–1173.

[121] G. Dennler, M.C. Scharber, C.J. Brabec, Polymer-fullerene bulk-heterojunction solar cells, Advanced Materials. 21 (2009) 1323–1338.

[122] C.J. Brabec, J.R. Durrant, Solution-processed organic solar cells, MRS Bulletin. 33 (2008) 670–675.

[123] S.-H. Lee, D.-H. Kim, J.-H. Kim, G.-S. Lee, J.-G. Park, Effect of metal-reflection and surface-roughness properties on power-conversion efficiency for polymer photovoltaic cells, The Journal of Physical Chemistry C. 113 (2009) 21915–21920.

[124] S.-H. Lee, J.-H. Kim, T.-H. Shim, J.-G. Park, Effect of interface thickness on power conversion efficiency of polymer photovoltaic cells, Electronic Materials Letters. 5 (2009) 47–50.

[125] R.C. Hiorns, R. de Bettignies, J. Leroy, S. Bailly, M. Firon, C. Sentein, A. Khoukh, H. Preud'homme, C. Dagron-Lartigau, High molecular weights, polydispersities, and annealing temperatures in the optimization of bulk-heterojunction photovoltaic cells based on poly(3-hexylthiophene) or poly(3-butylthiophene), Advanced Functional Materials. 16 (2006) 2263–2273.

[126] W. Ma, J.Y. Kim, K. Lee, A.J. Heeger, Effect of the molecular weight of poly(3-hexylthiophene) on the morphology and performance of polymer bulk heterojunction solar cells, Macromolecular Rapid Communications. 28 (2007) 1776–1780.

[127] C. Nicolet, D. Deribew, C. Renaud, G. Fleury, C. Brochon, E. Cloutet, L. Vignau, G. Wantz, H. Cramail, M. Geoghegan, G. Hadziioannou, Optimization of the bulk heterojunction composition for enhanced photovoltaic properties: correlation between the molecular weight of the semiconducting polymer and device performance., The Journal of Physical Chemistry B. 115 (2011) 12717–12727.

[128] Y. Xie, P. Dutta, D. Cengher, V. Bommisetty, J. Li, D. Galipeau, Q. Qiao, Solvent effect on the morphology of P3HT/PCBM films, Proceedings of SPIE. 7416 (2009) 74161Q1–8.

[129] D.E. Motaung, G.F. Malgas, C.J. Arendse, Comparative study: The effects of solvent on the morphology, optical and structural features of regioregular poly(3-hexylthiophene):fullerene thin films, Synthetic Metals. 160 (2010) 876–882.

[130] M.T. Dang, G. Wantz, H. Bejbouji, M. Urien, O.J. Dautel, L. Vignau, L. Hirsch, Polymeric solar cells based on P3HT:PCBM: Role of the casting solvent, Solar Energy Materials and Solar Cells. 95 (2011) 3408–3418.

[131] R.B. Aïch, Y. Zou, M. Leclerc, Y. Tao, Solvent effect and device optimization of diketopyrrolopyrrole and carbazole copolymer based solar cells, Organic Electronics. 11 (2010) 1053–1058.

[132] G. Li, V. Shrotriya, J. Huang, Y. Yao, T. Moriarty, K. Emery, Y. Yang, High-efficiency solution processable polymer photovoltaic cells by self-organization of polymer blends, Nature Materials. 4 (2005) 864–868.

[133] Y.-S. Tsai, W.-P. Chu, F.-S. Juang, R.-M. Tang, M.-H. Chang, T.-E. Hsieh, M.O. Liu, Efficiency improvement of organic solar cells by slow growth and changing spin-coating parameters for active layers, Japanese Journal of Applied Physics. 50 (2011) 022301–1–022301–4.

[134] P. Dutta, Y. Xie, M. Kumar, M. Rathi, P. Ahrenkiel, D. Galipeau, Q. Qiao, V. Bommisetty, Connecting physical properties of spin-casting solvents with morphology, nanoscale charge transport, and device performance of poly(3-hexylthiophene):phenyl-C61-butyric acid methyl ester bulk heterojunction solar cells, Journal of Photonics for Energy. 1 (2011) 011124.

[135] P.P. Boix, M.M. Wienk, R.A.J. Janssen, G. Garcia-Belmonte, Open-circuit voltage limitation in low bandgap diketopyrrolopyrrole-based polymer solar cells processed from different solvents, The Journal of Physical Chemistry C. 115 (2011) 15075–15080.

[136] M.M. Wienk, M.G.R. Turbiez, J. Gilot, R.A.J. Janssen, Narrow-bandgap diketo-pyrrolo-pyrrole polymer solar cells: The effect of processing on the performance, Advanced Materials. 20 (2008) 2556–2560.

[137] L. Bürgi, M.G.R. Turbiez, R. Pfeiffer, F. Bienewald, H.J. Kirner, C. Winnewisser, High-mobility ambipolar near-infrared light-emitting polymer field-effect transistors, Advanced Materials. 20 (2008) 2217–2224.

[138] E. Zhou, Q. Wei, S. Yamakawa, Y. Zhang, K. Tajima, C. Yang, K. Hashimoto, Diketopyrrolopyrrole-based semiconducting polymer for photovoltaic device with photocurrent response wavelengths up to 1.1 μm, Macromolecules. 43 (2010) 821–826.

[139] J. Peet, J.Y. Kim, N.E. Coates, W.L. Ma, D. Moses, A.J. Heeger, G.C. Bazan, Efficiency enhancement in low-bandgap polymer solar cells by processing with alkane dithiols, Nature Materials. 6 (2007) 497–500.

[140] C. V. Hoven, X.-D. Dang, R.C. Coffin, J. Peet, T.-Q. Nguyen, G.C. Bazan, Improved performance of polymer bulk heterojunction solar cells through the reduction of phase separation via solvent additives, Advanced Materials. 22 (2010) E63–E66.

[141] D. Di Nuzzo, A. Aguirre, M. Shahid, V.S. Gevaerts, S.C.J. Meskers, R.A.J. Janssen, Improved film morphology reduces charge carrier recombination into the triplet excited state in a small bandgap polymer-fullerene photovoltaic cell., Advanced Materials. 22 (2010) 4321–4324.

[142] C.S. Kim, L.L. Tinker, B.F. DiSalle, E.D. Gomez, S. Lee, S. Bernhard, Y.-L. Loo, Altering the thermodynamics of phase separation in inverted bulk-heterojunction organic solar cells, Advanced Materials. 21 (2009) 3110–3115.

[143] J. Jo, D. Gendron, A. Najari, J.S. Moon, S. Cho, M. Leclerc, A.J. Heeger, Bulk heterojunction solar cells based on a low-bandgap carbazole-diketopyrrolopyrrole copolymer, Applied Physics Letters. 97 (2010) 203303–1–203303–3.

[144] K. Kim, J. Liu, M.A.G. Namboothiry, D.L. Carroll, Roles of donor and acceptor nanodomains in 6% efficient thermally annealed polymer photovoltaics, Applied Physics Letters. 90 (2007) 163511–1–163511–3.

[145] Y. Liang, Z. Xu, J. Xia, S.T. Tsai, Y. Wu, G. Li, C. Ray, L. Yu., For the bright future-bulk heterojunction polymer solar cells with power conversion efficiency of 7.4%, Advanced Materials. 22 (2010) E135–138.

[146] Y. Liang, D. Feng, Y. Wu, S.-T. Tsai, G. Li, C. Ray, L. Yu, Highly efficient solar cell polymers developed via fine-tuning of structural and electronic properties, Journal of the American Chemical Society. 131 (2009) 7792–7799.

[147] G. Ren, E. Ahmed, S.A. Jenekhe, Non-fullerene acceptor-based bulk heterojunction polymer solar cells: engineering the nanomorphology via processing additives, Advanced Energy Materials. 1 (2011) 946–953.

[148] P. Sonar, G.-M. Ng, T.T. Lin, A. Dodabalapur, Z.-K. Chen, Solution processable low bandgap diketopyrrolopyrrole (DPP) based derivatives: novel acceptors for organic solar cells, Journal of Materials Chemistry. 20 (2010) 3626–3636.

[149] G.D. Sharma, P. Suresh, J.A. Mikroyannidis, M.M. Stylianakis, Efficient bulk heterojunction devices based on phenylenevinylene small molecule and perylene–pyrene bisimide, Journal of Materials Chemistry. 20 (2010) 561–567.

[150] C.H. Woo, T.W. Holcombe, D.A. Unruh, A. Sellinger, J.M.J. Fréchet, Phenyl vs alkyl polythiophene: A solar cell comparison using a vinazene derivative as acceptor, Chemistry of Materials. 22 (2010) 1673–1679.

[151] H. Sirringhaus, N. Tessler, R.H. Friend, Integrated optoelectronic devices based on conjugated polymers, Science. 280 (1998) 1741–1744.

[152] A.J. Moulé, J.B. Bonekamp, K. Meerholz, The effect of active layer thickness and composition on the performance of bulk-heterojunction solar cells, Journal of Applied Physics. 100 (2006) 094503–1–094503–7.

[153] J. Alstrup, M. Jørgensen, A.J. Medford, F.C. Krebs, Ultra fast and parsimonious materials screening for polymer solar cells using differentially pumped slot-die coating, ACS Applied Materials & Interfaces. 2 (2010) 2819–2827.

[154] L. Zeng, C.W. Tang, S.H. Chen, Effects of active layer thickness and thermal annealing on polythiophene:fullerene bulk heterojunction photovoltaic devices, Applied Physics Letters. 97 (2010) 053305–1–053305–3.

[155] J. Peet, L. Wen, P. Byrne, S. Rodman, K. Forberich, Y. Shao, N. Drolet, R. Gaudiana, G. Dennler, D. Waller, Bulk heterojunction solar cells with thick active layers and high fill factors enabled by a bithiophene-co-thiazolothiazole push-pull copolymer, Applied Physics Letters. 98 (2011) 043301–1–043301–3.

[156] P. Heremans, D. Cheyns, B.P. Rand, Strategies for increasing the efficiency of heterojunction organic solar cells: material selection and device architecture, Accounts of Chemical Research. 42 (2009) 1740–1747.

[157] F. Monestier, J.-J. Simon, P. Torchio, L. Escoubas, F. Flory, S. Bailly, R. de Bettignies, S. Guillerez, C. Defranoux, Modeling the short-circuit current density of polymer solar cells based on P3HT:PCBM blend, Solar Energy Materials and Solar Cells. 91 (2007) 405–410.

[158] S.R. Scully, M.D. McGehee, Effects of optical interference and energy transfer on exciton diffusion length measurements in organic semiconductors, Journal of Applied Physics. 100 (2006) 034907–1–034907–5.

[159] J.D. Kotlarski, P.W.M. Blom, Impact of unbalanced charge transport on the efficiency of normal and inverted solar cells, Applied Physics Letters. 100 (2012) 013306–1–013306–3.

[160] C. Waldauf, M. Morana, P. Denk, P. Schilinsky, K. Coakley, S.A. Choulis, C.J. Brabec, Highly efficient inverted organic photovoltaics using solution based titanium oxide as electron selective contact, Applied Physics Letters. 89 (2006) 233517–1–233517–3.

[161] T.J.K. Brenner, I. Hwang, N.C. Greenham, C.R. McNeill, Device physics of inverted all-polymer solar cells, Journal of Applied Physics. 107 (2010) 114501–1–114501–9.

[162] J.H. Park, J.S. Kim, J.H. Lee, W.H. Lee, K. Cho, Effect of annealing solvent solubility on the performance of poly(3-hexylthiophene)/methanofullerene solar cells, Journal of Physical Chemistry C. 113 (2009) 17579–17584.

[163] V.D. Mihailetchi, L.J.A. Koster, P.W.M. Blom, C. Melzer, B. de Boer, J.K.J. van Duren, R.A.J. Janssen, Compositional dependence of the performance of poly(p-phenylene vinylene):methanofullerene bulk-heterojunction solar cells, Advanced Functional Materials. 15 (2005) 795–801.

[164] G. Williams, Q. Wang, H. Aziz, The photo-stability of polymer solar cells: contact photo-degradation and the benefits of interfacial layers, Advanced Functional Materials. (2012) doi: 10.1002/adfm.201202567.

[165] M. Campoy-Quiles, T. Ferenczi, T. Agostinelli, P.G. Etchegoin, Y. Kim, T.D. Anthopoulos, P.N. Stavrinou, D.D.C. Bradley, J. Nelson, Morphology evolution via self-organization and lateral and vertical diffusion in polymer:fullerene solar cell blends, Nature Materials. 7 (2008) 158–164.

[166] Z. Xu, L.-M. Chen, G. Yang, C.-H. Huang, J. Hou, Y. Wu, G. Li, C.-S. Hsu, Y. Yang, Vertical phase separation in poly(3-hexylthiophene):fullerene derivative blends and its advantage for inverted structure solar cells, Advanced Functional Materials. 19 (2009) 1227–1234.

[167] J.-S. Kim, P.K.H. Ho, C.E. Murphy, R.H. Friend, Phase separation in polyfluorene-based conjugated polymer blends: lateral and vertical analysis of blend spin-cast thin films, Macromolecules. 37 (2004) 2861–2871.

[168] A.C. Arias, N. Corcoran, M. Banach, R.H. Friend, J.D. MacKenzie, W.T.S. Huck, Vertically segregated polymer-blend photovoltaic thin-film structures through surface-mediated solution processing, Applied Physics Letters. 80 (2002) 1695–1697.

[169] T.B. Singh, N. Marjanović, P. Stadler, M. Auinger, G.J. Matt, S. Günes, N.S. Sariciftci, R. Schwödiauer, S. Bauer, Fabrication and characterization of solution-processed methanofullerene-based organic field-effect transistors, Journal of Applied Physics. 97 (2005) 083714–1 – 083714–5.

[170] T.D. Anthopoulos, C. Tanase, S. Setayesh, E.J. Meijer, J.C. Hummelen, P.W.M. Blom, D.M. de Leeuw, Ambipolar organic field-effect transistors based on a solution-processed methanofullerene, Advanced Materials. 16 (2004) 2174–2179.

[171] T.D. Anthopoulos, D.M. de Leeuw, E. Cantatore, P. van 't Hof, J. Alma, J.C. Hummelen, Solution processible organic transistors and circuits based on a C70 methanofullerene, Journal of Applied Physics. 98 (2005) 054503–1 – 054503–6.

[172] P.H. Wöbkenberg, D.D.C. Bradley, D. Kronholm, J.C. Hummelen, D.M. de Leeuw, M. Cölle, T.D. Anthopoulos, High mobility n-channel organic field-effect transistors based on soluble C60 and C70 fullerene derivatives, Synthetic Metals. 158 (2008) 468–472.

[173] Y. Yao, C. Shi, G. Li, V. Shrotriya, Q. Pei, Y. Yang, Effects of C70 derivative in low band gap polymer photovoltaic devices: Spectral complementation and morphology optimization, Applied Physics Letters. 89 (2006) 153507.

[174] R.C. Haddon, C70 thin film transistors, Journal of the American Chemical Society. 118 (1996) 3041–3042.

[175] M.M. Wienk, J.M. Kroon, W.J.H. Verjees, J. Knol, J.C. Hummelen, P.A. Van Hal, R.A.J. Janssen, Efficient methano[70]fullerene/MDMO-PPV bulk heterojunction photovoltaic cells, Angewandte Chemie. 42 (2003) 3371–3375.

[176] X. Wang, E. Perzon, F. Oswald, F. Langa, S. Admassie, M.R. Andersson, O. Inganäs, Enhanced photocurrent spectral response in low-bandgap polyfluorene and C70-derivative-based solar cells, Advanced Functional Materials. 15 (2005) 1665–1670.

[177] G.D. Sharma, J.A. Mikroyannidis, S.P. Singh, Efficient bulk heterojunction solar cells based on D–A copolymers as electron donors and PC70BM as electron acceptor, Materials Chemistry and Physics. 135 (2012) 25–31.

[178] E. Verploegen, R. Mondal, C.J. Bettinger, S. Sok, M.F. Toney, Z. Bao, Effects of thermal annealing upon the morphology of polymer-fullerene blends, Advanced Functional Materials. 20 (2010) 3519–3529.

[179] T.M. Clarke, A.M. Ballantyne, J. Nelson, D.D.C. Bradley, J.R. Durrant, Free energy control of charge photogeneration in polythiophene/fullerene solar cells: the influence of thermal annealing on P3HT/PCBM blends, Advanced Functional Materials. 18 (2008) 4029–4035.

[180] R.A. Marsh, J.M. Hodgkiss, S. Albert-Seifried, R.H. Friend, Effect of annealing on P3HT:PCBM charge transfer and nanoscale morphology probed by ultrafast spectroscopy, Nano Letters. 10 (2010) 923–930.

[181] K.M. Coakley, B.S. Srinivasan, J.M. Ziebarth, C. Goh, Y. Liu, M.D. McGehee, Enhanced hole mobility in regioregular polythiophene infiltrated in straight nanopores, Advanced Functional Materials. 15 (2005) 1927–1932.

[182] P.G. Karagiannidis, S. Kassavetis, C. Pitsalidis, S. Logothetidis, Thermal annealing effect on the nanomechanical properties and structure of P3HT:PCBM thin films, Thin Solid Films. 519 (2011) 4105–4109.

[183] R. Hamilton, C.G. Shuttle, B. O'Regan, T.C. Hammant, J. Nelson, J.R. Durrant, Recombination in annealed and nonannealed polythiophene/fullerene solar cells: transient photovoltage studies versus numerical modeling, The Journal of Physical Chemistry Letters. 1 (2010) 1432–1436.

[184] W. Cai, X. Gong, Y. Cao, Polymer solar cells: Recent development and possible routes for improvement in the performance, Solar Energy Materials and Solar Cells. 94 (2010) 114–127.

[185] N.D. Treat, M.A. Brady, G. Smith, M.F. Toney, E.J. Kramer, C.J. Hawker, M.L. Chabinyc, Interdiffusion of PCBM and P3HT reveals miscibility in a photovoltaically active blend, Advanced Energy Materials. 1 (2011) 82–89.

[186] G. Li, V. Shrotriya, Y. Yao, Y. Yang, Investigation of annealing effects and film thickness dependence of polymer solar cells based on poly(3-hexylthiophene), Journal of Applied Physics. 98 (2005) 043704–1–043704–5.

[187] A.B. Tamayo, T. Kent, M. Tantitiwat, M.A. Dante, J. Rogers, T.-Q. Nguyen, Influence of alkyl substituents and thermal annealing on the film morphology and performance of solution processed, diketopyrrolopyrrole-based bulk heterojunction solar cells, Energy & Environmental Science. 2 (2009) 1180–1186.

[188] Y. Kim, S.A. Choulis, J. Nelson, D.D.C. Bradley, S. Cook, J.R. Durrant, Device annealing effect in organic solar cells with blends of regioregular poly(3-hexylthiophene) and soluble fullerene, Applied Physics Letters. 86 (2005) 063502–1–063502–3.

[189] W. Ma, C. Yang, X. Gong, K. Lee, A.J. Heeger, Thermally stable, efficient polymer solar cells with nanoscale control of the interpenetrating network morphology, Advanced Functional Materials. 15 (2005) 1617–1622.

[190] A. Swinnen, I. Haeldermans, M. vande Ven, J. D'Haen, G. Vanhoyland, S. Aresu, M. D'Olieslaeger, J. Manca, Tuning the dimensions of C60-based needlelike crystals in blended thin films, Advanced Functional Materials. 16 (2006) 760–765.

[191] J.M. Warman, M.P. de Haas, T.D. Anthopoulos, D.M. de Leeuw, The negative effect of high-temperature annealing on charge-carrier lifetimes in microcrystalline PCBM, Advanced Materials. 18 (2006) 2294–2298.

[192] P.G. Karagiannidis, D. Georgiou, C. Pitsalidis, A. Laskarakis, S. Logothetidis, Evolution of vertical phase separation in P3HT:PCBM thin films induced by thermal annealing, Materials Chemistry and Physics. 129 (2011) 1207–1213.

[193] J. Jo, S.-S. Kim, S.-I. Na, B.-K. Yu, D.-Y. Kim, Time-dependent morphology evolution by annealing processes on polymer:fullerene blend solar cells, Advanced Functional Materials. 19 (2009) 866–874.

[194] S. Lilliu, T. Agostinelli, E. Pires, M. Hampton, J. Nelson, J.E. Macdonald, Dynamics of crystallization and disorder during annealing of P3HT/PCBM bulk heterojunctions, Macromolecules. 44 (2011) 2725–2734.

[195] B. Conings, S. Bertho, K. Vandewal, A. Senes, J. D'Haen, J. Manca, R.A.J. Janssen, Modeling the temperature induced degradation kinetics of the short circuit current in organic bulk heterojunction solar cells, Applied Physics Letters. 96 (2010) 163301–1–163301–3.

[196] Y. Zhang, H.-L. Yip, O. Acton, S.K. Hau, F. Huang, A.K.-Y. Jen, A simple and effective way of achieving highly efficient and thermally stable bulk-heterojunction polymer solar cells using amorphous fullerene derivatives as electron acceptor, Chemistry of Materials. 21 (2009) 2598–2600.

[197] K. Maturova, S.S. van Bavel, M.M. Wienk, R.A.J. Janssen, M. Kemerink, Morphological device model for organic bulk heterojunction solar cells, Nano Letters. 9 (2009) 3032–3037.

[198] S. Dongaonkar, J.D. Servaites, G.M. Ford, S. Loser, J. Moore, R.M. Gelfand, H. Mohseni, H.W. Hillhouse, R. Agrawal, M.A. Ratner, T.J. Marks, M.S. Lundstrom, M. A. Alam, Universality of non-Ohmic shunt leakage in thin-film solar cells, Journal of Applied Physics. 108 (2010) 124509–1–124509–10.

[199] A.J. Parnell, A.D.F. Dunbar, A.J. Pearson, P.A. Staniec, A.J.C. Dennison, H. Hamamatsu, M.W.A. Skoda, D.G. Lidzey, R.A.L. Jones, Depletion of PCBM at the cathode interface in P3HT/PCBM thin films as quantified via neutron reflectivity measurements, Advanced Materials. 22 (2010) 2444–2447.

[200] M.-F. Falzon, A.P. Zoombelt, M.M. Wienk, R.A.J. Janssen, Diketopyrrolopyrrole-based acceptor polymers for photovoltaic application, Physical Chemistry Chemical Physics. 13 (2011) 8931–8939.

[201] B.P. Karsten, J.C. Bijleveld, R.A.J. Janssen, Diketopyrrolopyrroles as acceptor materials in organic photovoltaics, Macromolecular Rapid Communications. 31 (2010) 1554–1559.

[202] F. Li, Y. Du, Y. Chen, L. Chen, J. Zhao, P. Wang, Direct application of P3HT-DOPO@ZnO nanocomposites in hybrid bulk heterojunction solar cells via grafting P3HT onto ZnO nanoparticles, Solar Energy Materials and Solar Cells. 97 (2011) 64–70.

[203] J. Chandrasekaran, D. Nithyaprakash, K.B. Ajjan, S. Maruthamuthu, D. Manoharan, S. Kumar, Hybrid solar cell based on blending of organic and inorganic materials - An overview, Renewable and Sustainable Energy Reviews. 15 (2011) 1228–1238.

[204] M. Wright, A. Uddin, Organic-inorganic hybrid solar cells: A comparative review, Solar Energy Materials and Solar Cells. 107 (2012) 87–111.

# Appendix A.
# Additional Tables & Figures

**Table A1-1.** Active layer thicknesses of hole-only and electron-only devices of various D/A ratios, annealed at various temperatures.

| | | Annealing Temperature | | | | |
|---|---|---|---|---|---|---|
| **Type** | **D/A Ratio** | **25°C** | **60°C** | **100°C** | **150°C** | **200°C** |
| $h^+$-only | 1/1 | 233 nm | 263 nm | 253 nm | 230 nm | 509 nm |
| | 1/2 | 354 nm | 226 nm | 364 nm | 199 nm | 331 nm |
| | 1/3 | 234 nm | - | 261 nm | 256 nm | 514 nm |
| | 1/4 | 276 nm | 267 nm | 247 nm | 269 nm | 266 nm |
| $e^-$-only | 1/3 | 198 nm | - | 153 nm | 197 nm | 272 nm |
| | 1/4 | 213 nm | - | 184 nm | 187 nm | 179 nm |

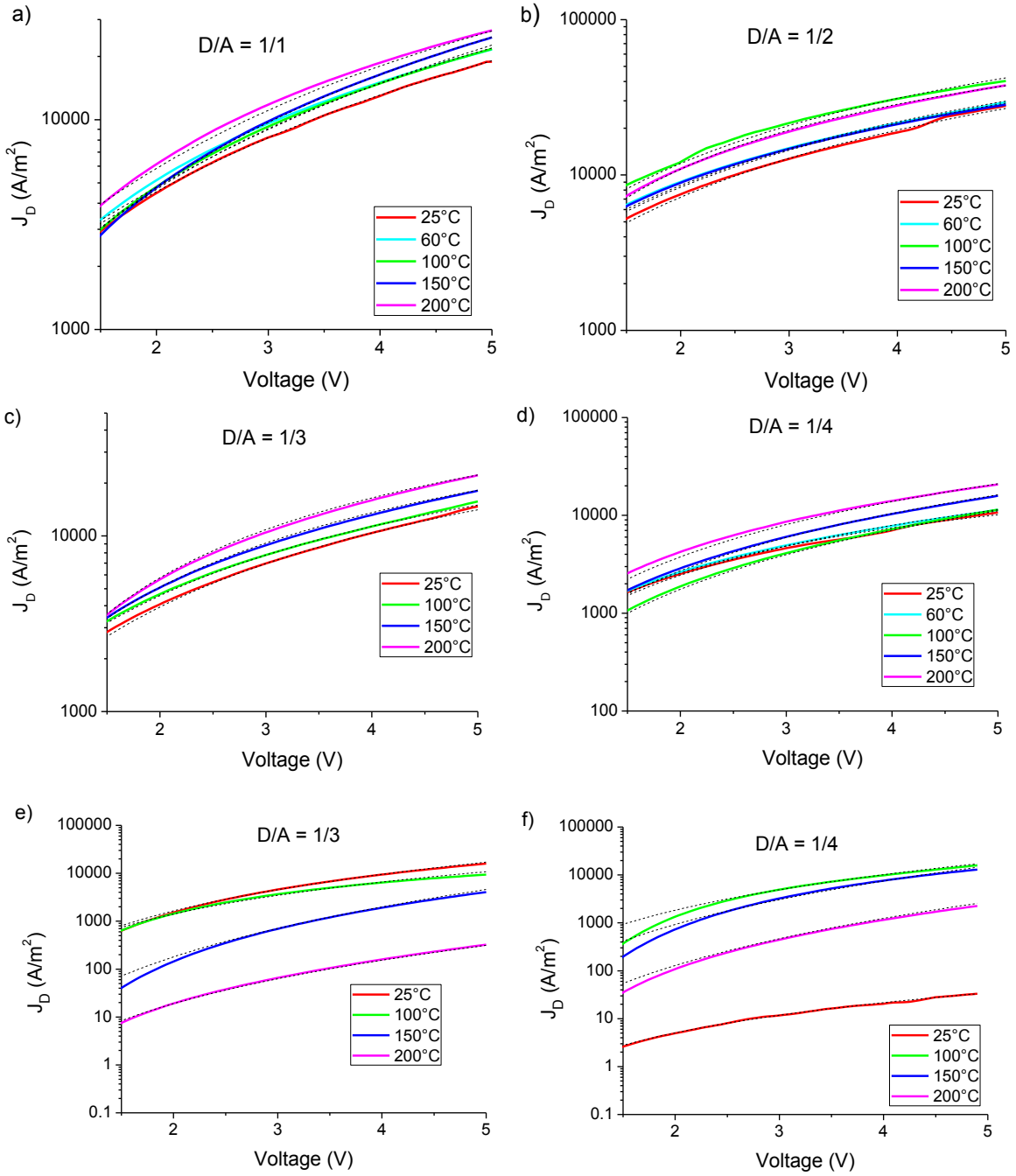


**Figure A1-1.** *J-V* characteristics in the dark of PDBFBT:$PC_{61}BM$ films of hole-only devices with D/A ratios of a) 1/1, b) 1/2, c) 1/3, and d) 1/4 and electron-only devices with D/A ratios of e) 1/3, and f) 1/4 annealed at various temperatures, with fittings from the Mott-Gurney equation (black, dotted lines).

# Appendix B.
# Scientific Contributions

The following peer-reviewed publication is based on aspects of the work contained in this thesis:

- **L. Murphy**, W. Hong, H. Aziz, and Y. Li, Organic photovoltaics with thick active layers (~800nm) using a high mobility polymer donor, Solar Energy Materials and Solar Cells, 114 (2013) 71–81.

Other peer-reviewed publications:

- Y. Li, P. Sonar, **L. Murphy**, and W. Hong, High mobility diketopyrrolopyrrole (DPP)-based organic semiconductor materials for organic thin film transistors and photovoltaics, Energy & Environmental Science (2013) DOI: 10.1039/C3EE00015J.

Presentations:

- **L. Murphy**, Y. Li, and H. Aziz, High mobility donor polymer semiconductor for organic solar cells, 3rd Annual Nano Ontario Conference, 2012.